Pore Resolved Simulations of Char Particle Gasification

Greg Hingwah Fong
Marquette University

PORE RESOLVED SIMULATIONS OF CHAR PARTICLE GASIFICATION

by

Greg Fong, B.S.

A Thesis submitted to the Faculty of the Graduate School
Marquette University
In Partial Fulfillment of the Requirements for
The Degree of Master of Science

Milwaukee, Wisconsin

August 2017

ABSTRACT
PORE RESOLVED SIMULATIONS OF CHAR
PARTICLE GASIFICATION

Greg Fong, B.S.

Marquette University, 2017

Coal is a significant source of energy in today's world and many studies have been conducted in order to better understand and optimize its use. To address greenhouse effects associated with coal combustion, cleaner methods for harnessing its energy are being explored. One such method is gasification, a process which converts coal into syngas, a mixture consisting primarily of H_2 and CO. Syngas can be used to generate electricity or to produce hydrocarbons that can be used as fuels.

To better understand and optimize the process, simulations can be used to study the gasification of individual porous char particles that form within the gasifier. Available models range in complexity from zero-dimensional models to CFD simulations. However, most studies simplistically treat the char particle as an effective porous continuum, despite the fact that the presence of large, irregular voids and fractures renders such treatments invalid. This work presents a three-dimensional simulation of a reacting porous char particle that resolves these large voids using micro-CT imaging in order to better understand the interaction between reaction and transport during gasification. In order to correctly gauge the impacts of the resolved structure, a second model was developed which employs the simplistic assumptions in question: a perfectly spherical particle and an effective continuum treatment of the porous structure. To faithfully compare the models, both particles have identical mass, volume, porosity and equivalent diameter.

The results of the simulations indicate the necessity of accounting for the presence of large voids in any char consumption model, as they enhance reactant transport into the particle. By introducing additional avenues for transport, the species and temperature profiles within the particle are significantly different in the two models. Furthermore, with enhanced transport, the amount of accessible surface area increases, resulting in faster reaction rates and a reduction in char consumption time.

ACKNOWLEDGEMENT

Greg Fong, B.S.

I would like to first sincerely thank my advisor, Dr. Simcha Singer for the opportunity to work on such challenging yet interesting and meaningful project and for the past two years in the Graduate School of Mechanical Engineering. Without his support, advice, and intelligence, I am sure I would not have been able to have such a memorable experience. Also, I would like to thank Dr. Singer for his guidance, a combination of clear direction and independence, which enabled me to get passed the tough times when progression seemed to come to a halt. I would like to also thank my committee members: Dr. Somesh Roy and Dr. Anthony Bowman, who advice and feedback have helped me further my knowledge regarding Fluent and progress on my research.

I am also grateful and thankful to the American Chemical Society who have provided support the funding for this research. I would also like to thank Dr. Zhongzhe Liu and Dr. Taly Gilat-Schmidt for helping to create the coal char particles and obtain micro-CT scans.

My graduate experience would not be complete without mentioning my current and previous colleagues from the Thermal Lab, Rui Gu, Jianqing Li, and Alanna Cooney. These intelligent individuals have enriched my graduate experience as their friendship and support consistently encouraged and motivated me to remain diligent to my research. In addition, their feedback and suggestion have greatly helped and better me in my class work and thesis. Also, I would like to thank my best friend, Daniel Drzewiecki, who is pursing graduate studies at the University of Illinois Chicago, for all his support and life advice he has provided me to help me become a better person and manage the graduate lifestyle.

I would also like to thank my parents and brother, who always supported me one way or another allowing me to focus more on my graduate studies. Without their words of encouragement and their advice regarding life and academics, my graduate journey would have been significantly more difficult and hectic. Finally, I would like to thank my girlfriend, Renata Vinhas, who has supported me throughout my graduate studies and for being understanding of the graduate lifestyle. Without her love, I doubt I would have had such a great graduate experience and been successful in my thesis and classwork.

TABLE OF CONTENTS

LIST OF TABLES

LIST OF FIGURES

Chapter 1. Introduction

1.1 Background on Coal and Char Particle

Coal is a well-established essential energy source and is still used to produce a significant portion of the world's electricity. Coal accounts for approximately 41% of global energy generation and is projected to account for at least 30% of global electricity generation until 2040.[17] An example of high coal dependency can be seen in the United States where in 2015, coal is the highest energy generation source at 33% tied with natural gas. This percentage approximately equates to 1.3 trillion kilowatt-hours of electricity generated fueled by approximately 700 million short tons of mined coal. This amount of coal forecasted for the near future to remain constant or slight increase in demand.[23] The majority of current coal utilization is accomplished through a highly polluting method, combustion, as the harmful byproduct, carbon dioxide is released into the atmosphere contributing to the greenhouse effect. As the world becomes more aware of the consequences associated with pollution, cleaner energy production methods are being researched in order to reduce emissions, increase efficiencies, and divert from high pollutant technologies, such as coal combustion. An alternative method of harnessing the energy store in coal is through the method of gasification.

Gasification reaction that highly characterize gasification process, primarily does not occur with coal, but with its carbonaceous solid, char. Char particles are produced when the coal particles are heated to a sufficient level that its macromolecular networks begin to decompose, and ultimately releases the light gases and tar, leaving only a primarily carbonaceous porous particle. The evacuation of the light gases and the tar occur at a short

time scale upon entrance of coal in the gasifier. This process is called devolatilization if it occurs in a reactive environment or pyrolysis if it is in a non-reactive environment. The purpose of this study will focus on char particles that are created from devolatilization. During the devolatilization process, the char geometric features, such as random voids, and char pore structure and networks are formed. The char pore structure and its morphology also are highly dependent on the type of coal, whether the coal is plasticized or non-plasticizing, and its heating conditions (operating pressure and temperatures).[37]

Due to the resultant coal char having a wide range of pore sizes, the pore sizes are classified into generally three regions: macropores – pore diameter greater than 50 nm, mesopores - pore diameter within 2 and 50 nm size, and micropores – pore diameter less than 2 nm. Overall, the devolatilization process results in the creation of a vast amount of pores, creating a large specific surface area. Resultant specific surface areas range from 80 m^2/g to 600 m^2/g and greatly exceed the surface area of a smooth sphere that may be used to represent a char particle. The majority of the specific surface area is associated with the micropores and mesopores due to their vast number and high surface area to volume ratio, which results in most of the gasification occurring on micropores and mesopores due to the majority of particle surfaces are associated with these pores sizes. Penetration through these pores causes gasification reactions to primarily occur within the particle, as compared to the outer particle surface.

Once the coal has sufficiently devolatilized, the resultant porous char particle undergoes gasification characterized by heterogeneous reactions under a high temperature and pressure (1 atm to 30 atm) environment, primarily consisting of CO_2 and H_2O to produce a mixture primarily consisting of H_2 and CO, which is referred to as syngas. The

importance of syngas can be seen in its use in the production of chemicals, fuels, and fertilizers. Alternatively, the gasification coupled with the Fischer-Tropsch process can convert the syngas into liquid hydrocarbons for lubrication and fuel applications and can be a suitable substitute for petroleum. Gasification's main limitation and overall rate-limiting process is char conversion, converting char into syngas, which occurs at a significantly slower rate than devolatilization.

Various gasifiers have been developed but this study focuses on entrained flow gasifiers. Entrained flow gasifiers were chosen due to their ability to utilize a wide variety of coal feedstock while convert most of the resultant char into syngas at the sacrifice of cold gas efficiency, a measurement of a gasifier's efficiency based off the ratio of flow energy within the gasifier to the energy of the fuel.[23,46] Coal slurry along with steam and oxygen are concurrently fed into the entrained-flow gasifier, which operates at high temperatures and pressures. The char particles are entrained or have low relative velocity between the particle and flow by environment and begin to convert. The resultant syngas is extracted from the gasifier at an outlet while the slag or majority of ash, a undesired byproduct of the minimal combustion that occurs within an entrained-flow gasifier composed of many inorganic species, is extracted from another outlet.

1.2 Gasification

Gasification reactions are heterogeneous reactions where the reactant (this thesis focuses on only H_2O and CO_2) react with carbon contained within the char particle surfaces. These heterogeneous reactions consume the char, eventually fully converting the char into syngas. Char consumption reactions, either gasification or combustion, are

primarily categorized using a "three zone" theory, in which three main zones or regimes are defined to capture nature of the heterogeneous reactions in porous solids.[39] The defining criteria for these three zones are characterized by the amount of reactant species penetration into the particle, which ultimately compares the rate of internal char consumption to the rate of reactant transport.

Zone I, also referred to as the kinetic-limited zone, is characterized by sufficiently slow reaction rates which permits species diffusional transport to overcome species consumption. This results in an approximately uniform species profile within the char particle. Zone I conditions are used to extract kinetic parameters, such as activation energies, due to limited internal distortion attributed to transport effects. Zone II, also referred to as the intra-particle diffusion-limited zone, is characterized by reactions rates and species diffusional transport rates of similar magnitudes, which results in the partial species penetration and species gradients within the char particle. Char consumption consequentially occur within the particle in correlation to the amount of species penetration and the physical properties (e.g. temperature and porosity) at the penetration location. Zone III, the externally diffusion limited regime, is characterized by reaction rates significantly faster than mass transport, resulting in reactions and char consumption primarily confined to the external surface area. The internal particle density remains constant throughout Zone III consumption due to minimal species penetration. Each zones' characteristics are illustrated in the figure below assuming the char particle is perfectly spherical. It may be noted that the X axis is the radial distance, Y axis is the reactant concentration, the circle is to represent the char particle's radial domain, and the colored lines represent the zonal behaviors. Please note the possible variations for Zone II regimes as shown in Figure 1.1.

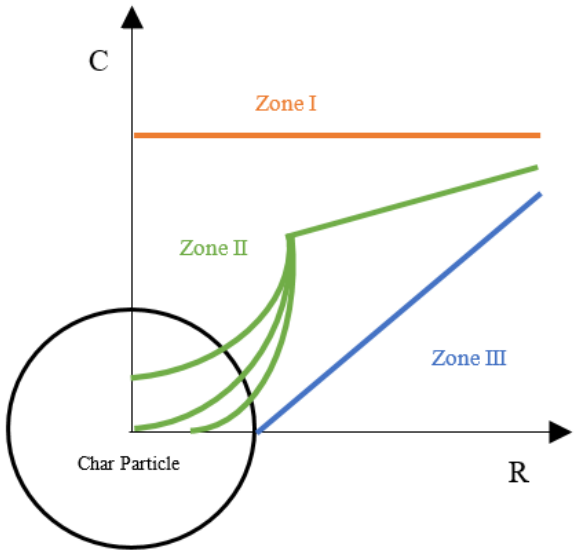

Figure 1-1. Typical Radial Species Concentration Profile of Individual Zones

There are many factors the zone in which gasification primarily occurs, but a highly influential factor is the particle temperature for a specified constant particle diameter. Many well-established works and studies were conducted to analyze and capture the effects of particle temperature. The reaction rates for each zone is shown in Figure 1.2 for a set particle size where the slope of the plot correspond to the measured activated energy for the specified zone. It may be noted that operating parameters (e.g. pressure and temperature) are modified to transition the particle between zonal behaviors. In Figure 1.2, the X axis is the inverse temperature and the Y axis is the logarithmic total reaction rate. In Zone I the heterogeneous reaction rates, shown with constant activation energy, are not affected or distorted as the reactants are able to fully penetrate the particle and are not hindered by diffusion through the particle structure. In Zone II, the reaction rate is significantly affected as indicated by activation energy being approximately half of its non-

distorted value due to resistance from the particle structure.[57] Distortions and resistance from the particle structure introduce reactant species gradients throughout the particle, ultimately reducing the amount of internal gasification reactions when compared to Zone I. Lastly, Zone III exhibits an activation energy that approaches or is zero, due to limited reactant penetration into the particle resulting in little to no gasification reactions occurring within the particle.

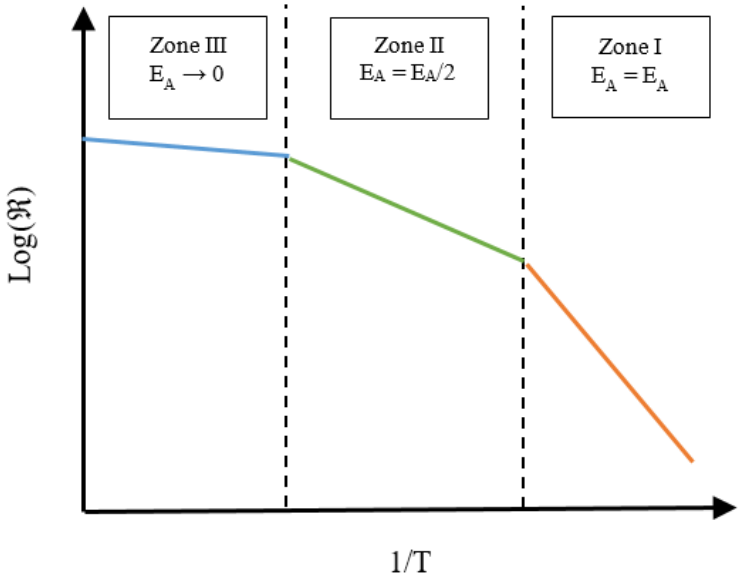

Figure 1-2. Heterogeneous Reaction Rates Vs. Particle Temperature of Specific Zones

1.3 Motivation

Coal char gasification is typically characterized by a heterogeneous reaction that occurs between the surrounding gas mixture and the char particle which is produced during devolatilization. In order to represent the porous nature of the char particle, the effective porous continuum assumption is typically applied to the char particle, ignoring the

necessary length-scale constraints, which restricts its application to cases in which the characteristic size of the pores is much smaller than the size of the particle. The effective porous continuum assumption is a simplistic approach to modeling a char particle porous structure by lumping all pore types and geometric features (e.g. irregular voids) within the geometry domain in a single porosity variable which is used to track particle progression. This is illustrated in the equation below.

$$L_{pore} \ll L_{particle} \tag{1.1}$$

In order to account for the invalidity and inaccuracy of the effective porous continuum for particles with larger voids and fractures, discrete representation of char particles with Monte Carlo or random walk methods were also used.[44,53] However, due to complexity, inaccuracy and computational power required by the discrete representation, almost all models still employ the effective porous continuum assumption along with adjustable parameters. Incorporating adjustable parameters negatively affects the model results by restricting predictive power and the knowledge gained from the simulations of gasification within the char particle.

In order increase the syngas production efficiency, understanding the fundamental factors of chemical reaction, species transport (mostly diffusion), and morphology at the char particle scale is necessary. However, understanding the impact of these factors is difficult due to their being coupled for gasification, which occurs in Zone II. The Zone II regime occurs at temperatures and particle sizes such that both chemical reaction and species transport through the porous particle significantly influence the overall heterogeneous reaction rate. This is indicated by reactant species partially penetrating into

the char particle, and to varying extents, as time progresses. Experimentally extracting the impact of reaction, transport and morphology for Zone II conditions is very difficult due to their coupled nature.[49,50] On the other end of the spectrum, current simulation approaches are limited in the applicability and predictive power by their inability to resolve the irregular char particle structure, which is often treated as a symmetrical, homogeneous porous sphere.[44]

The purpose of this thesis is to improve the fundamental understanding of the interaction between reaction, transport, and morphology during char particle gasification, and to inform simpler models used as submodels within computational fluid dynamics (CFD) simulations. This is accomplished through the use of reacting CFD simulations with a realistic char particle geometry obtained from X-ray micro-computed tomography experiments (micro-CT). The model removes the questionable assumptions of previous simulations: perfectly spherical char particles, and the application of the effective porous continuum model for the entire char particle, even when Eq. 1.1 is violated.[19,56]

To accomplish the stated research objectives, the large pores of an actual (non-spherical) char particle geometry will be resolved in 3-D, allowing for a better representation of realistic char. In the resolved pores, conservation equations based on first-principles will be employed, rather than equations based on the effective pore continuum treatment, which is inapplicable and inaccurate for large pores that are of the same order of magnitude as the particle itself. For the small micropores/mesopores, which are much smaller than the size of the particle, the effective porous medium approach will be employed. Both limitations of current models are illustrated in Figure 1-3, which illustrates the high frequency of larger macropores, and a typical three-dimensional char morphology

from SEM is shown in Figure 1-4, which illustrates many abruptly ending macropores also known as blind pores, both indicating macropores that violate Eq. 1.1 if incorrectly implement.

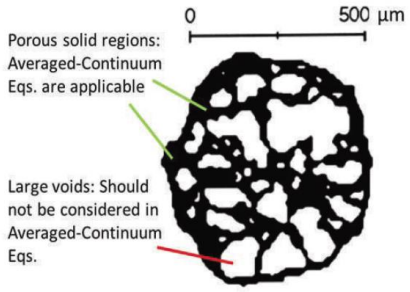

Figure 1-3. Cross Section of a Char Particle[60]

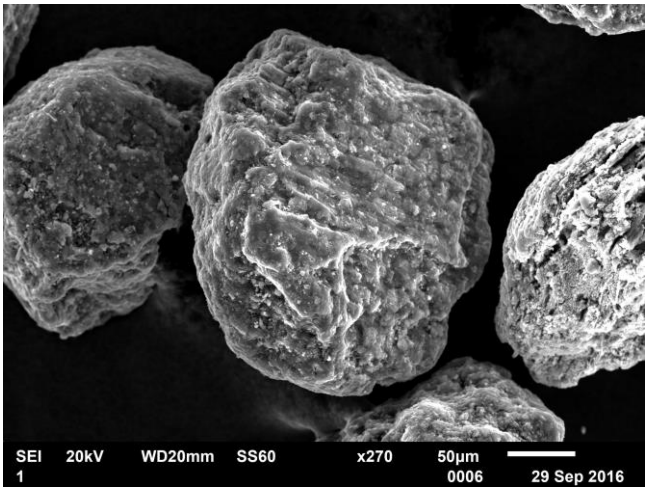

Figure 1-4. x270 SEM Image of Lignite Char Particle of Approximately 100 µm

Previous experimental research has been conducted on the effects of very large char particle geometry using CT scans, but not micro-CT scans. This resulted in some hypotheses regarding the reactant transport within char particles that will be studied as part of this research. Maylotta et al. (1986) studied the real time gasification and pyrolysis of

a coal in situ through the use of a CT scanner. From their work, Maylotta et al. hypothesized, that large voids/cracks enhance access to the microspores (d < 2nm) where the reaction predominantly occurs. This work correlates with Karacan and Badger who determined experimentally that the large voids are connected throughout the particle via high resolution CT, which theoretically should enhance reactant transport.[16] In addition, Hodge et al. also concluded that the assumption of perfect spherical char particles is inadequate for porous solids due to the particle conversion and heterogeneous reaction rates being strongly influenced by particle morphology.[22] Applications of this research is not limited to coal specifically and can be applied to other char, such as bio char, and could also be applied to combustion, as well as gasification.

1.4 Thesis Outline

Chapter 2 covers a literature review conducted in order to introduce the necessary background knowledge regarding gasification of char particles. Initially, well-established and early models are discussed in order to understand the basic fundamentals of char gasification and the underlying foundation of later char consumption models. These well-established models include effectiveness factor and global models. Afterwards, more recent models are discussed and critiqued with an emphasis on the models assumptions, primarily the effective porous continuum assumption, and the char particle geometry.

Chapter 3 focuses on how the char consumption model of this thesis is developed and an explanation of the boundary conditions. This section initially begins with discussion of the software packages utilized and their advantages compared to other comparable software packages. Primary software packages that are discussed are ANSYS Fluent v.

17.1 and Simpleware ScanIP. Afterwards, the coal type and process of converting the coal into char is discussed in detail. At this point, capturing the char particle geometry so it can be implemented is discussed. Lastly, explanation of the chosen parameters and boundary condition of the CFD model along with any customization are explained.

Chapter 4 analyzes the differences between of two models' results. One model implements an unresolved particle geometry with complete implementation of the effective porous continuum assumption while the other implements a partially resolved real char particle with the effective porous continuum assumption in the resolved regions. The main modes of comparison are via contour plots, one-dimensional plots, and effectiveness factor at various distinct points in the particle progression. Main variables that are analyzed are all species, diffusion coefficients of all species, temperature, gasification reactions, porosity, and conversion.

Chapter 5 concludes and recaps the findings that were determined from Chapter 4 with the reasoning that led to the final conclusion. Main aspects that are mentioned are the relative error of the complete particle lifespan between the models, the reactant penetration rate, and the effectiveness factor. Lastly, Chapter 6 discusses how the future work of the study regarding how study can be further refined, have its applicability expanded, and inform fundamental submodels.

Chapter 2. Literature Review

This chapter discusses previous studies and their approaches to capturing gasification and consumption of a single char particle. The two main types of models presented are analytical models (global models, effectiveness factor models) and numerical models of single char particles. The vast number of numerical models can be divided into two main categories, models which focus on the varying particle structures based off their morphological features (e.g. pore distribution) and those which focus on the particle boundary layer (can include particle structure). The focus of this literature review is to review models that analyze the impact of the varying particle structures and compare them to the analytical and numerical models. Analytical models are models which do not solve PDE, are non-spatially resolve, and only require a single value for a variable while numerical models are models that can be spatially varying, have variable profiles, and are based on a numerical solution of governing equations.

2.1 Global Models

The most fundamental and least complex type of model is the global model. Global models, for instance, shrinking core models, capture the consumption of a single char particle under the assumption that all the reactions occur at the surface of the particle and no reactant species diffuse into the particle.[31] From these assumptions, the conversion of a single particle under given operating parameters is used to empirically solve the particle's reaction rate constant per unit external surface area, $4\pi R^2$.[31,32] The global models can also be modified to add complexities to improve accuracy, such as including the effects of transport in the surrounding boundary layer. This is accomplished assuming steady state

conditions and by equating the rate of diffusion through the boundary layer to the heterogeneous reaction rates. This assumes that once the reactant diffuses into the particle, the reactant is immediately consumed via heterogeneous reactions. The char particle consumption rate is then easily solved in an explicit algebraic formula.

Although this model can be used to give overall insight into burning times, the model has a variety of limitations associated with it. Assuming that no species diffusion occurs within the particle simply ignores the effects of the microspores and mesopores, which causes Knudsen diffusion to occur within the particle. Knudsen diffusion facilitates species penetration into the particle by capturing the diffusion within a porous setting that includes species interaction with the pore walls. Also, pores of a larger scale and/or geometric features (e.g. voids) can facilitate species transport throughout the particle, providing another method of species penetration. Having species penetrate the particle ultimately leads to heterogeneous reactions occurring within the particle thus invalidating assumption that heterogeneous reactions only occur at the particle surface. Invalidating these assumptions suggests that the particle consumption does not occur in a constant density fashion as the global models suggest.

In practice, global models employ measured reaction rates, which account for internal as well as external reaction, and simply assume that this consumption occurs on the external surface. On the face of it, this does not appear to be a major shortcoming if the goal is to predict overall the char consumption rate. However, the remaining major limitation of the global models is their lack of versatility. Since the global models typically utilize experimental data in order to determine the char consumption rate, the resultant global model is only valid for char particles under the same or similar physical process.[34]

For example, if a global model was to be produced from experimental data in Zone I behavior, the same model could not be implemented in order to insight char particles undergoing Zone II or Zone III behavior or under different operating circumstances.

A Zone III case that clearly illustrates the described global models' flaw is when the particle velocity has a significant impact, which causes limited to no species diffusion in the particle, thus requiring reaction rate data that reflects primarily outer surface reactions. If the same reaction data was to be applied to Zone I/II or even transitional zones global model, the global model would not be able to accurately represent the actual physics. The reasoning is that a significant amount of reactions occurs within the particle which, in this particle case, under evaluate the carbon consumption. Even in situations where the operating parameters are slightly changed from a previous global model's parameter but still categorized in the same zone, the global model would lose accuracy as reaction rate would change accordingly to operating parameters.

2.2 Effectiveness Factor Models

An alternative and more realistic analytical model than the global models is the effectiveness factor model. The effectiveness factor model was initially developed for chemical engineering applications, such as catalytic porous pellets, but since char consumption shares similarities with these applications, effectiveness factor models were later implemented in char consumption studies.[20,24,35,60] The effectiveness factor models are differentiated by the basic geometry (e.g. cylinders and slabs) that the model is to represent.[41] In the case of char particle consumption, a sphere is employed, as most char particles are somewhat spherical. The effectiveness factor, η, represents the ratio of the

actual reaction rate integrated for the entire particle, which accounts for diffusion limitations, to the ideal reaction rate, if transport were infinitely fast. The effectiveness factor model's reaction rate, $\Re$, equation for the ith reaction is:

$$\Re_i = \Re_{ideal,i}\eta_i(\phi_i) \tag{2.1}$$

As shown above, the effectiveness factor, η, is a function of a non-dimensional variable, the Thiele modulus, ϕ_i, which is similar to a Damkohler number, and is the square root of the ratio of surface reaction rate to diffusion rate of the ith reaction. The Thiele modulus is a function of species concentration at the surface, the effective diffusion coefficient, and the reaction rates.[41,43] This is illustrated in the Thiele modulus for the nth reaction order equation below:

$$\phi_i = R\left(\frac{Sk_r(T)C_{As}^{n-1}}{D_{eff}}\right)^{0.5} \tag{2.2}$$

where R is the radius, S is the specific surface area, k_r is rate constant, C_{as} is the surface concentration of species A, and D_{eff} is the effective diffusion. In order to solve for the concentration of species within the porous particle, integration of a pseudo-steady state expression from a shell balance is performed. The species conservation equation is expressed in spherical coordinates is shown below:

$$\frac{1}{R^2}\frac{d}{dR}\left(R^2 D_{eff}\frac{dC_A}{dR}\right) = Sk_rC_A \tag{2.3}$$

Unlike global models, the effective factor models show versatility by enabling the use of *intrinsic* kinetic reaction data in the effective reaction rate expression, which is applicable in any zonal behavior and operating parameters. *Intrinsic* kinetic data is gathered from experiments in Zone I and normalized by the internal surface area.[41] The experimental data is then extrapolated and expressed in representative activation energies, pre-factor exponentials, and order of reaction.[32] The resultant factors are applied to the Arrhenius equation shown below, which is a function of temperature, to obtain the corresponding reaction rate.

$$k_r(T) = Ae^{-\frac{E_a}{R_u T}} \tag{2.4}$$

Once all necessary parameters of the Thiele modulus have been solved and implemented, the relationship between the Thiele modulus and the effectiveness factor can be utilized. The effectiveness factor expression is derived by integrating and solving the species equation shown in equation (2.3). The relationship is shown below:

$$\eta_i = \frac{3}{\phi_i}\frac{\phi_i coth\phi_i - 1}{\phi_i} \tag{2.5}$$

The corresponding reaction rate(s) are obtained and are used in an expression which relates reaction rate(s) to the rate of carbon consumption. A common method for measuring char consumption is via the conversion, *X*, a non-dimensional variable that relates the change of carbon mass from initial to a specified time. The conversion rate is related to reaction rates as illustrated in the expression below:

$$\frac{dX}{dt} = -\frac{MW_c}{\rho_{p,o} W_{C,o}} \sum_{i=1}^{i} v_{C,i} \Re_i \tag{2.6}$$

where MW_c is carbon molecular weight, $W_{c,o}$ is the initial percentage of carbon, $\rho_{p,o}$ is the initial particle density, $v_{c,i}$ is the carbon stoichiometric coefficient of the ith reaction, and $\Re_i$ is the ith reaction rate. By determining the conversion rate, the rate of porosity change is easily obtainable. In order to increase accuracy, effectiveness factor models are also able to account for boundary layers in a similar fashion to the global models. Bischoff later expanded the effectiveness factor model to be able to estimate the associated effectiveness factor of any single arbitrary reaction rate derived from absorption and simple reaction order curves.[38]

Although the effectiveness factor models improve on the global models' shortcomings, primarily the lack of accounting for species penetration within the char particle, the method still has major flaws due to its simplifications. One of the major challenges that the model faces is its assumption that the char particle pore structure only evolves in a uniform manner throughout the particle. Spherical shape implemented to model a char particle. Finally, the effectiveness factor model ignores significant pore structures such as large voids, surface contours, and porous networks. This becomes problematic as geometric features, such as large voids, may facilitate mass transport. The larger voids can introduce reactants to potential large porous networks leading reactants further or in different regions in the particle, which will ultimately cause for significant and varying internal conversion profiles. Overall, the porous structure has the potential to accelerate the char consumption and impact species gradients that cannot be captured in

the effectiveness factor. Accounting for these spatially varying parameters from the two stated major flaws also invalidates the fundamental assumption, effective porous continuum of the effective factor model. By lumping all pores together and not somehow adjusting for significant pore effects, the model assumes all pores affect char consumption and progress in a similar matter. In reality and from the previously mentioned shortcomings, this is simply inaccurate and undermines the effect of significant geometric features, primarily large pores.

2.3 Numerical Models

In this section, char consumption numerical models that capture the spatial gasification and/or combustion in a discrete particle and fluid domain are discussed. Numerical models are models which are models that are based on numerical solution to governing PDE. These models obtain their solutions by iteratively solving a set of conservation equations, such as, Naiver Stokes, energy, and species. In combination with the conservation equations, submodels are incorporated to modify and improve the realism of the overall model. Typical submodels include particle evolution (e.g. char conversion), local pore evolution, effective diffusion coefficients, gasification reactions, and ash behavior. These models are later categorized into two types, two-dimensional and three-dimensional models. It may also be noted that models are differentiated by how the particle structure is represented.

One of earliest and fundamental numerical studies that was conducted to analyze char consumption including pore structure and surface area evolution was developed by Gavalas.[27] Gavalas developed the random capillary model to include the effects of

overlapping capillaries within unresolved domain in order to account for randomly located porous networks coupled with a wide range of pore sizes ranging from mesopores to macropores. Although this particular study by Gavalas focuses on the kinetic regime, Gavalas mentioned that the same model is applicable to diffusion limited regimes but requires a numerical solution.[27] As mentioned before, the proposed one-dimensional pseudo-steady state model is able to model random pore networks in the unresolved region by randomly positioned long cylindrical straight capillaries that can overlap and extend through the representative char geometry, a sphere. Evolution of the char particle surface area and the pore size distribution is captured through the variables conversion and density. Conversion and density are determined via the pore growth variable, q. The pore growth variable is then implemented to determine the current radii of the capillary pore and the particle. Gavalas acknowledges that diffusion highly depends on the pore size and due to the implementation of such a wide pore size range, difficulties in determining the diffusion coefficient arose. Rather than using a continuous pore distribution, Gavalas opted to simplify the derivation of the effective diffusion from a discrete set of three pore sizes, each representing the three different pore categories. Gavalas's model was later expanded by Hurt et al. who included the effects of densification or shrinkage of particle surface area supported with greatly magnified optical photographs at various levels of conversion (e.g. SEM).[51] Applications of the Gavalas fundamental analysis in other fields can be seen in Dixon's 3-D CFD model analyzing the effects of number resolved straight cylindrical pores on transport and reaction in catalytic porous pallets.[1] Similar to Gavalas, Dixon concluded that the resolved cylindrical pores are significant in the catalytic pellets.

Gavalas' modeling approach gave insight on pore evolution of an unresolved domain of a wide distribution of pore size and highlighting its interplay with random pore networks. However, Gavalas still acknowledges significant variations between the random pore model and experimental data, most notably in higher temperature ranges, which ultimately reveals necessary improvements. Gavalas attributed these discrepancies to the lack of accounting for the initial transitional phase into and within regime II, the random pore model being invalid at higher conversions (approximately 0.7 or greater).[27] The second and more fundamental weakness is related to the effective porous continuum assumption not being exactly valid. Even though the porous networks, most likely to be macropores, are accounted for as straight long capillaries, real networks behave significantly different from what Gavalas' derivation assumes. Some significant geometric properties are single outer macropores branching off into multiple regions and leading to discrete networks, having significant curvature, ending abruptly within the particle, and having the ability to vary in diameter with respect to the particle radial location. Rather than including these factors into the random pore model, these important macroporic geometric features are lumped into the effective porous continuum assumption, which ultimately reduces the accuracy of the model as consequence of inaccurate physical representation. As Gavalas suggested, the model can be expanded for Zone II studies but without any further modifications, the model loses its merit. This is apparent when calculating diffusion coefficients from a discrete set of pore radii is inadequate as unresolved pores, captured in the effective porous continuum assumption, vary spatially and will impact char consumption rate and profile.

Sahu et al. presented a one-dimensional transient model that captures the consumption of a carbon undergoing isothermal combustion from a discrete representation of a cenospheric char particle's initial and progressing structure coupled with calculating diffusion via random walk method.[53] It is also assumed that diffusion is negligible and the particle is sufficiently small enough to be assumed isothermal. The spherical voids, which characterize cenospheric char, are randomly distributed through a 50-micron diameter particle with the ability to overlap allowing for realistic pore networks that may reach the particle surface. Pore growth of available resolved surface areas connected to the ambient environment, internal or external, were captured with the pore growth variable, q, analogously to Gavalas.[53] Varying initial void fractions and number of voids were implemented for a diverse result data set along with comparison of the initial void fraction via random simulation placement to the corresponding theoretical Gavalas void fraction.

Sahu et al. acknowledges the weakness in their model, which can be seen the initial monodisperse set of voids was not sufficient to capture the initial particle structure. The more significant stated weakness was the possible violation of the pore length-scale constraint, illustrated in Eq. 1.1, as Sahu acknowledges the fact that pore size length-scales can vary up to four magnitudes.[53] Violation of the pore length scale, when coupled with the connective resolved porous network, adds more complexity, which cannot be ignored and will negatively affect results. The model's lack of versatility is emphasized due to its limited application to solely the kinetic limited regime. Although the weaknesses are acknowledged, the model could not to be improved attributed by the limited computational resources at the time.[53]

Sotirchos and Amundson proposed one-dimensional transient models to capture char consumption via combustion and gasification for both a shrinking and constant char particle radius while also accounting for an external boundary layer.[58] Both models implement conservation of mass, species, and energy equations and include the effects of the evolving pore structure on surface area, diffusivity, specific heat and other local transport and thermodynamic properties of the porous particle. The heterogeneous reaction rate expressions are also functions of the local conversion via the internal surface area. Diffusivities are also heavily influenced by pore structure: Knudsen diffusivity is a function of variables such as porosity and pore radii, and the effective continuum diffusion coefficient for a porous media also depends on the porosity. The presented model excels compared to previous models due to its ability to better reflect particle realism via bimodal pore-size distribution.

Although the model's dynamics prove to be informative, justification of the effective porous continuum assumption is still questionable. Evidence of questionable assumptions still loomed and can be seen in pore radii distribution as one dimensional models only have the capability to utilize symmetric distributions of any variable. This does not correctly reflect a real char particle as geometric features are not symmetrical, non-uniform initially and are somewhat random. In addition, the model does not account for voids or discrete pore networks, which may enhance mass transport. As previously mentioned, other means of transport inside of the particle will accelerate char consumption as heterogeneous reactions are not confined to primarily the outer edge of the particle. Representing the char particle as a perfect sphere also neglects the effects of the morphology of the particle, which may increase available surface area for heterogeneous

reactions to take place. The effective porous continuum also fails at capturing internal geometric features such as cenopores, which will have an effect once the char particle has sufficiently shrunk to the void's corresponding radial location.

A slight deviation from the typical of a carbon consumption model was Zoulalian et al., who proposed a one-dimensional transient model to capture the diffusion limited and kinetic limited evolution of a wood char particle (via random pore model similar to Gavalas), depicted as a homogeneous porous slab.[11] The model considers the effects of water vapor and carbon dioxide gasification reactions. Boundary conditions at the center and outer surfaces and initial conditions (e.g. initial porosity and concentrations) were used to solve conservation equations, diffusion coefficients (including Knudsen diffusion), and current porosity along with many other expressions. Among the expressions, many well developed expressions or formulations (e.g. convection transfer coefficient) were developed for spherical cases but were adjusted in order to be applicable to the one-dimensional Cartesian models. An example of this is implementing a suitable value for the variable, pore diameter determined from a ratio of external specific surface area (surface area per unit volume) of a sphere to a slab.[11] Limited diffusion and kinetic cases were conducted under various structural parameters, Ψ and temperatures in order to compare the resultant limited diffusion and kinetic data sets, reactive surface area, and reaction rates (water vapor and carbon dioxide). Model results correlated with experimental findings and the phenomenon that the intrinsic gasification rates are proportional to the resultant surface area and is a linear function of natural log of the ratio of current to initial particle density.[11]

Zoulalian et al. also presented a 500x magnified figure of a real wood char particle, which the model is to represent but raises some concerns regarding the assumptions made

in the model. The primary assumption, pseudo-homogenous slab pores, and its associated effective porous continuum assumption comes into question as the magnified figure shows a neighborhood of pores in the central region of the particle whose radii are several times larger than the surrounding pores. Without compensating for the effects of macroscopic pores, even more when considering a potential neighborhood, inaccuracies may occur as species are able to better penetrate into the particle via these large pores and ultimately enhance and accelerate gasification within the particle and conversion. As other factors such as temperature, diffusion, and species concentrations are naturally coupled with heterogeneous reaction rates that fuel gasification and conversion, the effects of the significant porous regions may also trickle to the remaining microporous regions and cause model inaccuracies.

Despite the challenges that are incorporated with accounting and modeling the effects of macropores, Cai and Zygourakis developed a one-dimensional transient model to further the established grain model to incorporate the effects of defined interconnected porous networked. The char particle in question undergoes combustion at specified temperature and mixture composition of nitrogen and oxygen. The pore structure was reconstructed by positioning grains to emulate a significant portion of the desired char structure; most notably bituminous Illinois #6 char. The grains were assumed to be spherical, constant grain diameter (to simplify grain effectiveness factor calculations), structural integrity does not compromise, and grains are non-diffusible. Grain surface area, diameters, and quantity were derived from experimental data.[60]

Limitations of the proposed model are evident in static structure. Without the decay of the char grain structure, the model is unable to alter the available surfaces for

heterogeneous reactions to occur on thus unable to provide insight on reaction and species patterns. The lack of transient behavior of the structure does not account for the dynamic contribution to reactions of various surface regions as the char particle continues to evolve and undergo consumption. Although the presented model accounts for the effects of the macropores, shown from the voids surrounding the grains, meso and micropores' effects are neglected, this is evident in the lack of porous effects in the grains. This inability causes the model to ultimately reduce the heterogeneous reaction sites and pathways for mass transfer further into particle, thus producing inaccuracies and difference between experimental and simulation results.

Wang and Bhatia proposed a transient one-dimensional model to capture the gasification of a single char particle, the resultant structure evolution, and peripheral fragmentation surrounded by a boundary layer. The implemented char structure was depicted by micropores which are represented within spherical grains surrounded by voids which represent macropores. Macropore diameters are held constant throughout the simulation while micropore diameter grows accordingly to the amount of gasification that occurred. Justification of only dynamic micropore diameter was given based on the majority of particle surface area being associated with micropores, thus heterogeneous reactions are governed by micropores.[24] In order to reduce complexity, individual micropore grain are assumed and modelled to have unity effectiveness factor. This causes for no internal grain concentration gradient but only at the char particle scale.[26] Transport through multicomponent diffusive and molar fluxes are separately determined from the two categorized pore sizes from the bidisperse dusty-gas model using the corresponding porosity and tortuosity.[24]

However, the proposed model still inherits the problems associated from implementation of the effectiveness porous continuum assumption. The assumption becomes problematic as it is applied to the most significant portion of the model, the microporous spherical grains, as it forces all pores on a grain to be a uniform pore diameter and growth at the same rate. The lack of diversity of pore sizes on individual grains has potential to skew conversion rates and profiles of the individual grain which may further translate into greater overall impact on a particle scale. Additionally, the justification of individual microporous grains' inability to have internal concentrations comes into question as internal concentration become more significant when modeling particles with higher initial radii due to the likelihood of operating in Zone II. The dynamics of the proposed model comes into question when the model also neglects to capture the growth of macropore radius. This is an issue as the macropore radius already has the potential to increase reactant transport further in the particle, potentially accelerating particle conversion, and will its effects amplified once the radius begins to increase.

Xu et al. proposed a mathematical one-dimensional transient model to analyze the difference in species concentration and conversion between the gasification of coal and biomass char motivated by the chars' different microstructure.[47] Coal and biomass char are both modeled as small spheres specified at initial particle radius while implementing an effectiveness porous continuum assumption coupled with an initial pore diameter to capture porous evolution and effects. Species and mass conservation equations utilized the effective diffusion, obtained from Knudsen and multicomponent, and convection within the particle. Model dynamics are captures through main variables (e.g. diffusion, porosity, and conversion) that are function of time and radial distance. It is assumed that temperature

is constant throughout the particle justified by the small particle radius. It may also be noted that a similar model was developed by Fatehi and Bai in order to be a tool for extracting *intrinsic* kinetic reaction rates from experimental data for solely biochar.[29]

Although the chosen ambient parameters (e.g. temperature) by Xu et al. demonstrate Zone I properties reducing the effects of porous structure, notable discrepancies still occur between the resultant simulation and experimental results in earlier times. The root of the discrepancies is suspected from implementation of the effectiveness porous continuum assumption. Justification of this claim can be seen primarily in the discrepancies between earlier experimental and simulation species which emphasize the fact that geometric features have a significant effect on mass facilitation. This will skew how the initial reactant penetration into the particle before reaching Zone I conditions and distort information gather at the initial timeframe. In addition with coupling constant temperature throughout the particle, the model represents the heterogeneous reactions are occurring at a symmetric and uniform profile. The contrary can be seen from Cai et al. who illustrate distinct significant macropores in a char particle, which ideally increases the amount of resolved surface area for heterogeneous reactions to take place on.[60] The lack of resolved surface area for heterogeneous reactions to participate on thus skews the species composition especially at earlier times where the majorities of structure properties have not yet decayed. After this initial state, the simulated species composition begins to settle and variation between experimental and simulation data were minimalized.

Singer et al. proposed a transient one-dimensional spherical model to capture the evolution of a char particle under Zone II conditions. Evolution of the particle was captured by an adaptive random pore model, which ultimately coupled with the flux terms used in

the model. The effects of porous networks are also included and derived from randomly positioned overlapping straight cylinders throughout a sphere with individual growth rates Flexibility of the model is demonstrated through the wide range of valid pore radii distribution in order fit varying situations.[54] The model solves standard conservation equations including porous effects through the effective porous continuum assumptions with fixed boundary conditions located in the center of the sphere. In order to account for time varying effective diffusion, Singer implements a Feng Stewart Method in tandem with the Dusty Gas Model.[54] The Dusty Gas Model is first implemented to obtain effective diffusion through a single given pore. Afterwards, the Feng Stewart Model is implemented to distribute the calculated diffusion for a range of pore sizes while implicitly accounting for associated pore networks with potential dead ends.[15,57] Additional realistic transient properties were included in the model in order to improve validity and accuracy. One of the properties is annealing, which captures the reduction of reactivity at high temperatures due to rapid atomic rearrangement.[54] Singer incorporates peripheral fragmentation, which captures the structural decay due to failure in structure integrity. Even though it is hard to model peripheral fragmentation, variables such as pore size distribution, ash content and temperature aid in predictions.

Singer acknowledges the potential weaknesses that may be associated with the proposed model. One stated limitation and a consequence of one-dimensionality was the model's inability to correctly represent an asymmetric and complex geometry and/or an uneven distribution of pore size and number in a char particle.[54] An example of the model's inability was explicitly mentioned was the model's inaccurately capture large voids/pores, such as cenospheres which have the potential violate boundary conditions either at the

surface or center of the particle. The other and major limitation of the proposed model is associated with the implementation of the effective porous continuum assumption. Most notable limitation from the continuum assumption can be seen is the model's inability to account for significant geometric factors, such as branching porous networks, that can facilitate the reactant transport into the particle and may accelerate conversion. In addition, the assumption fails to account for large surface voids or morphology factors, which increase the availability for heterogeneous reactions to occur and may facilitate internal mass transport once a sufficient part of the particle geometry has been consumed. In realistic conditions, the porous networks naturally have some curative and radius among many other factors may vary as the pore penetrates further into the particle overall varying the consumption rate and profile.

As times progressed, computational resources grew exponentially allowing for what was previously deemed infeasible to become possible. Computational fluid dynamics (CFD) has been used to model char consumption. An interesting approach can be seen from Richter et al., who developed a CFD model utilizing the commercial CFD software package, ANSYS Fluent. The three-dimensional, steady state CFD model represented the porous char particle as an asymmetric agglomerate of solid spheres moving through a predefined ambient species mixture composition under various specific pressures and temperatures for the purpose of understanding internal char conversion.[9] The intention of using the agglomerate of spheres was to primarily pseudo-resolve macropores and discrete internal networks. The voids surrounding the spheres represent the macropores and their associated porous networks. In addition, by creating this arbitrary particle structure, realistic particle properties such as surface area to volume ration and surface ratio can be

imitated. From solving the fundamental conservation equations (e.g. species, energy, and momentum) insightful species and temperature profiles throughout the domain and char structure were obtained.

This unique approach to porous char particle modeling may give insight on species penetration in the particle and the resultant conversion but has flaws associated with the model. One flaw was the use of steady state to capture what is naturally a transient process: char conversion. Without a transient model, conversion has no effect on the char structure and the properties of the porous medium. This ultimately causes inaccuracies to occur in the resultant species and temperature profiles. Furthermore, in realistic char particles, the solid region between the resolved pores is itself highly porous, but the structure in Richter's model (the agglomerate of solid spheres), was defined as a solid and thus no mass transport or reaction is allowed within the defined structure. This greatly undermines the effect of mesopores and micropores, and confines the heterogeneous reactions to the surface of the spheres. Lastly, the model implements a constant diffusion coefficient for all species. This is highly problematic as there are significant temperature gradients surrounding and within the agglomerate. Since diffusion is naturally highly dependent on temperature and pressure, the diffusion coefficients should be recalculated in order to maintain accuracy throughout the entire model.[12]

Another CFD model was developed by Safronov et al. who proposed a two-dimensional axial symmetric steady state model of a single coal particle of various diameters, represented by essentially an impenetrable solid sphere, moving through previously determined ambient gas at various specified Reynolds number.[20] The environment is specified in order to expose the corresponding particle to oxidation regimes,

primarily, diffusion controlled (Zone II), transitional (intermediate between Zone I and II), and kinetic controlled (Zone I). Influences of porosity were accounted for by effectiveness factors derived from a given constant porosity and specific surface area. The model resultantly gave insight regarding species profiles, temperature profile, and carbon consumption rates from set inlet conditions. The primary finding is the inner particle surfaces, that are heavily influenced by particle size and char particle structure, are significant in diffusion limited regimes resulting in higher carbon consumption rates.[20]

Simplifications were made in order to reduce the complexities of the model but consequentially, some questionable assumptions and their associated inaccuracies were made. A significant oversight was made when employing a single porosity and specific surface area value to capture the effects of the Zone II attributes via effectiveness factor. Inherently the effectiveness factor model assumes the effectiveness porous continuum assumption, evident from the lack of explicitly accounting for significant voids/macropores. By applying the assumption without a sufficient substitution, e.g. a representative pore size distribution, the model lacks the ability to account for macropores which may result in reduction in species penetration and the corresponding carbon consumption rate. A set uniform porosity also cannot account for spatial variation of pore size, pore growth, and local carbon consumption and the representative overall carbon consumption. In addition, the proposed model assumes insignificant Knudsen diffusion, which disagrees with previous establishes publications and understanding of Zone II properties. Similarly to Richter, the model questionably implements a steady state model to capture a naturally transient problem and the essences of its dynamics (e.g. individual pore growth and carbon consumption rate). Fundamentally the implementation of the solid

sphere raises questions regarding the fidelity of the model as all char particles have permeable pores, which are factors in any zone, arguably less important in a Zone III regime.

Chapter 3. Model Development and Implementation

The primary goal of this section is develop two char gasification models that can be used for a valid comparison to gauge the inaccuracies associated with improper utilization of the effective porous continuum assumption. One model consists of a completely unresolved char particle, represented by a simple sphere and the complete implementation of the effective porous continuum assumption that violates the length-scale constraints shown in Eq 1.1 and will be also referred to as the 2-D model. The other model consists of a partially-resolved particle with the assumption implemented solely in the unresolved microporous regions, thus satisfying the length-scale constraints and will be also referred to as the 3-D model. Subsequently, from the development and comparison of the models for a case with identical boundary conditions, insights into the particle morphology on transport in and out of the particle are gained. It may be noted that both models are developed such that physical properties, such as total volume, mass, porosity and effective diameter are equivalent.

This chapter introduces the software packages that were utilized, the coal from which the char is obtained, an explanation why this coal was chosen and the process of converting the coal into char. The unresolved, two-dimensional CFD model completely implementing the effective porous continuum assumption is developed and its boundary conditions, operating parameters, and computational methods are discussed and justified. The resolved, three-dimensional model based on a real char particle is then described and discussed. Lastly, any customizations, implemented as user-defined functions (UDFs), in both CFD models, are described.

3.1 Software Packages

To fulfill the goal of the thesis, which is to improve fundamental understanding of interactions between reaction, transport, and morphology during char gasification and to inform particle-scale submodels for reactor-scale CFD simulations, two CFD models are developed. Initially, a suitable modeling approach, either creating a CFD code or utilizing a commercial CFD software package, must be chosen. The latter was chosen in this case to avoid the additional time to create a fully developed code that can be allocated to other tasks but the remaining problem is to determine the best possible commercial CFD software package. It is noted that all programs are executed on an Exxact Corporation manufactured workstation with a 28 core Intel(R) Xeon(R) CPU E5-2690 v4. @ 2.60 GHz processor, 256 GB of RAM with a 64-bit operating system.

Of the various commercial CFD software packages, ANSYS Fluent v. 17.1 was selected. Fluent was chosen due to its ability to handle a combination of complex submodels and their user-defined parameters. This is very essential as char gasification model requires many submodels to be used in tandem, in order to have a good foundation and starting point that can be later expanded to include finer details. Out of the multiple supported capabilities of Fluent, many of the necessary capabilities for a char gasification model were readily available, such as defining porous regions, transient flow, multiple solver settings, heat transfer (e.g. conduction and convection), species transport, and multiple diffusion models (e.g. multicomponent diffusion).[4]

Although it is not possible for any CFD software package to have every possible setting, submodel, or formulation readily developed, Fluent's other advantage is that it

provides many ways to customize or add submodels that user finds lacking with relative ease. One method, which is discussed in further detail later sections, is user-defined function (UDF), which generally enables the user to create expression for properties or modify properties within Fluent. If the user requires a variable that is not readily available within Fluent, the user is able to implement a user-defined scalar to represent the desired variable, which can be solved via differential equation (ODE or PDE) within Fluent. Lastly, Fluent is able to quickly to calculate variables from given parameters for post processing or initial variable profiles via user-defined custom field.

In terms of the computation process, Fluent enables the user to use as many processing cores as the license allows, greatly reducing the required computational time, while also not being RAM intensive. Fluent can also be easily coupled with ANSYS's CAD and meshing software, reducing incompatibilities that may occur if using another CAD and/or meshing software. This is very advantageous as it streamlines the creation process of the model, more specifically in this case the two-dimensional model (which is meshed in Fluent). In addition, Fluent has many resources from tutorials, theory guides, and user manuals that reduce the required steep learning curve and the time required to be able to confidently use a software package. Overall, ANSYS Fluent is a well-established tool in industry and is continually being updated and improved upon to remain as a robust tool compared to other CFD packages.

The remaining objective that has yet to be addressed is how to represent the char structure in CFD once the particle has been captured in a CT scanner or any other method. The chosen software package that enables the resultant tagged image file format (TIFF) files to be converted into three-dimensional figure is the 3D image visualization and

processing software, Simpleware ScanIP.[61] ScanIP is often used for visualization and processing of medical images, but ScanIP's capabilities can be applied to microscopic applications such as char particles.

Although there are other 3-D image visualization and processing software, ScanIP was chosen due its many benefits. The essential benefit that justifies the use of ScanIP is its compatibility with CFD codes, including ANSYS Fluent.[25] ScanIP is first able to reconstruct the 3-D image from the CT scanner TIFF files with high quality representation and accuracy. Afterwards, ScanIP is able to easily mesh the resultant basic reconstructed geometric structure with highly customizable meshing parameters to achieve a fine and complex mesh. Its meshing capability is also versatile as it can to specify different mesh parameters for distinct regions, thus maximizing the distribution of computational resource. The resultant mesh can be exported to CFD specific software packages, including ANSYS Fluent, reducing program incompatibility issues.

In addition, physical properties, e.g. volume and surface area, from the resultant char geometry can be calculated using ScanIP, enabling calculation of CFD submodel parameters such as porosity of the unresolved micropores; this ability will be demonstrated later within the thesis. Measureable features such as distance and angles can be accomplished on specified two-dimensional planes in order for better comprehension of physical features of the particle. ScanIP also offers a user friendly interface allowing for easy navigation and promotes iterative refinement of meshing or image processing.

3.2 Coal Char Particle

3.2.1 Char Properties and Creation

Char geometric features such as voids and pores are heavily dependent on the type of coal and the heating conditions during creation of the char. In order to emphasize the effects of geometric features on gasification, a coal type that is known to result in char with high amounts of relatively large geometric features (which is not uncommon) is chosen. The chosen coal that can highlight the interplay between char structure and transport and was Illinois no. 6 coal, a bituminous coal. An example of Illinois no. 6's many geometric features was presented by Cai et. al. and is shown in Figure 1.1.[60] From Figure 1.1, large amount of voids is visible, demonstrating its potential to be used to examine the structural effects. In addition, Zygourakis conducted studies to determine the char structure of Illinois no. 6 from on the heating conditions during pyrolysis. From Zygourakis's figures shown below, it is seen that regardless of the heating conditions, Illinois no. 6 coal will result in a char with significant geometric features.[40] Only the severity of the geometric features increases as the heat conditions increases, as evident from the progression from Figure 3-1 to Figure 3-2 were the internal white regions are macropores and the black regions are the microporous regions.

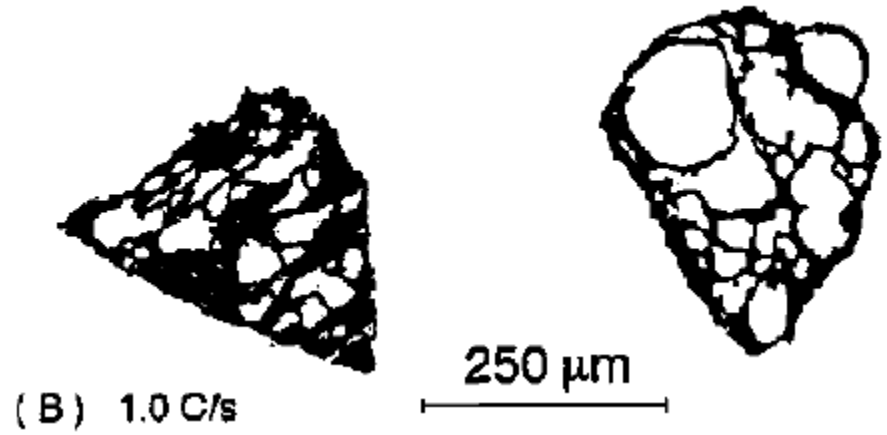

Figure 3-1. Cross-section of Illinois no. 6 Coal Char from Heating Condition 1.0 °C/s[40]

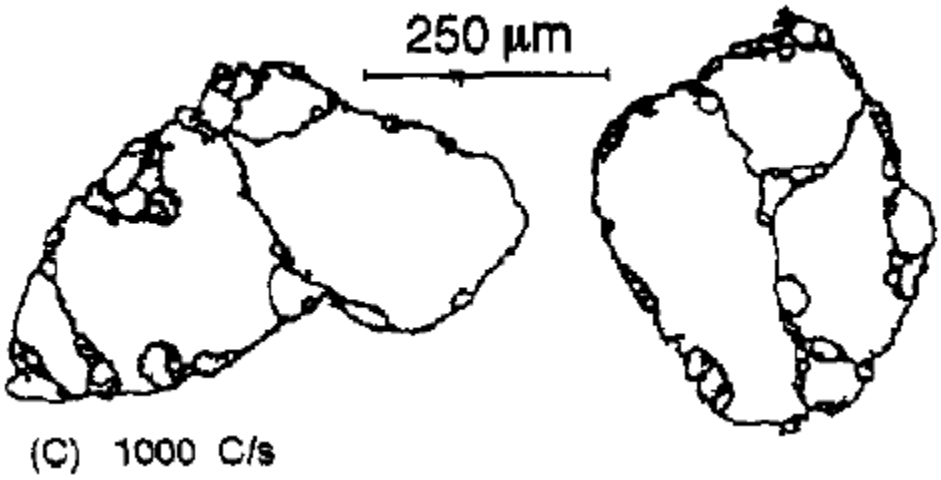

Figure 3-2. Cross-section of Illinois no. 6 Coal Char from Heating Condition 1000 °C/s[40]

The size of coal char particles varies with the reactor in which they are utilized. Entrained flow reactors typically use coal particles ground to diameters of 75 to 150 µm. Fluidized bed and moving bed reactors typically employ particles with sizes in the mm-range and cm-range, respectively. Despite the fact that this study is geared toward gasification of char

particles in an entrained flow reactor, intermediate-size coal particles were used in this study, as the chosen method of particle reconstruction, micro-CT scanners, have limited resolution, which is problematic for reconstructing “small” particles and their geometric features with accuracy. The micro-CT scanner at Marquette University has a resolution of 10 to 20 μm, which requires the use of larger particle to accurately capture particle geometric features. A viable solution to this problem is to utilize intermediate-size coal particles and scale the resultant three-dimensional image to a size comparable to those of a small char particle. This inherently assumes that the intermediate-size char particle structure is similar or the same as those of a small char particle structure. Later in the thesis, better suited solutions are presented that may be looked into in the future.

850 μm diameter bituminous Illinois no. 6 coal particles were ordered from the Penn State Coal bank and pyrolyzed at Marquette University. Dr. Zhongzhe Liu from the civil engineering department aided performed the pyrolysis of the Illinois no. 6 coal particles. The particles were pyrolyzed in the furnace at the Marquette University Water Quality Lab, which houses an electrically heated tube furnace that is currently used to pyrolyze biomass into biochar. Approximately 1.2 g of Illinois no. 6 powder is placed in the middle of steel tubing that is connected to an upstream inert gas purge system and a downstream liquid and gaseous product collection system. The steel tubing is heated resulting in the coal powder being pyrolyzed at a heating rate of 100 °C/min (approximately 1.667 °C/s) up to 800 °C in an oxygen free environment. The environment temperature of 800 °C is kept constant for approximately 20 minutes and is then cooled down to room temperature for char collection. About 0.6 g of Illinois no. 6 char is produced and then sieved through fine meshed multileveled sieves at specific size thresholds. Particles of the

desired size were gathered and carefully placed into a small lab specimen pinch and sealed transport bag.

3.2.2 Visualization Method of Char Particle

Since the resolved, three-dimensional simulation requires the real char particle geometry in order capture the nature of significant porous features, a method to capture the char particle structure must be employed. The micro-CT scanner housed at Marquette University's Olin Engineering Center and owned by Marquette University's Medical Imaging Systems Lab was used for this purpose. Micro-CT scanners capture microscopic objects with high resolution by generating X-rays that penetrate the object and magnify the "slice" or cross sectional view onto a planar X-ray detector. The detector then records the single "slice" as a TIFF file.[13] Each individual "slice" contains a greyscale pattern that directly correlates to the amount of X-rays absorbed by a certain region differentiating the materials within the slice as air does not absorb X-rays well while other solid materials naturally do (e.g. char). For example, pixels that indicate a high greyscale value (approximately white) are regions where a majority of X-rays has been absorbed, in the case of a char particle, indicate regions containing ash. When the greyscale is low (approximately black), X-rays are left unimpeded thus indicating air. When the greyscale is within the intermediate range or contain a gray color, the X-Rays are partially absorbed by the char.

The object is slightly incrementally rotated and the process is repeated until the object has completed a revolution. The resultant series of the TIFF files or slices collectively create a visual image of the object that can be further manipulated.

The micro-CT scanner at Marquette is micro-focal X-ray imaging system consisting of a Hamamatsu L9181-02 micro-focal X-ray source with a Varian 2520DX flat panel X-ray detector. The micro-CT scanner is able to achieve a maximum spatial resolution of approximately 10 to 20 microns, which is sufficient to resolve the relatively large geometric features for which volume averaging and the effective porous continuum assumption is not valid. The micro-CT scanner is set-up in a fashion that the sample, in this case the particle, will not be affected or damaged during the imaging process. The administrator and main contact for the micro-CT scanner is Dr. Taly Gilat-Schmidt. The micro-CT scanner and set-up can be seen in the Figure 3-3 below.

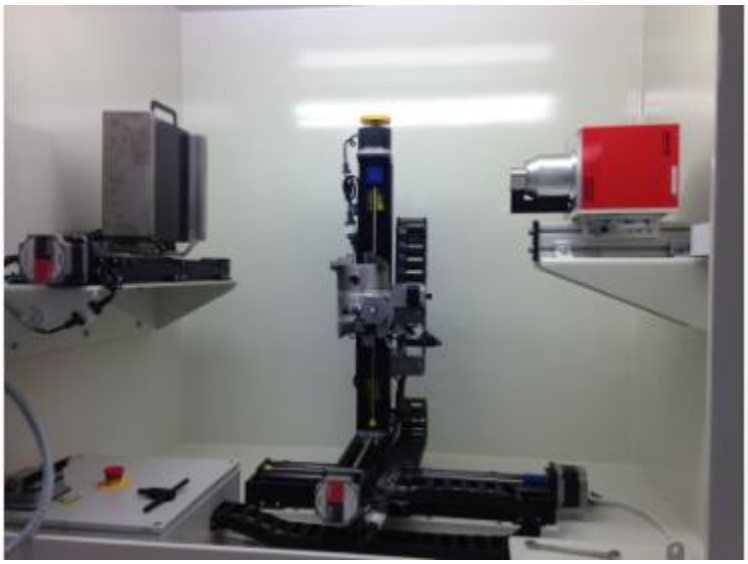

Figure 3-3. Marquette CT-Scanner[45]

The Illinois no. 6 char particles are attached to a clear cylinder apparatus by a double-sided adhesive that surrounds the cylinder's circumference. The sample particles are approximately evenly distributed on the adhesive surface. The procedure for particle placement ensures that there are few groups or clumps of particles and particles have

sufficient spacing. The cylindrical holder is shown in the Figure 3-4 below. The holder is inserted into the CT-Scanner and sensor positioning adjustments are made in order to correct sensor position, ultimately increasing imaging quality. Afterwards, the CT-Scanner's operating parameters are changed such that there are sufficient image files created to properly reconstruct the particle. The resultant 2-D TIFF files are then reconstructed and parsed into individual particles. The resultant voxel size used in this study was isotropic 20.0 microns. Each individual particle's files are sequentially labeled and placed in a separate folder that indicates the corresponding particle.

Figure 3-4 Cylindrical Particle Apparatus

3.2.3 Reconstruction of Real Char Structure

Initially, each particle's stack of TIFF files is imported into ScanIP, where the particles are first analyzed. After a quick visualization of the individual particle to ensure suitable geometric features are present and that it can be reconstructed, the particle's image domain is cropped in order to reduce unnecessary data from the surrounding regions where the particle is not present that may bog down the reconstruction process. Image processing

begins with the creation of the char particle geometry from what is referred to as a “mask” in ScanIP. A blank mask is created and named “Particle.” This is illustrated in Figure 3-5 shown below.

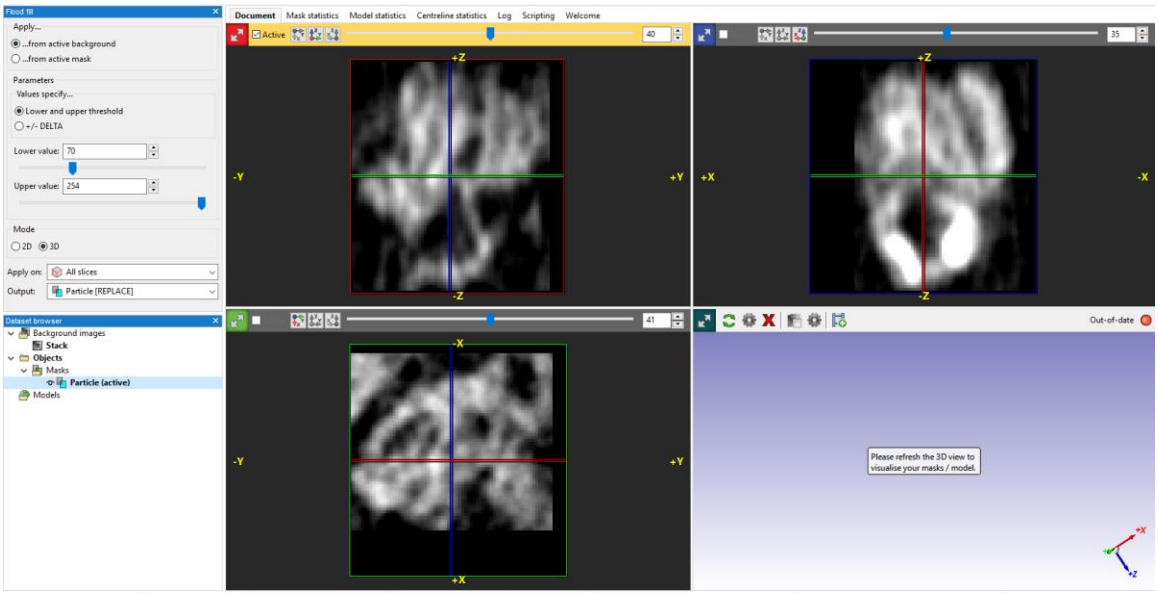

Figure 3-5. ScanIP GUI After Initialization

The mask/geometry is then assigned with the char particle geometry developed from the flood fill tool option. Flood fill creates a mask based on the connectivity from the point selected that is within the specified range of grey scale values, referred to as a threshold with ScanIP.[55] It may be noted that the threshold values from particle to particle may vary due to procedural variation within the individual particle files. The individual threshold is determined from trial and error to ensure that the particle and its individual geometric features are sufficiently resolved. The resultant char structure that is reconstructed from ScanIP is shown in Figure 3-6 below.

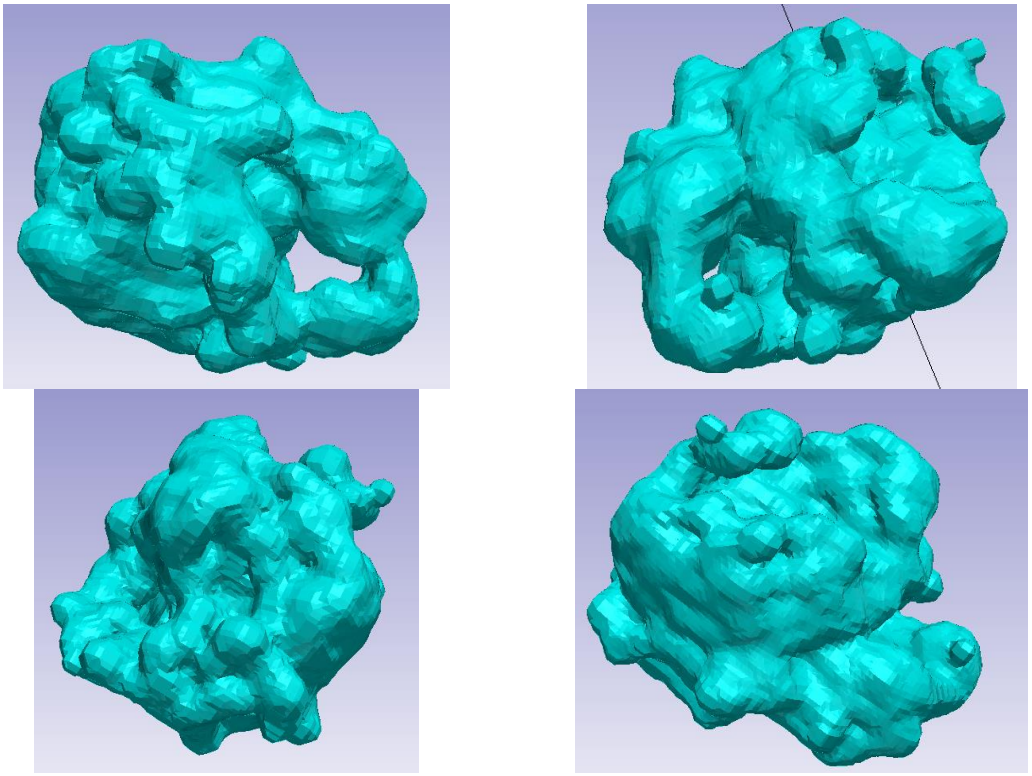

Figure 3-6 ScanIP Reconstructed Char Particle

3.2.4 Development of the Resolved Model Domain and Mesh

However, the particle geometry alone is insufficient for a CFD simulation, as a fluid domain is also required in order to capture the processes occurring in the surrounding gas. Since there is no specific fluid domain or geometry within the TIFF files, a fluid domain must be created in ScanIP. Similar to the particle mask procedure, a blank mask is initially created and named “fluid” to signify it is the fluid domain. In addition to this, the fluid mask, “fluid” is moved under the mask, “Particle” (if not already the case) in the GUI mask order as illustrated in Figure 3-7 shown below.

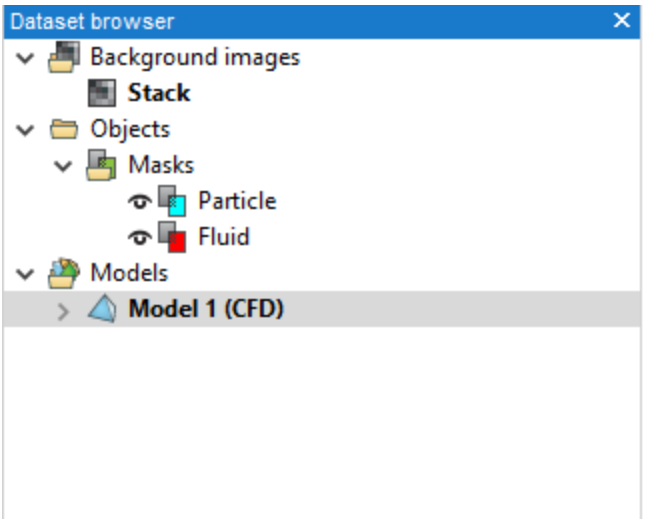

Figure 3-7. Mask Order in ScanIP GUI

This action allows ScanIP to correctly prioritize which mask takes precedence when there is spatial overlap between masks based on their sequential mask order, where the first or top ranked mask takes precedence. When spatial overlap occurs within this model, the particle will be recognized instead of the fluid geometry.

Afterwards, the fluid domain is created via the 3D editing tool, which allows the mask to be created from a combination of simple shapes. The fluid domain is a simple sphere of a specified diameter with its origin aligned with the approximate origin of the non-spherical particle. The diameter of the fluid sphere is specified to be approximately ten times the equivalent diameter of the char particle. It may be noted the available reconstruction imaging domain is expanded via the image processing tool, “Pad,” which expands on the current image domain by adding a user specified volume of the minimum greyscale value of zero.[61]

Once both the fluid and particle domains have been created from the previously stated procedure, the domains must be meshed for CFD simulation. Initially, a CFD mesh in ScanIP is created and the export type is specified as “Fluent volume”, indicating the program for which the mesh is intended. Afterwards, the masks are simply placed into the model in the same mask order, “Particle”, then “Fluid”, in order to retain the defined priority when spatial overlap occurs. In the model configurations, the boundary conditions of the model are first defined from the boundary conditions chosen during the meshing phase. The only defined boundary condition is the outer face of the fluid sphere, referred to as “fluid-Background” within ScanIP, which is defined as a pressure outlet boundary condition. Since the remaining boundary conditions that are left undefined, by default, ScanIP assigns the undefined boundary conditions as “wall” boundary conditions. If necessary, unsuitable defaulted wall boundary conditions are changed in Fluent. The entire CFD model material type is defined as “fluid”, as the fluid domain contains the ambient surrounding gaseous mixture, and the particle is a porous region that Fluent considers to be a fluid.

In order to be as computationally efficient as possible, the balance between accuracy and computational effort must be addressed in the model configuration meshing parameters. Since most of the gradients occur within the particle during gasification, the particle and fluid domains are meshed with different meshing parameters to better resolve the particle domain using a finer mesh, while using a coarser mesh for the fluid domain. Trial and error testing on the mesh sizes was done in order to determine a suitable mesh size that allows for sufficient accuracy while being computationally efficient. The chosen

ScanIP meshing parameters that were specified for the "base case" are shown in Table 3.1 and the resultant cross-section of the resultant mesh is displayed in Figure 3-8.

Table 3.1 Final ScanIP Meshing Parameters

Meshing Parameters	Particle Domain	Fluid Domain
Target Minimum Edge Length (mm)	0.0198	0.07
Target Maximum Error (mm)	0.002	0.003
Maximum Edge Length (mm)	0.0452	0.2
Surface Change Rate	14	70
Volume Internal Change Rate	30	60

Figure 3-8. Cross-Section of Final Three-Dimensional Mesh, Fluid – Red, Particle – Blue

To finalize the meshing parameters in Table 3.1, a mesh refinement and optimization study was conducted but this procedure is discussed in depth in Section 3.3.2. A brief overview of this mesh study is a set of distinct meshes (quantified by the number of total meshing elements in both fluid and particle regions) were applied to the developed CFD model set-

up and simulated. From the results, semi-global metrics are gathered and used to gauge the relative performance via relative error of each mesh. Table 3.2 pertains to the meshes used and the resultant semi-global metrics gathered. It may be noted that since there is minor computational time difference between Grid 3 and 4, thus the finest mesh is selected.

Table 3.2 Three-Dimensional Mesh Study

Grid	Meshing Elements	Max Porosity Relative Error (%)	Max Conversion Relative Error (%)
1	500,000	3.418240548	15.75024125
2	723,000	1.91298108	8.914977675
3	940,000	1.037603693	4.720521647
4	***1,200,00***	-	-

Afterwards, any possible complications associated with randomly disconnected mesh cells from the main zone or irregularities are located and are addressed before importing the mesh into Fluent. Initially, the meshed domains are separated into distinct entities via the image processing tool, “Boolean segmentation.” The individual voxel counts of distinct zones are then calculated and sorted via the mask statistics tool, highlighting problematic isolated zones, evident from small voxel counts values. Small voxel counts zones indicate problematic cells that will render the mesh useless as these respective individual zones may harbor cells that are impractical, such as cells with no associated volumes. Distinct zones with voxel counts less than 1000 voxels are deleted. The mesh is then recreated from the same meshing parameters. This process is repeated until no distinct zones show low voxel counts, and the mesh is exported to CFD.

3.2.5 Calculation of Unresolved Initial Porosity

To ensure a valid comparison between the 2-D (unresolved) and the 3-D (resolved) models, the initial mass, total porosity and total volume must be the same for each model. The initial porosity of the *unresolved*, microporous regions of the 3-D particle surrounding the resolved voids will therefore differ from the initial porosity of two-dimensional case to account for the porosity occupied by the voids and the resolved macropores. The total porosity of the char particle is taken to be 0.68 based on work of Zygourakis and the previously stated pyrolysis heating conditions.[40] Before any calculations regarding initial porosity adjustment are performed, a scaling procedure to scale down the entire resolved domain to match the domain size of the two-dimensional model must be implemented. A scaling ratio, $\Re_s$, was chosen to be the ratio of the two-dimensional particle diameter to an equivalent diameter of the resolved particle and is shown in the expression below where d_{2D} is the previously specified diameter of 100 microns and d_{3D} is the effective diameter of the resolved particle (including resolved macroporous regions).

$$\Re_s = \frac{d_{2D}}{d_{3D}} \tag{3.1}$$

Calculation of the equivalent diameter of the 3-D char particle can be accomplished by various methods, relying on physical properties or features that result in varying equivalent diameters.[42] The chosen sizing method is the equivalent volumetric diameter, which determines the equivalent diameter for the corresponding volume if the geometry were to be a perfect sphere. Of the several of sizing methods, this method was chosen since the two-dimensional model is spherical, so for a good comparison, the equivalent diameter

should also be derived for a hypothetical spherical geometry. The following expression is the volumetric diameter obtained from the $V_{3D,tol}$, the total volume (resolved macropores and microporous regions) of the resolved particle.[42]

$$d_{3D} = \left(\frac{6V_{3D,tol}}{\pi}\right)^{1/3} \tag{3.2}$$

This expression serves as a standard formulation that can be applied to any analyzed char particle, reducing any further variance between particles in future work. The expression only requires the total volume of the resolved voids plus the unresolved microporous regions that can be obtained easily within Fluent via a "volume monitor." Scaling down the entire domain by the diameter ratio not only forces both particle domains in the two-dimensional and the three-dimensional models to be of similar sizes, but it also forces both total particle volumes (3-D: resolved structure + macropore volumes & 2-D: unresolved structure) to be equal. This was confirmed from the Fluent three-dimensional volume being equal to the spherical volume of the two-dimensional model after all scaling was accomplished.

Once the entire domain has been scaled down by the diameter ratio, the resultant volumes are utilized to derive the 3-D char particle's microporous initial porosity first using the definition of the total initial porosity expression below, based on the fact that the total porosity is defined as the fraction of void volume to total volume. It may be also noted that the total initial porosity is also equivalent to 2-D char particle initial porosity due to the 2-D model's microporous region contains all pore sizes.

$$\varepsilon_{total,o} = \frac{V_{micro/meso} + V_{macro}}{V_{total,p}} \tag{3.3}$$

The variables in this expression are $V_{total,particle,}$ the volume of the unresolved solid regions and void/macropore volume, $V_{macro\ ,}$ which is the void/macropore volume, and $\varepsilon_{total,o}$ which is the total initial porosity that is readily chosen based on the heating rate and Zygourakis and is also used in the two-dimensional case. The remaining variable, $V_{micro/meso}$ (volume occupied from the micropores and mesopores) can be algebraically solved. $V_{micro/meso}$ is then utilized to determine the initial porosity of the *unresolved regions* of 3-D model from the expression below.

$$\varepsilon_{3D,u,o} = \frac{V_{micro/meso}}{V_{3D,u}} \tag{3.4}$$

Since the 3-D unresolved initial porosity are modified relative to the 2-D model, the particle masses that reside in the both models' unresolved region should be equivalent if done correctly. The proof that indicates that both models' total masses are equivalent is shown below. It is emphasized that the 2-D unresolved particle volume is equivalent to the total volume (resolved macropores and micro-porous regions) of the 3-D particle, which includes both the unresolved microporous regions and the resolved macropores. The proof begins with an expression that equates the particle mass residing in the unresolved regions of both models. It is emphasized that since only the unresolved volumes are utilized, the volumes are not equivalent as only the total volumes are equivalent.

$$\rho_t V_{3D,u}\left(1 - \varepsilon_{3D,u,o}\right) = \rho_t V_{2D}(1 - \varepsilon_{2D,o}) \tag{3.5}$$

The initial porosity of the unresolved region in the 3-D model is isolated on the left hand side. Please note that both true densities or pure char density cancel out. As a side note, the true density properties are illustrated in Section 3.3.4 Table 3.7.

$$\varepsilon_{3D,u,o} = 1 - \frac{V_{2D}}{V_{3D,u}}(1 - \varepsilon_{2D,o}) \tag{3.6}$$

Further manipulation is done to the right hand side such that the 2-D unresolved particle volume is substituted with its stated definition (from the beginning of the proof) and the 2-D unresolved porosity is factored out.

$$\varepsilon_{3D,u,o} = \varepsilon_{2D,o}\left(1 + \frac{V_{macro}}{V_{3D,u}}\right) - \frac{V_{macro}}{V_{3D,u}} \tag{3.7}$$

Each porosity is substituted with its respective volume definition as stated in the previous expressions earlier in this section.

$$\frac{V_{micro/meso}}{V_{3D,u}} = \frac{V_{micro/meso} + V_{macro}}{V_{3D,u} + V_{macro}}\left(1 + \frac{V_{macro}}{V_{3D,u}}\right) - \frac{V_{macro}}{V_{3D,u}} \tag{3.8}$$

Finally, the expression above is manipulated such that all the terms cancel, proving that the original conservation equation is true.

$$V_{micro/meso} + \frac{V_{macro}V_{micro/meso}}{V_{3D,u}} + V_{macro} \tag{3.9}$$

$$= V_{micro/meso} + \frac{V_{macro}V_{micro/meso}}{V_{3D,u}} + V_{macro}$$

$$0 = 0 \tag{3.10}$$

Ultimately since the physical properties diameter/equivalent diameter, volume, total porosity and mass are consistent between the models, the comparison between the two-dimensional and the three-dimensional models is appropriate and any differences from the simulation results can be attributed to the presence, distribution and size of the large voids and macropores in the 3-D simulation.

To obtain the required values in the expressions above, the reconstructed figure is further expanded. The volume of the macropores in the 3-D model is determined by applying the image processing tool, “Close,” on a duplicate mask of the developed particle structure. “Close” performs a morphological close to a targeted existing mask based on some inputted parameters that govern how holes, in this case macropores, are closed.[55] Input parameters of the "Close” tool primarily consist of pixels of structuring elements in this specific case, a cubic structuring element of 5 pixels. The “Close” tool input parameters were determined from a visual check of the 3-D figure and all cross sectional planes to ensure that all types of resolved macrospores defined by Rouqurol et al. are captured within the macropore mask.[36] The duplicate particle mask is ordered such that the duplicate mask is below the Particle mask and above the Fluid mask. This order allows ScanIP to isolate

the new corresponding macroscopic volume from the “Close” tool and exclude the char particle volume while taking precedence over the fluid domain. The resultant char particle and the macropore occupied volume is demonstrated below. Please note that the figures from Figure 3-9 were obtained from the same views as Figure 3-6 in order for easier visual comparison.

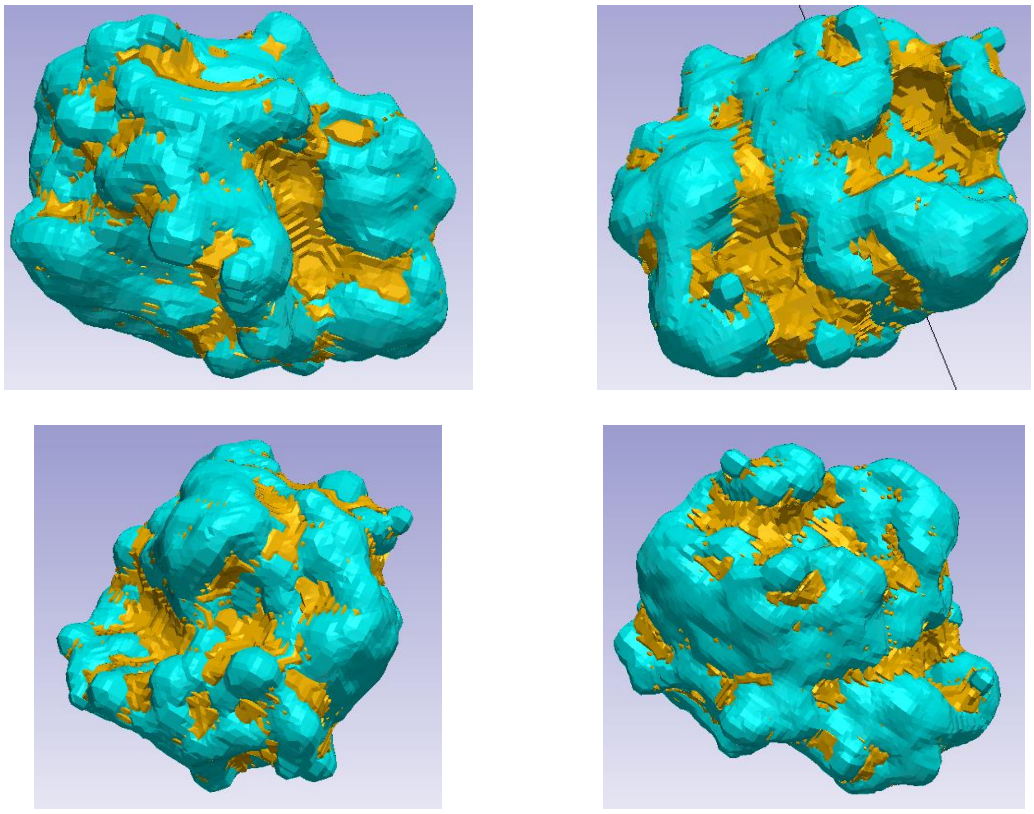

Figure 3-9. ScanIP Reconstructed Char Particle (Blue) with Calculated Macropore Volume (Gold Orange)

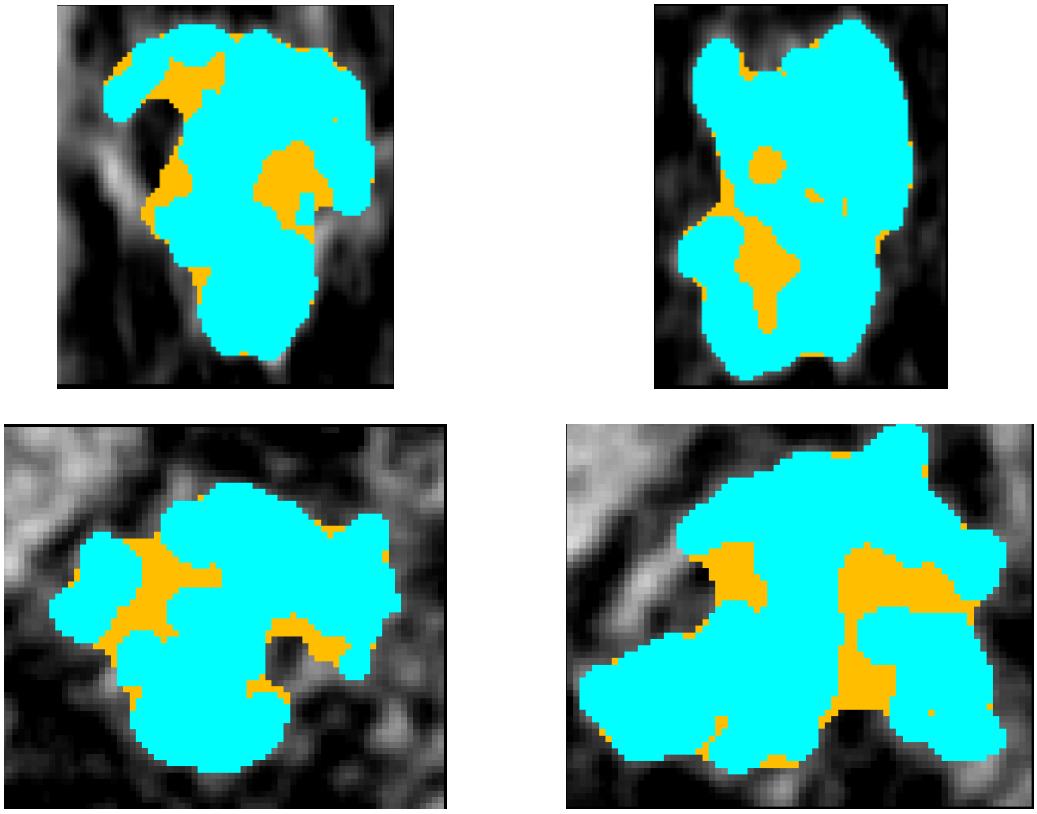

Figure 3-10 Cross Sections of Particle (Blue) with Macropore Volume (Gold Orange)

Once this is accomplished, the macropore mask is placed within the duplicate copy of the CFD mesh and ordered in the same fashion as in the mask GUI. The meshing parameters of the macropore mask uses the same meshing parameters as the original particle mask to remain consistent. A new CFD mesh is created with the three masks using the previously stated meshing procedure in Section 3.2.4 and imported into Fluent. Upon initializing Fluent with the new mesh, the domain is immediately corrected due to the assumed defaulted mesh creation units of meters to its correct units, millimeters. Within Fluent, both the particle and macropore domains had their respective volumes calculated. Afterwards, the previously developed scaling ratio is applied to the entire domain in all three coordinates, X, Y, and Z. The volumes are again computed using Fluent volume

monitors to determine the recalibrated initial porosity for the unresolved regions of the resolved char particle. Although determining the mask volumes is well within ScanIP's capabilities, the process of creating and importing the mesh into Fluent may cause the volume values to slightly vary from the values determined within ScanIP. In addition, obtaining all property values within the simulation domain is good practice and will allow for retention of high accuracy.

3.3 CFD Model Development

To analyze the effects of char particle structure, two separate models are developed, a two-dimensional and a three-dimensional model. The two-dimensional model implements the questionable effective porous continuum assumption in an unresolved homogeneous char structure geometry represented by a simple sphere. The three-dimensional model implements the effective porous continuum assumption only in the microporous regions surrounding the resolved large pores. Both models implement the same boundary conditions in order to perform a valid comparison.

3.3.1 2-D CFD Model Development - Geometry

The two-dimensional model is created for comparison and to serve as a foundation for the development of the three-dimensional model. It is advantageous to begin the work with the two-dimensional model as its creation process is overall easier. Taking advantage of the low number of mesh elements in a two-dimensional case relative to three-dimensional case allows for an efficient determination of aspects of the CFD model, such as reaction and transport submodels and boundary conditions. In addition, spherical domains, typically used to represent char particles, are advantageous, as they can be easily

defined and represented by an axisymmetric semicircle, with the straight face defined as an axis on any plane. This greatly reduces the computational domain, resulting in fewer total meshing cells, ultimately increasing the computational efficiency and speed.

A Fluent analysis system, an ordered group of software packages, is selected and placed on the open space in the project schematic in Workbench. Since the software packages are ordered in such a fashion that requires any preceding software to be developed, the initial software package, DesignModeler must be used and developed. DesignModeler is ANSYS CAD development software, which enables the development of three or two-dimensional figures. The Workbench GUI and a single Fluent analysis system is displayed in Figure 3-11 below.

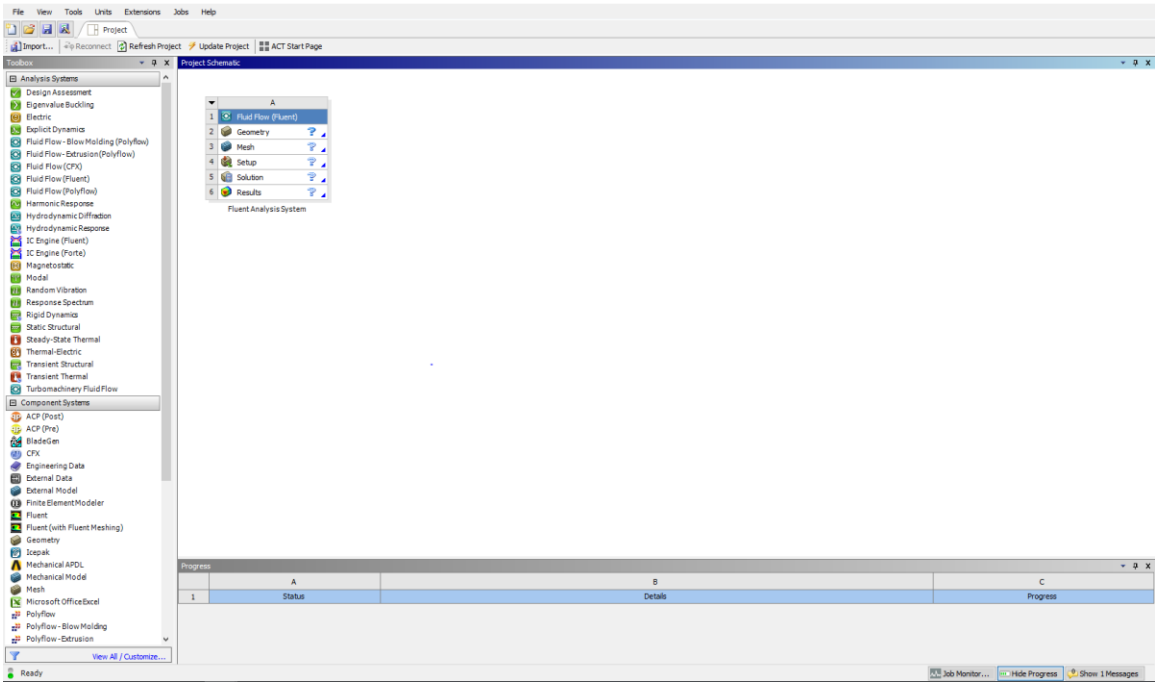

Figure 3-11. Workbench GUI and a Single Fluent Analysis System

Once the DesignModeler is initialized, the operating measuring unit is checked and changed to microns to match the particle length scale. As previously stated, the unresolved geometry is developed as a two-dimensional model. The char particle domain is a simple sphere, and the surrounding fluid domain is also defined to be a sphere, with the diameter being ten times that of the particle diameter, allowing for the boundary condition at infinity to be sufficiently far from the particle surface. Although there is a range of char particle diameters that are produced in a gasification environment, a 100-micron diameter particle is well within this range and is chosen as the particle diameter.

The semicircular fluid domain is sketched with the center aligned to the origin of the arbitrarily chosen sketch plane. Afterwards, the 100-micron diameter circle centered at the plane's origin is subtracted from the fluid domain, due the DesignModeler's inability to handle overlapping geometries. A surface (plane) is created from the fluid sketch from the tool, "Surface from sketches." The particle sketch is then created on the same plane and in a fashion so that it coincides with the fluid surface body and perfectly fits. From the particle sketch, a surface body is created from the tool "Surface from sketches" but the option of "frozen" is enabled so DesignModeler can differentiate the two bodies. The resultant two-dimensional geometry is shown in Figure 3-12. Please note the geometries are differentiated by color, indicating that DesignModeler correctly identifies two distinct bodies. The blue and gray geometries indicate the particle and fluid domains, respectively.

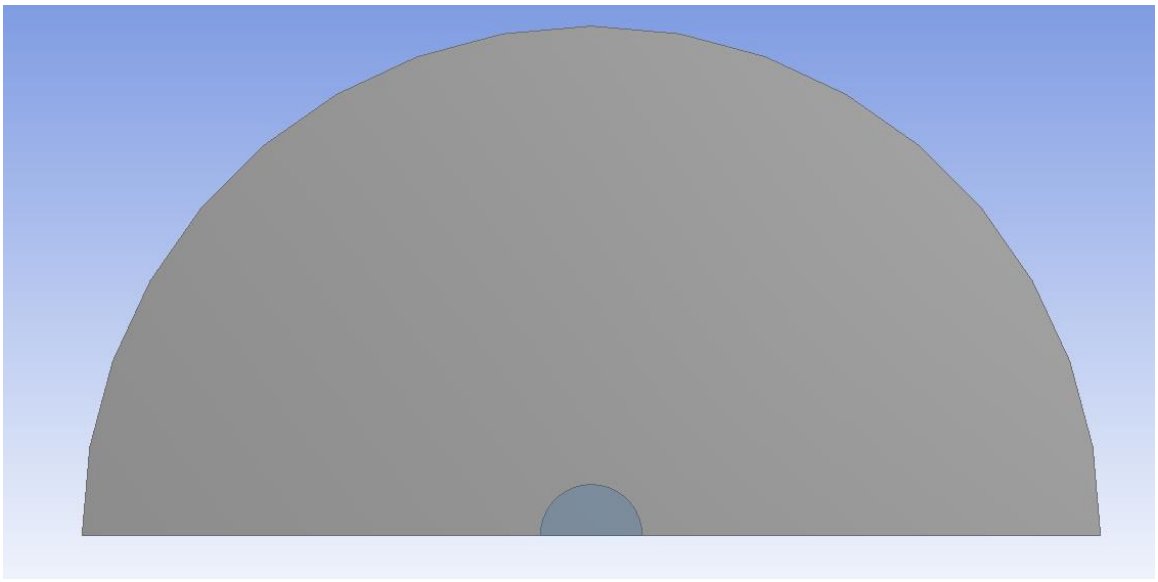

Figure 3-12. Resultant Geometry of the Two-Dimensional Model

Finally, each of the geometries are defined as fluid zones. This step translates into Fluent where both zones will subsequently be defined as fluid. It may be noted that the particle is also defined as a fluid zone, as Fluent recognizes porous regions as fluid zones. This property can be changed in the "Details View" of the resultant surface bodies. As a side note, defining the geometry faces are not done during this phase, but during the meshing phase.

3.3.2 2-D CFD Model Development - Mesh

The next objective is to develop the mesh for the two-dimensional model. This can be problematic as the balance between the number of elements and computational cost must be balanced in order reach maximum efficiency while minimizing error. To maximize computational efficiency, more resources (mesh elements) are distributed to high priority regions compared to low priority regions. This implies more mesh elements are placed in

areas surrounding and within the particle and comparatively fewer in the remaining areas. Meshing resources are needed in these regions in order to sufficiently resolve gradients that typically form within or around the particle region. Fewer resources are needed in the remaining fluid region due to the region reaching an approximate steady-state after the short transient period that is required after the first initial time steps, thus minimal gradients occur in this region.

The final meshing parameters for both the two-dimensional and three-dimensional models were obtained through refinement and optimization study. This process is problematic due to the fact that there are a vast number of meshing combinations, with a wide range of meshing elements and profiles that can be applied to a given CFD setting (e.g. time step and iterations per time step). To systematically sieve through many combinations, a meticulous yet simplistic procedure is employed for the purpose of determining a sufficient mesh while maintaining computational efficiency in mind.

The procedure is based on a convergence study in which some semi-global metrics, such as volume averaged porosity and conversion are obtained from a finalized Fluent simulation with a set of different meshes. It may be noted that all meshes use the same refinement tools and locations discussed later in the section. For simplicity, each mesh is quantified by its number of elements, due to the difficulties of quantifying the unique features and profiles of each individual mesh. Once each mesh has been developed, the mesh undergoes the respective CFD simulation and the semi-global metrics at the end of each time step are recorded. Also note that all meshes pass Fluent's mesh checker and are further refined if they do not pass. It is assumed that the finest mesh is the "exact" value, as it is theoretically the most conservative case, and every other mesh has its respective

relative error calculated for all time steps. Based on the maximum relative error and the number of meshing elements, a mesh is chosen with confidence, keeping in mind the tradeoff between computational requirements and accuracy. Table 3.3 show the results for the two-dimensional convergence study with the bold text indicating the chosen mesh. It may be noted that between grids 1 and 2, the porosity error slightly increased even though the number of meshing elements has increased. The can be explained as the size function was between the two grids are different. The three-dimensional mesh study can be seen in Table 3.2

Table 3.3. Two-Dimensional Mesh Study

Grid	Meshing Elements	Max Porosity Relative Error (%)	Max Conversion Relative Error (%)
1	14,451	0.895766972	8.046998806
2	77,713	1.114923258	6.589950065
3	***95,506***	***0.630947223***	***3.528885059***
4	120,423	-	-

The final iterative meshing parameters utilized in ANSYS meshing are displayed in the Table 3.4 below along with the resultant meshed domain.

Table 3.4 Final Two-Dimensional Meshing Parameters

Variable	Option
Size Function	Curvature
Relevance Center	Fine
Smoothing	Fine
Min Size	1.25e-05 µm
Max Face Size	2.250 µm
Max Tet Size	3.250 µm
Growth Rate	1.50

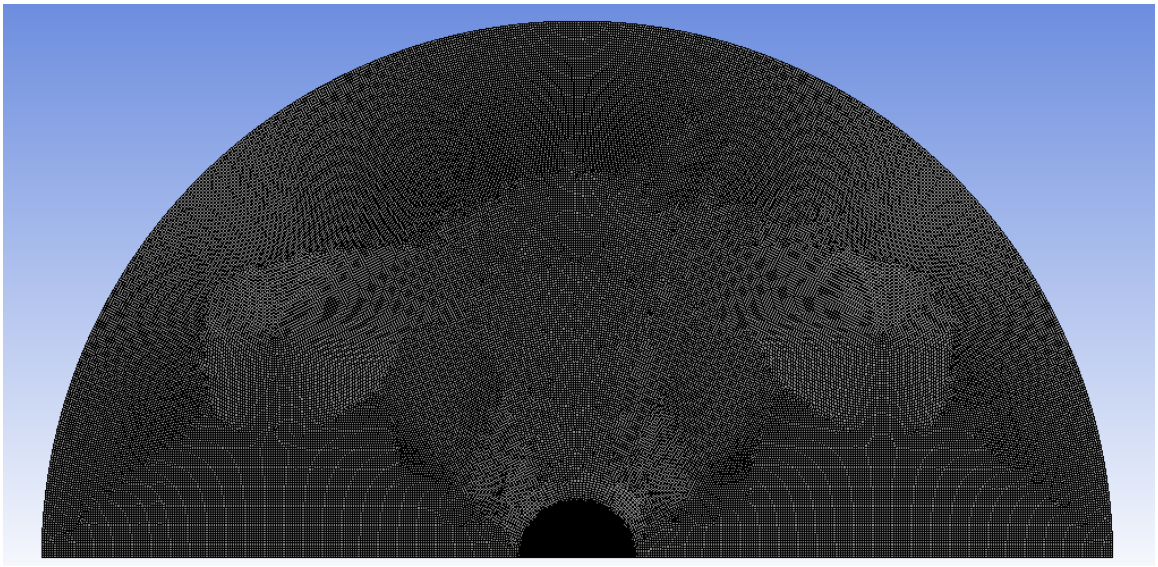

Figure 3-13. Final Two-Dimensional Meshed Domain

In the Fluent analysis system sequential order, meshing the two-dimensional model is required before proceeding to the CFD model set-up. In this section, meshing of the two-dimensional model is carefully described and the boundaries are defined. Defining the distinct bodies and the boundary conditions are first addressed to reduce confusion. Each body is individually selected using the "face" selection filter and had its surface geometry defined via "Create Name Selection". This option brings a dialog box which enables the face to be assigned a name and creates a geometric face. This procedure is repeated until both bodies have been defined. In good practice, in the geometry section, the corresponding geometries are also relabeled to align with their respective domain.

The remaining task is to assign labels to the boundary conditions. The "edge" filter is selected to easily select the desired edges. Once the desired edge is selected, the option "Create Name Selection" is selected and the same procedure from the domains are again repeated. This procedure is followed until all desired edges are assigned a corresponding

label. Edges that were labeled are, “Pressure_outlet”, “Axis”, “interface1”, and “interface2”. The named selection, “Pressure_outlet” is assigned to the outer edge of the entire domain to represent the pressure outlet boundary condition which will be discussed in detail in the CFD set-up portion. “Axis” is assigned to the diameter of the semicircle to indicate the axisymmetric axis. “Interface1” and “Interface2” are located at contacting edges between the fluid and particle and vice versa. The purpose of these two selections is to be able to create a mesh interface in Fluent giving the ability to separately mesh each domain and will be further explained in the coming content. A visual recap of all the named selections created is shown in the Figure 3-14.

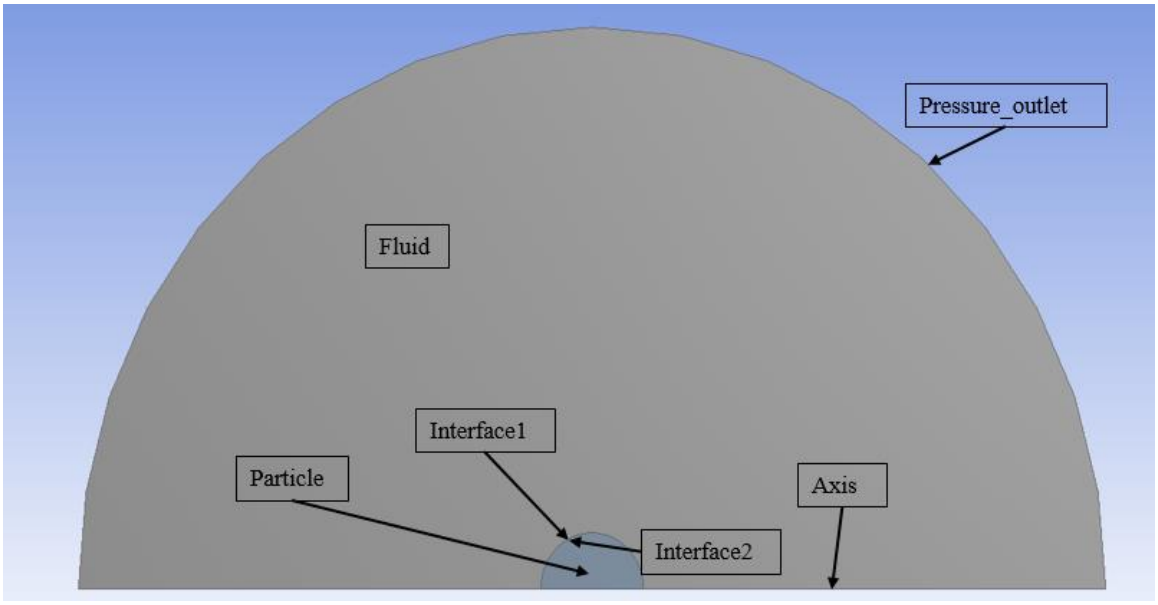

Figure 3-14. Visual Recap of Named Selection for Two-Dimensional Model

Afterwards, the whole domain must be meshed. Capturing the area surrounding the particle’s circumference is accomplished from the local meshing tool, “refinement”. Refinement is used to specify the maximum number of meshing refinements to surrounding areas of certain face, edge, and vertex ranging from a scale of 1 to 3. 1 represents minimal

refinement while 3 is the maximum refinement to the local region.[8] The refinement tool is applied to edges that were previously labeled as “Interface1” and “Interface2” both at the refinement scale 3. Applying refinement to both edges results in a finer mesh on the outer and inner regions surrounding the fluid and particle contact region, which greatly aids in resolving this region. Once accomplished, the resultant meshing parameters determined from the convergence study are utilized for the mesh. Lastly, the meshes are checked for quality within Fluent. If the mesh fails the quality check within Fluent, indicating an inadequate mesh, then the mesh is further refined until Fluent’s diagnostics indicates otherwise.

3.3.3 Fluent Model Theory

3.3.3.1 Species and Reaction Rates

Before any additional actions are taken to further develop the CFD model, such as enabling submodels, it is important to first understand what is required in a char gasification model. As a side note, in this section, only the theoretical portion that is directly implemented within Fluent without any additional customization is discussed. Any other required theories or expressions that are implemented via customization are discussed in the Section 3.4. The first aspect to address is what species are produced and consumed in the process of gasification. During char gasification studies CO_2 and H_2O are the reactant species and CO and H_2 are the products. The gasification reactions are shown below.

$$C + CO_2 \rightarrow 2CO \quad \text{(R1)}$$

$$C + H_2O \rightarrow CO + H_2 \quad \text{(R2)}$$

The main issue regarding the reaction kinetics is specifying a representative gasification reaction rate expression, R1 and R2, that best characterizes the particle consumption. The difficulty stems from the vast amount of gasification kinetics resulting from varying experimental set-ups that are only valid within a certain range of operating parameters. In order to choose the most representative case, the gasification kinetics and their resultant reaction rate expressions must pass the stated criteria.

1. Valid within the chosen ambient temperature, 1800K
2. Valid for the operating pressure of 2 MPa
3. Include a physical property that is a function of conversion or porosity
4. Gasification kinetics and expressions must be derived from coal char
5. Gasification kinetics are obtained from only CO_2 and H_2O gasification in an entrained flow gasifier
6. Gasification kinetics are undistorted by char structure/ must be obtained in Zone I

After sieving through many works/studies regarding the gasification kinetics and determining if the kinetic data satisfies the criteria, the reactions developed from Tremel were selected. The operating ranges that the reaction rate expressions are valid in are pressures up to 2.5 MPa and temperatures up to 1873 K.[10] The developed *intrinsic* gasification reaction rates also includes the physical property, specific volume, which naturally decays as porosity increases, allowing the reactions to correctly diminish as the simulation progresses. All data was gathered from an entrained gasifier, more specifically, pressurized entrained flow reactor. In addition, the study was conducted regarding H_2O and CO_2 gasification of an unknown coal char where gasification experimental data was

gathered from a thermogravimetric analysis and existing char surface data. The developed Tremel intrinsic reaction rate expression is illustrated below where P_i is the partial pressure of the ith species. It may be noted that the expression below is not valid within the reaction rate framework within Fluent, thus is applied to the CFD models via customization methods. This is discussed in detail in Section 3.4.3.

$$\Re_i = AS_g P_i^n e^{-\frac{E_a}{R_u T}} \tag{3.11}$$

Tremel provides values for the reaction rate variables, primarily pre-exponential factor and activation energy, for each reaction and if listed, the temperature the *intrinsic* gasification was obtained from. The Tremel gasification reaction rate variables are displayed in the Table 3.5 below.

Table 3.5 Tremel Gasification Reaction Rates Parameters

Reaction	Pre-Exponential Factor (g/ (m^2 s MPa^n)	Activation Energy (kJ mol^{-1})	Order	Derived Temperature (°C)	Ref.
R3	7.5 * 10^3	200	0.41	1600	[10]
R4	144.8 * 10^3	212	0.41	1600	[10]

To further improve the realism of the model, an annealing factor that was also applied in other models are applied to the current model.[54] More specifically, an annealing factor of approximately 0.5725 is applied to both gasification reaction pre-exponential factors which reduces the potency of the reaction rates. Annealing is a chemical phenomenon in which the initial devolatilization or pyrolysis of the char particle reduces the possible surface areas where gasification can occur on thus reducing the reaction rate.

This factor was derived from Tremel operating conditions and the initial conditions upon char entering a gasifier and the residence time under these conditions. The initial entrance temperature was obtained from Botero of a value of 2273 K and if assuming the particle travels linearly through entrance conditions, the time that the particle is under the gasifier entrance conditions was calculated to be approximately 0.1617 seconds. This value assumes the entrance conditions occupy a distance of approximately 0.5 meters from the entrance or top according to Botero whom conducted research regarding Illinois no. 6 char gasification from H_2O and CO_2 slurries resulting in temperature and species profiles within the gasifier.[14]

Lastly, the expression shown in Eq. 3.11 requires a specific volume but since the specific volumes that were listed from Tremel have no associated coal type, the specific volumes are not applicable or representative of Illinois no. 6 char. In the case of Illinois no. 6 char, there are a wide range of acceptable specific volumes as a result of varying measuring techniques. Having such a wide specific volume range, a value of 480 m^2/g is chosen with good faith. To capture the transient nature of a particle undergoing gasification, it is important to include an expression within the gasification reaction rate expression that represents the current state of the particle and its available local surface area per volume. The chosen expression is “1-X”, which represents the fraction of available specific surface area remaining in the unresolved regions of the 3-D particle and the complete 2-D particle. The factor is the percent representation of remaining available char for gasification and is characterized by the simple expression, 1-X. It may be noted that other similar but yet complicated expressions are applied to other studies, and could easily be incorporated.

Although gasification is primarily characterized by heterogeneous reactions, exclusion of the homogeneous reactions, primarily water-gas shift, is not valid nor realistic. At high operating temperatures and pressures, the effect of the water-gas shift reactions is amplified at initial times before the surrounding ambient environment has settled and reached equilibrium. Consequentially, the water-gas shift reactions will change the surrounding water vapor and carbon dioxide concentrations. The forward and backward water-gas shift reactions are displayed below. Below the reaction is Table 3.6 containing the water-gas shift kinetics that was used by Richter to model gasification of a porous representation.[9] Please note that the kinetics are within the temperature modified Arrhenius framework.

$$CO + H_2O \rightarrow CO_2 + H_2 \quad \text{(R3)}$$

$$CO_2 + H_2 \rightarrow CO + H_2O \quad \text{(R4)}$$

Table 3.6 Homogeneous Reaction Rate Parameters

Reaction	Pre-Exponential Factor (m^3 $kmol^{-1}$ s^{-1})	Activation Energy (J $kmol^{-1}$)	Order	Ref.
R1	2.74e+09	8.36e+07	0	[9]
R2	9.98e+10	1.205e+08	0	[9]

3.3.3.2 Radiative Effects

Lastly, another possible driving gasification factor, radiation, must be examined. Radiation can affect gasification rates as the both the fluid within the gasifier and the char particles are operating under high temperature range causing for the slightest temperature difference to be greatly amplified and result in heat transfer to the lower temperature

particle. The particle is naturally a lower temperature, as both gasification reactions are endothermic, causing the particle to act as a sink for the heat transfer. This model ignores radiation effects similar to other gasification model, such as the proposed model from Cai.[60] Radiation in this model is assumed to be negligible, as the particle of interest is assumed to be surrounded by many other similar particles resulting in radiative heat transfer to be dominated by particle to particle interactions. Since the particles are assumed to be at similar temperatures, the temperature difference is minimal, thus little to no net radiative heat transfer occurs.

3.3.3.3 Boundary Conditions

Since the char particles of interest are assumed to be within an entrained gasifier, the surrounding fluid's characteristics that the particle is swept with must be determined. Aspects that need to be determined are the operating pressure, the mole fraction of each species, and the temperature of the fluid. Since the particle of interest is also assumed to be within entrained flow or minimal imposed relative velocity, it can also be safely assumed that particle is relatively far from the gasifier entrance (high relative velocity region). Gathered ambient environment specifications were also obtained from Botero et al. In this case, the ambient environment was derived from a study regarding the entrained gasification of an H_2O slurry, whose resultant species and temperature profiles at a specified location relatively far from the gasifier entrance are used (approximately 6m away from the top) to better reflect where the majority of gasification takes place. It is also reiterated that the exclusion of oxygen is justified as most oxygen is consumed upon initial entrance of the gasifier as shown from Botero.[14]

Table 3.7 Surrounding Fluid Characteristics

Specification	Value
Temperature (K)	1800
H_2 Molar Fraction (-)	0.28
H_2O Molar Fraction (-)	0.21
CO_2 Molar Fraction (-)	0.12
CO Molar Fraction (-)	0.39

To improve gasification rates to accelerate the amount of syngas produced, an entrained gasifier's operating pressure always is amplified. Knowing so, and from analyzing studies regarding entrained gasifiers with the characteristics (e.g. species), an operating pressure of 2 MPa was chosen.[10,14,28] With the augmentation of the operating pressure, the density obtained from the ideal gas law is the following expression from the Fluent User's Manual.[7]

$$\rho = \frac{p_{op} + p_g}{\frac{R_u}{MW_m} T} \tag{3.12}$$

It may be noted that the additional pressure term is the gauge pressure but since the gauge is significantly lower than the operating pressure (by approximately 5 magnitudes), this term is negligible.

The last variable that is required for the simulation are the initial porosities of the unresolved and resolved particles. Although the values have been discussed in depth in Section 3.2.5, the initial unresolved/2-D porosity was chosen to be 0.68, which was chosen based off the heating rate and Zygourakis work.[40] The same 2-D initial porosity is applied to the 3-D microporous region (unresolved region) and then recalibrated corresponding to

amount of the resolved macropores volume. This resultant initial porosity in the 3-D microporous region is 0.638.

3.3.3.4 Mass Transport – Diffusion and Viscous Resistance

It is very evident that the pore diameters have a significant impact on the transport within the char particle and is not explicitly accounted for in any of the Fluent standard features. To improve on this weakness, the permeability is redefined to be a spatially varying and a function of pore diameter and conversion. Although permeability is not explicitly stated as a porous property, it is captured within the property, viscous resistance which is equivalent to the inverse of permeability. Initially, an expression that determines the micropore diameter progression is gathered from Wang et al., shown in expression below, and assigned to its designated variable, $d_{p.}$ It may be noted that the expression is derived from a capillary based model.[24]

$$d_p = \frac{4\varepsilon}{S_v(1-X)} \tag{3.13}$$

Although the porosity can be readily referred to via customization method, the specific volume in the units of m^2/m^3 must be determined. To remain consist with the previous chosen specific volume of 480 m^2/g is converted to the desired units of m^2/m^3 from the use of the carbon density including porous effects. Again, it is reiterated that a decaying factor of 1-X is attached to this specific volume for better realism of the model. Afterwards, a permeability expression derived from cylindrical pore model is gathered and utilized within the loop to calculate the resultant viscous resistance profile.[24,30] The resultant viscous resistance expression can be seen below.

$$viscous\ resistance = \frac{32}{d_p^2} \tag{3.14}$$

In order for the model to remain true to the real char particle undergoing gasification, the model must have a more realistic representation of the main mode of mass transport, diffusion. Diffusion dominates mass transport because the lack of imposed velocity within the entrained gasifier diminishing other modes of transport and the high operating temperatures amplify diffusion. There are two main zones that diffusion needs to be determined for, diffusion that occurs with and without porous effect. Porous effects cannot be neglected as micropores and mesopores essentially impede diffusion by limiting the species mean free path thus containing and prevent species interaction.

Before finalizing the diffusion expression, the type of diffusion model must be selected. There are various types of diffusion models developed but are generally categorized in two forms, multicomponent (species to species) or species to mixture. The latter is chosen as there due to many well-established expressions and species to mixture diffusion is generally easier to develop for UDFs due to lesser amount of combinations. For the diffusion fluid zone, there are plethora of well-established diffusion expressions or values that can selected. To select most representative, the diffusion expression must be dynamic by being able to correctly react to varying factors such as pressure, temperature, and species unlike constant binary diffusion coefficients which are derived from a set operating parameters and lack versatility in an evolving domain. The selected diffusion model that satisfy the criteria is from a modified diffusion expression by Fuller et al which is an expansion on the diffusion expression from Chapman and Enskog.[48] The model below

assumes that that the gas acts as an ideal gas and that correction factor is assumed to be unity. The ideal gas assumption is valid in this CFD model as the operating temperature is relatively high (above 1600K). In addition, the atomic parameters in the dominator are determined from regression analysis of experimental data with an absolute error of approximately 4%.[48] Implemented atomic parameters are displayed below.

$$D_{i,m} = \frac{(1.0 * 10^{-7})T^{1.75}}{P_{tol,atm}\sqrt{\frac{MW_i + MW_{avg}}{MW_i MW_{avg}}}\left(v_i^{\frac{1}{3}} + v_{avg}^{\frac{1}{3}}\right)^2} \quad (3.15)$$

Table 3.8 Atomic Diffusion Volume

Species	Atomic Diffusion Volume (-)
H_2	7.07
H_2O	12.7
CO_2	26.9
CO	18.9

To address the particle zone, it is essential that the porous effects include the desired properties as sought for in the fluid diffusion zone. The chosen expression to capture porous diffusion is Knudsen diffusion. Knudsen diffusion is developed from a capillary model that assumes the system or in this case, the micropores and mesopores, are significantly smaller or approximately equal than the corresponding species mean free path. From this explanation, it is natural that many other char gasification models implement Knudsen diffusion as pore diameter can be on the nanometer scale which is significantly smaller than typical mean free path. Knudsen diffusion also assumes only gaseous species are interacting with micropores and colliding with pore's circumference preventing and/or

slowing down the diffusion rate of the specific species to the mixture. From this explanation, it is evident that Knudsen diffusion is not only a function of dynamic variables, primarily temperature, but also micropore diameter. The following is the expression for Knudsen diffusion of the ith species into the gaseous mixture is shown below.

$$D_{i,m,knud} = \frac{d_p}{3}\sqrt{\frac{8R_uT}{\pi MW_i}} \tag{3.16}$$

Knudsen diffusion by itself is still not suitable to represent total effective diffusivity as molecular diffusion, developed in the fluid zone, can occur simultaneously with Knudsen diffusion. Also, it is important to include both expression as during the char's natural progression causes it to decay, Knudsen diffusion becomes less prevalent as pore diameters begins to grow which fuels molecular diffusion to become more dominant. The common combination of the two expressions for total effective diffusivity can be seen below where it is evident as Knudsen diffusion increases and becomes unstable due to pore growth, Knudsen diffusion begins to phase out and molecular diffusion becomes more dominant. In this expression, it is assumed that tortuosity is equivalent to the inverse of porosity.

$$\frac{1}{D_{i,m,eff}} = \frac{\varepsilon}{\tau}\left(\frac{1}{D_{i,m,knud}} + \frac{1}{D_{i,m}}\right) \tag{3.17}$$

3.3.3.5 Species Properties – Kinetic Theory

To ensure a realistic model as high temperatures and pressures, the species physical and thermal properties must be determined with accuracy. Each species' viscosity and thermal conductivity were altered from the default constant values to being determined from kinetic theory. Kinetic theory enables the viscosity to change with temperature, which translates into thermal conductivity expression evident by the viscosity term in Eq. 3.19, which overall, improves model accuracy. This is illustrated in the kinetic theory expressions for viscosity and thermal conductivity respectively from the Fluent User's Manual.[7] It can be seen that viscosity depends on the Lennard-Jones parameters that are based on a molecular scale estimation derived from intermolecular potential functions.[53] Since viscosity now is derived within the intermolecular framework, the estimated viscosity value should theoretically be more accurate. All Lennard-Jones parameters are obtained from ANSYS's species database.

$$\mu = 2.67 * 10^{-6} \frac{\sqrt{MW_i * T}}{\sigma^2 \Omega_{\mu}(\frac{T}{\varepsilon_{L-J}/k_B})} \tag{3.18}$$

$$k = \frac{15}{4} \frac{R_u}{MW_i} \mu \left[\frac{4}{15} \frac{c_p MW_i}{R_u} + \frac{1}{3} \right]] \tag{3.19}$$

3.3.3.6 Governing Equations

Before any simulations are conducted, it is crucial to understand the governing equations that are solved during the simulations: the momentum, mass, species, and energy conservation equations. Typical conservation equations are solved for purely fluid zones

which are the fluid in the surrounding environment end within the resolved voids of the particle. In this model, these governing equation are solved in the regions where solely the fluid occupies which is the volume surrounding the particle. In addition to these conservation equations, modified versions of these equations are required to account for the porous effects and to be solved in the porous region. The governing equations for the porous regions are the modified single-phase porous media momentum, mass, and energy conservation equations. The mass, momentum, and energy equations are displayed below and gathered from Fluent's User Manual and Theory Guide.[6,7] The first set of equations consist of the mass, momentum, species and energy standard conservation equations respectively.

The expression below is the mass conversation equation where ρ is the density, and ν is the velocity.

$$\frac{\partial(\rho)}{\partial t} + \nabla * (\rho \vec{v}) = 0 \tag{3.20}$$

The expression below is the momentum conversation equation where p is the pressure, g is gravity, and F is external body forces (e.g. interactions with dispersed phases) or model-dependent sources (e.g. porous media).

$$\frac{\partial(\rho \vec{v})}{\partial t} + \nabla * (\rho \vec{v} \vec{v}) = -\nabla p + \nabla * (\bar{\bar{\tau}}) + \rho \vec{g} + \vec{F} \tag{3.21}$$

The expression below is the species conservation equation where Y_i is the mass fraction of the ith species, J_i is the diffusional flux of the ith species, and R_i is the net rate of production via reactions of the ith species.

$$\frac{\partial(\rho Y_i)}{\partial t} + \nabla * (\rho \vec{v} Y_i) = -\nabla \vec{J_i} + R_i \tag{3.22}$$

The expression below is the energy conservation equation where ρ_f is the fluid density, E_f is energy in the fluid zone, S_f^h is the fluid enthalpy source, k_f is the thermal conductivity of the fluid zone, h is the enthalpy, and τ_{eff} is the effective stress tensor.

$$\frac{\partial}{\partial t}(\rho_f E_f) + \nabla * (\vec{v}(\rho_f E_f + p) = S_f^h \nabla * [(k_f)\nabla T - (\sum_i h_i J_i) + (\bar{\bar{\tau}}_{eff} * \vec{v})] \tag{3.23}$$

The next set of equations are the governing mass, momentum, species and energy conservation equations in the porous region respectively.

The expression below is the mass conservation equation in the unresolved porous region where ε is the unresolved porosity.

$$\frac{\partial(\varepsilon\rho)}{\partial t} + \nabla * (\varepsilon\rho\vec{v}) = 0 \tag{3.24}$$

The expression below is the momentum conservation equation in the unresolved porous region where B_f are body forces, μ is dynamic viscosity, K is viscous resistance, and C_2 is inertial resistance.

$$\frac{\partial(\varepsilon\rho\vec{v})}{\partial t} + \nabla * (\varepsilon\rho\vec{v}\vec{v}) = -\varepsilon\nabla p + \nabla * (\varepsilon\vec{\tau}) + \varepsilon\vec{B_f} - (\frac{\varepsilon^2\mu}{K}\vec{v} + \frac{\varepsilon^3 C_2}{2}\rho|\vec{v}|\vec{v}) \quad (3.25)$$

The expression below is the species conservation equation in the unresolved porous region.

$$\frac{\partial(\rho\varepsilon Y_i)}{\partial t} + \nabla * (\rho\varepsilon\vec{v}Y_i) = -\nabla\vec{J_\iota} + R_i \quad (3.26)$$

The expression below is the energy conservation equation in the unresolved porous region where ρ_s is the solid density, E_s is the energy in the solid region, and k_s is the solid thermal conductivity,

$$\frac{\partial}{\partial t}\left(\varepsilon\rho_f E_f + (1-\varepsilon)\rho_s E_s\right) + \nabla * (\vec{v}\left(\rho_f E_f + p\right) = S_f^h + \nabla * [\left(\varepsilon k_f + (1-\varepsilon)k_s\right)\nabla T - (\sum_i h_i J_i) + (\bar{\bar{\tau}} * \vec{v}) \quad (3.27)$$

From a quick comparison between the two conservation sets of equations, it is evident that porous effect is highly influential in the governing equations and must be accurately determined in order to avoid significant inaccuracies. This is emphasized by simply the fact that porosity is including in all temporal terms and one way or another, including in many other terms as well.

3.3.3.7 Residuals

To further the understanding of Fluent, it is essential that the convergence criterion is well understood. The main convergence criterion within Fluent is defined as a residual.

A residual is defined as the summation of individual cells' imbalance of a variable between the specific cell and the neighboring cells including a constant source term.[7] This is better illustrated in expression below where R_Φ is the residual of a variable, Φ is any variable, b is a source constant, a_{nb} is the neighboring cell coefficient, and a_{cell} is the cell coefficient.

$$R^{\phi} = \sum_{Cell} \left| \sum_{nb} a_{nb}\phi_{s,nb} + b - a_{cell}\phi_{s,cell} \right| \tag{3.28}$$

In order to quantify if the summation of variable imbalance or residual is indicating convergence, the residual value will decay as the iterations continue until a residual criterion has been met. If this is the perceived trend, Fluent is indicating that the variable's residual is converging to a value as the variable's imbalance is continually minimized. If the opposite is occurring and residual amount continually increase, Fluent is indicating that the variable is diverging and there is an underlying problem with the simulation set-up, the model, or both. Another possible trend is where the residual "levels out" and the residual value remain constant as the iteration continues. This indicates that the variable can't converge any further and has reached its "optimal" value.

3.3.4 2-D CFD Model Development – Fluent Set-Up

All components required for the CFD model have been described, leaving the CFD model yet to be developed. Please note that the two-dimensional CFD model was also first initially developed as a foundation for the three-dimensional CFD model. From the describe CFD development procedure, the two-dimensional CFD model is first thoroughly

described and then the three-dimensional CFD model is described, with any notable discrepancies compared to the two-dimensional model.

Fluent offers many well-defined and highly customizable submodels that can be selected to fit the needs of the model under development. Out of the many combinations of submodels, the viscous [flow], energy, and species (includes species transport and reaction) submodels are enabled. The viscous model is chosen to be laminar due to the particle being entrained in the flow, thus a minimal amount of relative velocity is present and the flow is laminar. Since the viscous model is always enabled, the Naiver Stokes and other conservation of momentum equation, are always present. In addition, once the species submodel is selected, the energy submodel is automatically enabled due to the dependence of the species on energy submodels, which also enables the conservation of energy equations. No further actions or specifications are needed for the energy submodel at this time. Species transport is required as it captures the transport of the chemical species from solving species conversation equation and enables the conservation of species equations. Within the species submodel dialog, the option, species transport, is enabled, which further enables the selection both volumetric and wall surface reactions. Since both reaction types are required, both options are selected. Wall surface reactions are used to implement heterogeneous gasification reactions with their associated heat of reactions. An aggressiveness factor, a variable within the range of 0 to 1 that controls the robustness and convergence speed, of 0.5 was used in the explicit chemistry solver. Additional selected species transport options are inlet diffusion (allowing diffusion from inlet boundary condition), thermal diffusion, and diffusion energy source.

Initially, H_2, H_2O, CO_2, CO, and C<s> (carbon solid) are copied from Fluent's fluid species database populated with predefined well-established thermal and physical properties such as standard state enthalpies, standard state entropies, specific heat polynomials, and molecular weights. Each species' thermal conductivity and viscosity were altered from the default constant values to being determined from kinetic theories stated in Section 3.3.3.5. An additional customizable blank solid species material is added and named, "Carbon-solid" whose density, thermal conductivity, and specific heat values are populated with constant values similar to corresponding true values of pure carbon. It may be noted that C<s> is applied to the unresolved porous regions, is a fluid due to Fluent's specification, and is the species that participates in reactions while Carbon-solid is utilized for heat transfer with the solid portion in the unresolved porous regions. All species and their corresponding non-typical physical and thermal properties are displayed in Table 3.9.

Table 3.9 Species Physical and Thermal Properties

Species	State	Thermal Conductivity (w/m/K)	Viscosity (kg/m/s)	Density ($kg/m^{3)}$	Specific Heat (J/kg/K)
H_2	Fluid	Kinetic theory	Kinetic theory	N/A	Polynomial
H_2O	Fluid	Kinetic theory	Kinetic theory	N/A	Polynomial
CO_2	Fluid	Kinetic theory	Kinetic theory	N/A	Polynomial
CO	Fluid	Kinetic theory	Kinetic theory	N/A	Polynomial
C<s>	Fluid	Kinetic theory	Kinetic theory	N/A	Polynomial
Carbon-Solid	Solid	1.891	N/A	2100	1458

In order for Fluent to characterize the species within the computational domain and their interactions, the species must be analyzed together in what is referred to as a mixture material. A mixture material is a material composed of multiple species whose physical

and thermal properties are determined from the presence of each species and used to define the reactions that occur from species interaction. In the initial development of the mixture material, the fluid species, excluding C<s>, are specifically specified in the category, "Selected Species" in the following order from first to last, H_2, H_2O, CO_2, and CO. Note that the last species, CO, is the "bulk species," thus its mass and mole fractions are calculated as the remaining mass or mole fraction after summation of the non-bulk species. CO is selected as the bulk species because CO typically has the greatest concentration within an entrained gasifier as indicated by Botero, which translates into the greatest mole and mass fraction.[14] Since CO is the most abundant species, it is necessary and good practice to assign this species as the bulk to aid in simulation stability.[7] Placement of each species must also be noted as species ID of 0 is attached to the first species and so on and so forth. This information is required in UDF customization methods, which are discussed later in detail, as species are identified by their species ID. Lastly, C<s> is specified under the category "Selected Site Species" in order to enable heterogeneous reactions for the mixture while not including carbon in the gas-phase mixture.

The next major step is to specify the reactions that occur from the interactions of the species and their corresponding properties within the mixture material dialog. The previously stated reactions are implemented to characterize gasification and water-shift reactions. Homogeneous and heterogeneous reaction rates are differentiated by their reaction type, as homogeneous are defined as volumetric reactions and heterogeneous defined as wall reactions. Within the mixture reaction dialog, the necessary inputted reaction parameters are pre-exponential factor (A), activation energy (E_a), and temperature exponent (n_T) for the modified Arrhenius' equation shown below.

$$k_r(T) = AT^n e^{-\frac{E_a}{R_u T}} \tag{3.29}$$

Although all four reactions have their corresponding stoichiometric chemical reactions defined within this dialog, the only true reaction kinetics inputs are for those of the water-shift gas reactions, reactions one and two, and gasification reaction rate parameters are populated with dummy filler parameters. The gasification kinetics are not required, as the dialog heterogeneous reaction rates will be overwritten from a corresponding customization method, which includes the effects of a dynamic and spatially varying porosity on the available surface area and is obtained from an expression other than the provided modified Arrhenius framework. The previously stated water-gas shift kinetics on Table 3.6 was implemented.

Two mechanisms, named “homogenous” and “heterogeneous”, are developed for the sole purpose to specify and restrict where the reactions may occur. The mechanism, “homogeneous” contains both directions of the water-gas shift reaction. The mechanism, “heterogeneous” contains both gasification reactions and requires a specification on the coverage of the site species in the mechanism specified domain. Since there is only a single site species, C<s>, the site coverage in the porous domain is designated to be completely covered by C<s>. It may be also noted by default that the reaction diffusion balance is enabled once species transport model is selected, but must be disabled within this model, as it causes erratic and undesired behavior.

In sequential order, the formulation of each mixture property must be determined and specified. Most of the mixture properties are formulated from a weighted average of

individual species properties, with the exception of mass diffusion, explained in Section 3.3.3.4. However, the species contribution can be calculated from either a molar or a mass basis. In this specific case, a molar based calculation is favored due to high temperatures resulting in the gas to behave more as an ideal gas. This also explains why ideal gas options are chosen in Table 3.10. Kinetic theory is chosen as the formulation method of thermal diffusion to give the thermal diffusion coefficient a dynamic representation. Table 3.10 below indicates how each mixture property is determined.

Table 3.10 Chosen Formulation Expression of Mixture Properties

Property	Formulation
Density	Ideal Gas Law
Specific Heat (J/kg-K)	Mixing-Law
Thermal Conductivity (W/m-K)	Ideal-Gas Mixing Law
Viscosity (kg/m-s)	Ideal-Gas Mixing Law
Thermal Diffusion Coefficient (kg/m-s)	Kinetic Theory

Next, the mesh interface, named “fluid-to-particle” is created from the pair of interfaces that were previously made during the meshing phase. The development of the mesh interface can create some combination of boundary conditions even undesired boundary conditions, but in this case created two wall and one interior boundary condition.[7] The wall boundary conditions initially posed a problem due to their required boundary of either gradients or values of simulation factors (e.g. temperature and species) that will be imposed at their respective locations. However, since the interfaces are perfectly in contact, no mesh elements are assigned to either wall boundary conditions rendering the conditions useless as they no longer participate in the calculations. It may be noted upon opening a developed Fluent file, the details of the mesh interface may vary, revert to previous settings, or be deleted. As a precautionary measure, each time the Fluent file is reopened, settings

of the mesh interface are carefully checked and verified to ensure that the mesh interface has not been changed from its desired settings.

The next major section that must be developed is the fluid and particle domains found under the section “Cell Zone Conditions”. Initially, the domains are both checked if they are defined as fluid, and if not, the domains are redefined as fluids. Within the fluid cell zone dialog, the reaction option is enabled and the mechanism specified is “homogeneous”. This ultimately specifies that reactions are to occur within this zone and only the water-gas shift reactions are permitted. Lastly, the material of the fluid zone is specified to be the mixture that was previously developed. Next, the particle domain must be addressed and altered to fit the purposed CFD model.

The three main enabled characteristics of the particle domain are “Source Terms”, “Reactions”, and “Porous Zones”. In the reaction tab, the reaction mechanism, “heterogeneous”, is assigned to the particle domain and as a byproduct of defining the region as porous, the field, “Surface-to-Volume Ratio (1/m)” is available. This field is left as a value of one, as this physical property and its transient behavior is accounted for in the customization and any other value would amplify the user-defined reaction rates. The “Source” dialog is initially left unpopulated as the corresponding user-defined function, at this point, has not been compiled for use. Here in the “Porous Zone” setting, the particle is defined to be pure carbon using the previously created solid material, “Carbon-solid” in the category, “Heat Transfer Settings”. Similar to the “Source” dialog, the remaining settings, viscous resistance and porosity, have not been compiled at this point, thus these settings are not yet defined. As a consequence of defining a porous zone, the option of how to calculate porous zone velocity can be defined. To remain conservative and to keep the

highest accuracy by solving the physical velocity flow field, the physical velocity formulation was preferred.[7] Lastly, within the "Cell Zone Conditions", the operating pressure is changed to that of a typical operating pressure within an entrained gasifier. This resulted in the defaulted operating pressure of 101,325 Pa (atmospheric pressure) be changed to stated 2,000,000 Pa.

The next priority to be addressed is the boundary conditions. Upon the initial development of the boundary conditions, it is necessary to ensure that the boundary conditions assigned during meshing are correct. Typically, Fluent can determine the type of the boundary condition from the provided label. If this was not the case, the boundary condition is easily changed to the desired boundary condition. In the two-dimensional model, it is important that the flat face is defined as an axis type as it permits axisymmetry. For a better visual representation, the current hemispherical model is mirrored from the defined axis within the graphics option to result in a circular domain. Afterwards the surrounding circumference, previously labeled "Pressure_outlet" is ensured to be of type pressure outlet. It is noted that pressure outlet is commonly implement as an outlet at a specified gauge pressure but has the ability to "reverse flow" such that flow can enter the CFD domain through this boundary condition. This ability is exploited as it can automatically replenish the CFD domain with species at a specified temperature while imposing no additional velocity, if gauge pressure is populated with a zero value, leaving the domain's velocity to be determined from the occurring reactions. The species from the pressure outlet boundary condition are specified in mole fractions at a specific temperature to reflect the ambient environment surrounding of the particle within the gasifier previously

determined. Table 3.11 is specifications to reflect the ambient environment and is assigned to the pressure outlet boundary condition.

Table 3.11 Pressure Outlet Boundary Condition Specifications

Specification	Value
Gauge Pressure (Pa)	0
Backflow Total Temperature (K)	1800
H_2 Molar Fraction (-)	0.28
H_2O Molar Fraction (-)	0.21
CO_2 Molar Fraction (-)	0.12

After many attempts and iterative refinement, the solution methods were finalized. Overall the "Coupled" solver scheme was chosen which indicates the implementation of a pressure-based coupled algorithm. Advantages of the pressure-based coupled algorithm is its ability to compensate for poor quality meshes or implementation of relative large time steps.[6] These advantages are emphasized in the application of the three-dimensional model as the resolved particle may have some abstract complex geometry that may naturally result in mesh regions being developed. Lastly, the Coupled solver's limitations, primarily incompatibility with fix velocity (assigning a constant velocity for interior cell zone) and non-iterative time advancement solver, do not restrict nor affect the CFD models.[6]

Spatial discretization of the gradients, pressure, density, momentum, and the species are individually assigned formulation in their respective field in the dialog, "Solution Methods". The gradient is chosen to be discretize from the "Least Squares Cell Based" method as it provides a less computational expensive method to calculate derivatives for complex meshes or in this case, the resolved three-dimensional model.[6] The gradients of pressure, density, momentum, and species are individually discretized by

Second-Order Upwind formulation which is sufficient to discretize the variables while being less computational intensive compared to other methods such as the Third-Order Upwind formulations. After examination of the computational time of all transient formulations, the first order formulation was selected to be less computational expensive while resulting in small variation compared to more accurate formulations (e.g. second order implicit).

Although all of the necessary definitions of solvers, boundary conditions, and zones have been developed, the CFD model may be too "stiff" for the model to correctly converge with fair stability (indicated by the lack of residual banding) without further adjustment. The adjustments that can be made to achieve a functional simulation are adjustments of the under-relaxation factors from their default values. Under-relaxation factors control how the variables are updated from iteration to iteration. Typical range of values are from 0 to 1 where 0 is the most conservative case where the updated iterative value is complete biased towards the previous iteration. On the other side of the spectrum, a value of 1 updated iterative value is complete bias on the newest calculation. Beyond this range, the under-relaxation factors can be assigned values greater than one, which takes an aggressive approach by updating the iterative value from extrapolation of the current iteration value and newly calculated iteration value. It is difficult to optimize these factors, as there is a vast amount of combinations that can be implemented. To narrow the variability, only the species (individual species are lumped together) and energy equations were chosen to be varied, as these under-relaxation factors are prone to be affect the calculations significantly while the remaining factors are left at their defaulted value. The final under-relaxation factor set is achieved from executing multiple simulations. Each simulation varied the

species and energy under-relaxation factors and started from a low initial factor and increased as the simulation progressed until divergence or failure. Criteria for determining the final factors is evaluating the stability: whether the simulation diverged or not and if residual banding occurred (indicating instability) and choosing one of the highest values for both species and energy factors. Table 3.12 is the final set of under-relaxation factors. Please note the field "User Defined Scalar" is discussed in the Section 3.4.

Table 3.12 Under-Relaxation Factors

Variable	Under-Relaxation Factor
Density	1
Body Forces	1
Species (Lumped)	0.6
Energy	0.6
User Defined Scalar	1

The majority of the simulation has been described, but a stopping criteria is required to evaluate when the solution has achieved sufficient accuracy and can progress to the next time step. There are many types of stopping criterion but after extensive comparison and experimentation, an absolute stopping criterion is selected based on individual variable error, or residual. The final stopping criteria is that the continuity, velocity, energy, all species, and the user-defined scalar must simultaneously be below a residual value of $1 * 10^{-3}$ and energy must exceed or reach the residual value of $1 * 10^{-6}$. The energy residual is specified at a comparatively lower residual value due to the coupled effects between temperature and other variables such as porosity, reaction rates, and species. It may be noted during both models' simulation, the variables, continuity and temperature, were reluctant to satisfy their respective residual criterion. This is problematic as in some situations; the residuals will never reach the specified values, preventing simulation

advancement. To prevent this, an additional stopping criterion is required. To prevent the simulation from stalling, an iteration limit is applied to every time step such that if the time step has not yet reached the specified residual criterion within the iteration threshold, the simulation proceeds to the next time step. This iteration threshold is difficult to definitively define due to its high variability with time step as a bigger time step will require a higher iteration threshold to accurately simulate the data if the residual criterion is not met. A time step of 0.0005 s or 0.5 ms with the previously residual criterion and an iteration threshold of 200 iterations per time step was determined to be a suitable stopping criteria that results in high accuracy. The implementation of 0.5 ms time step is justified as a simple experiment, similar to the mesh convergence technique, was conducted where multiple varying time steps that are multiples of 0.5ms are individually applied to the simulation. Based off the resultant volume averaged conversion and porosity, the relative error was calculated assuming the smallest time step is the true value.

In order to begin a simulation, a set of initial conditions must be provided. In this case, the initial conditions are the same values specified in the far field (pressure outlet) boundary conditions, in order to initially impose ambient conditions. It may be noted that the initialization only recognizes species mass fraction, so mass fractions were populated for each species rather than mole fractions. In addition, an initial value for the user-defined scalar, which represents the porosity, must be populated. From analysis of the pyrolysis parameters and heating conditions to the work accomplished by Zygourakis, a reasonable initial porosity was chosen. Table 3.13 shows the initial conditions.

Table 3.13 Initial Conditions

Variable	Value
Gauge Pressure (Pa)	0
Axial Velocity (m/s)	0
Radial Velocity (m/s)	0
H_2 Mass Fraction (-)	0.0274638
H_2O Mass Fraction (-)	0.1840716
CO_2 Mass Fraction (-)	0.256955
Temperature (K)	1800
User Scalar – Porosity (-)	0.68

After the initialization, further action must be taken in order to increase the realism of the model due to initialization impacting entire model domain. This is problematic as the initial initialization, if not altered, would introduce reactants throughout the entire particle, fueling gasification reactions from the first time step and overestimating the reactant's penetration into the particle and the amount of conversion. To prevent this, an action named "patching" is applied, to further specify the absences of CO_2 and H_2O at the initial conditions for the particle zone. The "missing" mass fraction within the particle is then lumped into the bulk species CO, thus finalizing the initialization process.

3.3.5 3-D CFD Model Development – Fluent Set-Up

Similar to the set-up of the two-dimensional model, the three-dimensional model has similar settings, with some variation. In order to import the reconstructed mesh file of the resolved particle, a Fluent analysis system is placed into the ANSYS workbench and instead of initializing the DesignModeler software, the mesh is imported into the ANSYS mesh software in the corresponding analysis system. This action ultimately removes the DesignModeler, leaving the analysis system with only the mesh and Fluent portions. As stated previously, after initialization of Fluent, the entire domain is corrected from the

meter length scale to the millimeter scale. Afterwards, the geometry must be modified such that the volume of the two-dimensional and the three-dimensional model are approximate or equal. To achieve this, a scaling ratio that was developed from diameters of each model, that is discussed later, and which is applied to all coordinates, X, Y, and Z.

The ratio is applied through the scaling option within Fluent, where the ratio is specified for the X, Y, and Z coordinates and then applied. To ensure that the spherical 2-D and non-spherical 3-D particle volumes are approximately the same within Fluent, a monitor is created to calculate the volume of the altered char particle. This valued is verified to be approximately the same as the volume of the 100-micron sphere. Ensuring the total volumes (macropore and unresolved volumes for 3-D model), mass, and size are exactly of each other is important for validating the comparison between the two models as approximate volumes will limits the variation between the two models, primarily the physical features. This is explained in more detailed in the previous section

Similar to the two-dimensional model, the mesh must be checked within Fluent and if the mesh does not pass, or indicates quality issues, the mesh must be altered within Fluent or ScanIP until the issue is resolved. Explained more in depth in the next section, all possible undefined boundary conditions that are not realized in ScanIP will be defaulted to be a “wall”. This is problematic, as the boundary between the particle and fluid domain is defined be a wall along with an additional boundary condition typed shadow wall. The wall boundary condition enforces a value or a gradient value for all variables (e.g. temperature and H_2) at that boundary condition location. The shadow wall is a byproduct of the wall boundary condition if there is a solid or fluid zone on each side of the wall, in this case two fluid zones, “Fluid” and “particle” and requires similar input as the wall. In addition, the

shadow-wall can also prevent any fluid flow passing this boundary condition. To remedy this, the wall boundary condition is redefined as an interior boundary condition which does not enforce any specifications and simply is a “boundary condition” that fluid can occupy. Compared to the two-dimensional model, it is evident that the three-dimensional model does not require any interfaces for mesh interface creation because the boundary condition between the zones can be readily changed to an interior boundary condition.

The remaining settings, such as boundary and initial conditions and solver settings, that were developed in the two-dimensional model are tested and validated for the three-dimensional model. Since there was no indicated outstanding inaccuracies or failures, the same settings shown in Table 3.9 to Table 3.13 were implemented, with one exception: the initial porosity. The initial porosity must be altered since in the three-dimensional geometry, significant geometric features such as macropores have been resolved and are no longer lumped into the unresolved geometry’s porosity. This new porosity was calculated within Fluent and the method is discussed in Section 3.4. For this particular char particle, the recalibrated porosity in the unresolved regions, or also known as the region between the resolved voids, is approximately 0.638.

Unlike the two-dimensional model where a plane is readily available for post-processing contour plots, the three-dimensional model lacks such planes. In the three-dimensional model, three planes (XY, YZ, and ZX planes) are created for the purpose of post-processing. All planes share a common attribute of coinciding at the origin of the model. Although not previously mentioned, the planes are also implemented in solution animations in order to visually track the progression of specified variables for a given post-processing setting.

3.4 CFD Model Customization

Although a majority of the parameters and settings are readily available in Fluent, there are aspects that either require slight adjustment or need to be added in order for a more accurate representation of a char particle and its consumption. An example of a primarily feature that was not available in Fluent, thus requiring user intervention, is the lack of Knudsen diffusivity in the porous region. All of the user-defined features that were implemented in the models are shown in Table 3.14 and in the Appendix.

Table 3.14 User-Defined Features in CFD Models

Variable	User-Defined Feature	UDF Macro
Conversion	Custom-Field Function	N/A
Transient Porosity	User-Defined Scalar (UDS)	N/A
Unsteady UDS	User-Defined Function (UDF)	DEFINE_UDS_UNSTEADY
UDS Source	User-Defined Function (UDF)	DEFINE_SOURCE
Diffusion Coefficient	User-Defined Function (UDF)	DEFINE_DIFFUSIVITY
Viscous Resistance	User-Defined Function (UDF)	DEFINE_PROFILE
Heterogeneous Reaction Rates	User-Defined Function (UDF)	DEFINE_SR_RATE
Porosity	User-Defined Function (UDF)	DEFINE_PROFILE

Some of these features can be readily created within Fluent with minor complications but there are others, which benefit from a third party software using of the coding language, C. It may be also noted, the open source software, Notepad ++ was used to develop the UDFs as Notepad ++ can be specified for the coding language C which reduces confusion regarding syntax errors thus expediting the development process.

The simpler customizations that can be completed within Fluent are the custom-field functions and the user-defined scalars. Out of the two, the simplest method is the custom-field function that can create expressions using a combination of any numerical

value and Fluent automatic calculated variables' cell values with simple mathematical operations such as powers, multiplication, and logarithmic operations. Cell values refers to the variable value at the center of the meshing element. Instead of a more complicated method, a metric of the char particle decay, conversion can be quickly developed within Fluent via custom-field function. Conversion is only a linear function of one variable, porosity and can be quickly developed from the expression below.

$$X = \frac{\varepsilon - \varepsilon_o}{\varepsilon_{fi} - \varepsilon_o} \tag{3.30}$$

Constants in this expression are the final porosity, ε_f value that holds a value of unity which indicates complete void occupation/ particle consumption and the initial porosity, ε_o which varies from particle to particle and also depends on implemented assumptions. Although the expression is simple, calculating the current porosity, ε, is not, due to Fluent's inability of treating porosity as a function of time.

3.4.1 Porosity - UDS

In order to compensate for this, a user-defined scalar (UDS), a method to represent any unviable variable within Fluent, is developed to represent and constantly calculate porosity. In Fluent, the UDS quantity is changed to one and is defined such that it only applies to the cell zone correlating to the particle region. All UDSs are composed three main components, diffusion, transient, and source terms. Before any additional settings are developed, a formulation that can calculate the porosity profile must be determined. Initial challenge that transpired is the lack of transient porosity formulation in the literature. Instead, transient conversion formulation was utilized and is further manipulated to derive

an expression via the relationship displayed in Eq. 3.31. The chosen transient expression for conversion was obtained from Sotirchos and Amundson and is shown below.[58] Please note that the negative sign is counteracted by the negative of the carbon stoichiometric coefficient due to being a reactant coefficient and since the char is assumed to be purely carbon, $W_{c,o}$ is unity.

$$\frac{dX}{dt} = \frac{-MW_c}{W_{c,o}\rho_{c,o}} \sum_{i=1}^{2} v_{C,i}\Re_i \tag{3.31}$$

Also note that the carbon density in the formulation above requires recalibration to account for the volume that is initially occupied by voids from the porous effects. This recalibration of density is derived from a pure carbon density from Table 3.9 for consistency and the initial porosity and is displayed in the expression below.

$$\rho_{c,o} = \rho_{c,t}\,(1 - \varepsilon_o) \tag{3.32}$$

Eq. 3.30 is then derived with respect to time in order to obtain the relationship between conversion and porosity rates.

$$\left(\varepsilon_{fi} - \varepsilon_o\right)\frac{dX}{dt} = \frac{d\varepsilon}{dt} \tag{3.33}$$

Combining Eq. 3.31 and Eq. 3.33 results in a new expression that calculates porosity rate based off the reaction rates, density of carbon, and physical properties of carbon that is displayed below.

$$\frac{d\varepsilon}{dt} = \left(\varepsilon_{fi} - \varepsilon_o\right)\frac{-MW_c}{W_{c,o}\rho_{c,o}}\sum_{i=1}^{2} v_{C,i}\Re_i \tag{3.34}$$

From the expression above, it is evident that the UDS that characterizes porosity will only require an unsteady or transient term shown from the left-hand side and a source term shown on the right-hand side. To completely disable the diffusion of the UDS, the inlet diffusion is disabled (found in the UDS dialog) and the UDS diffusion coefficient is defined as zero. The UDS diffusion coefficient can be defined in the mixture properties in the field, "UDS Diffusivity (kg/m-s)", which is becomes available once a UDS has be defined.

In order to provide the source and the unsteady/transient terms to the UDS, individual user-defined functions, UDFs, must be developed and placed in the correct locations. UDFs are greatly versatile customization methods that are created by pre-defined Fluent macros within the framework and syntax of the programming language, C to enhance Fluent's current and standard features.[6] To be able to use the pre-defined macros, all UDF files require the header file, "udf.h". The pre-defined macros for each UDF are explicitly outlined in Table 3.14.

In the case of the transient/unsteady term, the macro, DEFINE_UDS_UNSTEADY, is a macro specifically designated to define the unsteady term in an UDS. The unsteady term is primarily defined from two arguments provided from the unsteady macro, the implicit part or central coefficient named "*apu" and the explicit part or source term "*su". These two terms are resultant of how Fluent assumes how the transient term was discretized. The source term, "*su" is the volume integral of the previous time step and central coefficient, "*apu" is the volume integral of the current time

step. The ANSYS Customization Manual describes the unsteady expression as the following formula. Please note the expression below has been modified from the original in the ANSYS Customization Manual to exclude the effects of mass which undesired for this specific UDS. Once developed and validating through testing, the unsteady UDF named "unsteady_UDS" built and compiled into Fluent. Afterward, the UDF is populated in field, "Unsteady Function" in the User-Defined Scalar dialog.

$$unsteady = \underbrace{-\frac{\Delta V}{\Delta t}\phi^{n}}_{apu} + \underbrace{\frac{\Delta V}{\Delta t}\phi^{n-1}}_{su} \tag{3.35}$$

3.4.2 Porosity – Source Term (UDS)

The last component required for the porosity UDS formulation is the source term. The macro used to define the source term is "DEFINE_SOURCE". Required inputs of the macro are primarily the source expression, which would be the right hand expression from Eq. 3.34 and the derivative of the expression with respect to source's dependent variable, porosity. It may be noted that the derivative can be populated with a value of zero which would force an explicit solution from the UDF.[6] In the developed UDF code, the ability for the reaction rates using parameters from Table 3.5 and Eq. 3.11 to spatially vary is a result of implementing by what is referred to as Fluent's cell temperature and species values. This simply means when the UDF is calculating, each individual cell's temperature and species value is referred to when called upon in the calculation to determine the UDF's value for that specific cell. Since each cell holds a different value, the resultant UDF will be different for each cell causing a UDS profile. It may be noted that the species mole fraction does not have an assigned macro within UDFs to refer to the simulation value and had to be developed from species mass fractions which do have an assigned macro. The following

expression is expression used to convert the ith species mass fraction to mole fraction. In order to correctly referred species, the species ID must be known and can be determined by the order of the species in the "Selected Species" field. The order is from top to bottom of the list starting at a value of zero.

$$X_i = \frac{Y_i/MW_i}{\sum_1^i Y_i/MW_i} \tag{3.36}$$

After determining each gasification reactant's mole fraction value, Dalton's Law is applied to obtain the reactant's partial pressure by simply multiply the mole fraction by the total pressure (approximately 2 MPa).

During the development of the source UDF, the derivative was defined as zero forcing the explicit solution of the source term. After testing and ensuring the UDF has no bugs or undesired properties, the source UDF named "source_UDS" is built and compiled into Fluent. In order to apply the source UDF, the user scalar source amount is specified as one in the particle cell zone dialog in the tab labeled "Source Terms". This unlocks a field where the source UDF can be populated. This action is only applied to the particle cell domain as the porosity calculation is only applicable to the particle zone.

Despite the new dynamic porosity being developed and characterized in the user-defined scalar, translating the resultant UDS profile into the porosity field within the particle domain has yet to be addressed. To address this issue, the macro, "DEFINE_PROFILE" is utilized and developed on within the UDF named "porosity_linked". This macro is a commonly used macro as it can be used to define various boundary conditions (e.g. inlet velocity and species profile) or in this specific simulation

cell zone conditions, primarily porosity, as a function of time and/or spatially coordinates.[6] Within this macro, a loop that entails all cells, is created such that the result of the porosity UDS is copied to the output of the macro. After testing, the UDF is built and compiled into Fluent. The UDF is then populated in the porosity field located within the particle cell zone under the tab, "Porous Zone" completing the translation of the dynamic nature of the variable, porosity.

3.4.3 Gasification Reaction Rates

The finalized reaction rate expressions are also implemented to govern the heterogeneous gasification reaction rates. To accomplish this, a UDF named, "reaction_rate_Tremel" is developed using the macro, "DEFINE_SR_RATE". This macro overwrites the default reaction rate calculated from the inputted reaction rate parameters in the Fluent mixture reaction GUI with defined custom reaction rate. The Tremel expressions are individually assigned to their corresponding reaction within Fluent based off the assigned reaction name. In this case, the CO_2 expression is assigned to the reaction, "reaction-3" and the H_2O expression is assigned to the reaction, "reaction-4". Before implementation, the Tremel expressions must be further modified the resultant units from 1/s to kmol/m^3-s to satisfy the output unit criteria of DEFINE_SR_RATE macro. Knowing that the Tremel reaction rates are derived from the amount of mass change and conversion attributed from individual gasification reaction, the relationship between reaction rate and conversion demonstrated from Eq. 3.31 was utilized. From Eq. 3.31, individual reaction rates can be solved by setting the left-hand side as the corresponding Tremel expression while assuming that there is only one reaction that is the sole contributor to conversion. This leaves the conversion expression with one unknown, the reaction rate and is solved

algebraically resulting in a new reaction rate expression with the required units of kmol/m^3-s. The modified Tremel reaction rate expressions for the UDF can be seen below.

$$\Re_i = \frac{-AS_g P_i^n e^{-\frac{E_a}{R_u T}} W_{c,o} \rho_c}{MW_c \upsilon_{C,i}} \tag{3.37}$$

After validation and testing of the UDF operations, the UDF is built and compiled into Fluent. The reaction rate UDF is hooked into the field, "Surface Reaction Rate" located in the dialog of User-Defined Function Hooks. It is reiterated that the surface-to-volume ratio found in the reaction dialog of the particle domain is set to unity to prevent UDF reaction rates to altered by a factor of the defined surface-to-volume ratio.

3.4.4 Particle Porous Transport - Viscous Resistance

The UDF named, "permeability" is defined using the DEFINFE_PROFILE macro with Eq. 13. Similarly, to the "porosity_link" UDF, the "permeability" UDF implements a cell loop to determine the UDF values for all cells. After testing and validating the UDF, the UDF is built and compiled into the Fluent file. The UDF is hooked into the field, "Viscous Resistance" found under the cell zone "Particle" in the "Porous Zone" tab. Please note there are as many viscous resistance field as coordinates so in the case of the two-dimensional case, there are two fields and for the three-dimensional case, there are three fields. All possible fields are populated with the same viscous resistance UDF.

3.4.5 Particle Porous Transport - Diffusion

Since the expressions (Eq. 3.15 to Eq 3.18) and Table 3.8 stated in Section 3.3.3.4 cannot be applied via Fluent framework, an UDF is required to apply these expressions within the CFD models. Within Fluent, there is no explicit method to differentiate diffusion from zone to zone while including a more complex model so a UDF is required. The UDF named "diffusivity_knud" created and the chosen macro to govern the development of diffusion is "DEFINE_DIFFUSIVITY". Unlike the implemented method to differentiate gasification reactions used in the UDF, "reaction_rate_Tremel", the diffusion zones are differentiated from the possible functionalities of a UDF. Within the UDF, the particle and fluid zone ID are gathered from within Fluent and defined within the UDF. The zone ID then permits the UDF to correctly identify the zones or in UDF terminology, threads and assign variables to these threads. However, the zone IDs are simulation dependent meaning the three-dimensional and two-dimensional simulations will most likely have different ID values for the particle and fluid zones. The identification variables in tandem with if statements allow the UDF to correctly separate diffusion expressions. Within the separated zones, additional if statements are created to separate the species diffusion based off their species ID. Essentially once the simulation domain has been separated by zone and species, the remaining task is to select and develop expressions that can most accurately represent diffusion.

After initial testing and validation through simple custom-field functions to ensure that the calculation is of the correct magnitude (10^{-5} for fluid zone and 10^{-6} for particle zone) and assigned to the corrected zones, the UDF, "diffusivity_knud" is built and compiled into Fluent. The UDF is hooked into Fluent within the mixture properties and

under the field “Mass Diffusivity”, the open user-defined is selected. Upon selection, a dialog box is presented where the compiled UDF can be selected. It may be noted that the diffusion coefficients can be accessed in post-processing under the species tab as laminar diffusion of ith species.

Chapter 4. Results and Discussion

This chapter presents the findings that were obtained from the unresolved two-dimensional model that fully implements the porous continuum assumption and three-dimensional model that only implements the assumption in unresolved regions. The data is initially presented via multiple contour profiles at a given time. In addition, the data is also presented as one-dimensional radial profiles for a given set of incremental times. The latter includes the effectiveness factors that acts as the primarily mode of comparison between the two models.

4.1 Contour Plots

To better grasp the difference between the two models, contour plots of a chosen cross sectional area at specific times are presented and analyzed in this section. Contours plots, unlike other representations, are better suited to demonstrate the models' different profiles throughout the whole cross sectional area while allowing for difference between the profiles to be emphasized. In the three-dimensional case, the cross section was chosen to best highlight the presence and the effects of the resolved geometric features. For both models' circular cross sectional area, the particle region is located in the center and there are cases where the particle cannot be differentiated due to variable profiles within and surrounding the particle. It may be noted that all figures can potentially display regions with low picture quality (e.g. pressure outlet boundary condition and particle to fluid contact region) due to a courser mesh at the corresponding region.

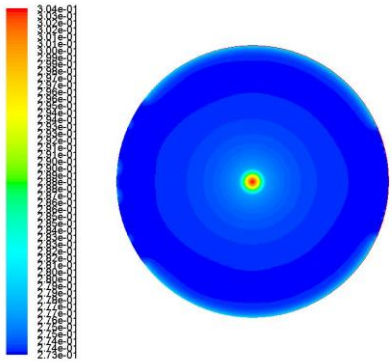

(a) 0.100s – Max: 0.304/ Min:0.273

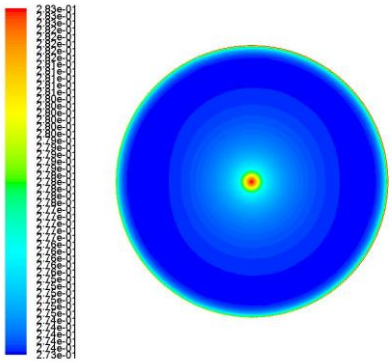

(b) 0.200s – Max: 0.283/ Min:0.273

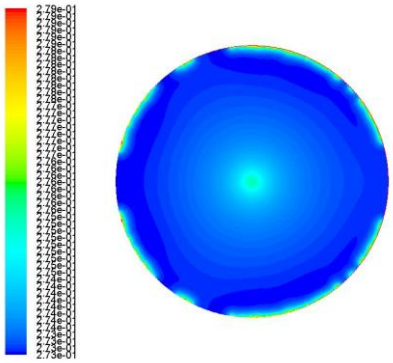

(c) 0.300s – Max: 0.279/ Min:0.273

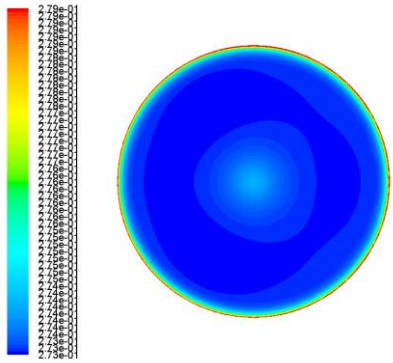

(d) 0.400s – Max: 0.279/ Min:0.273

Figure 4-1. Unresolved Contour Plot of H_2 Mole Fraction

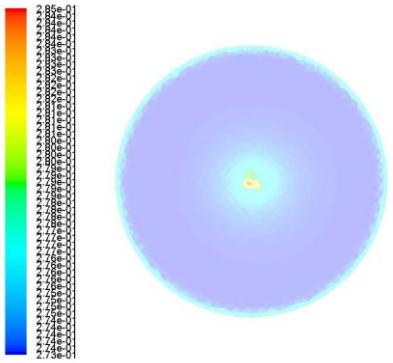

(a) 0.100s – Max: 0.285/ Min:0.273

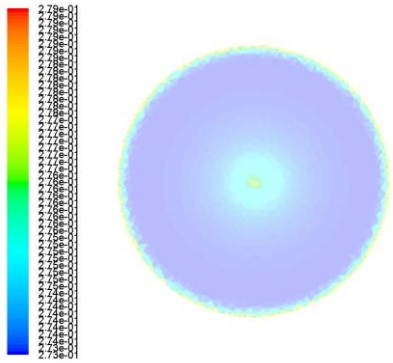

(b) 0.200s – Max: 0.279/ Min:0.273

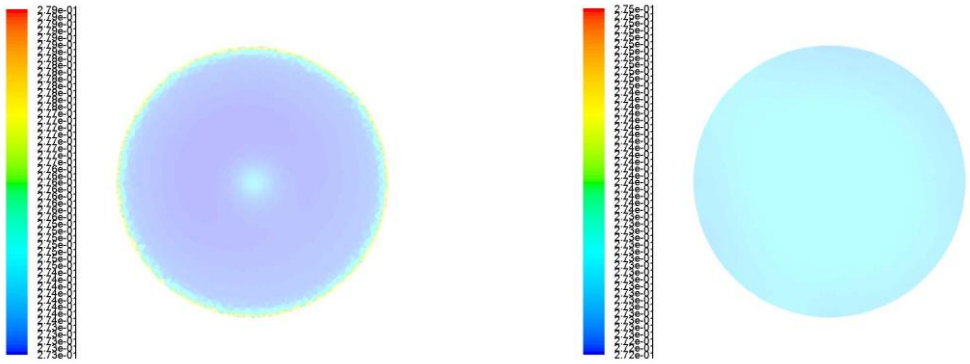

(c) 0.300s – Max: 0.279/ Min:0.273 (d) 0.400s – Max: 0.275/ Min:0.272

Figure 4-2. Resolved Contour Plot of H_2 Mole Fraction

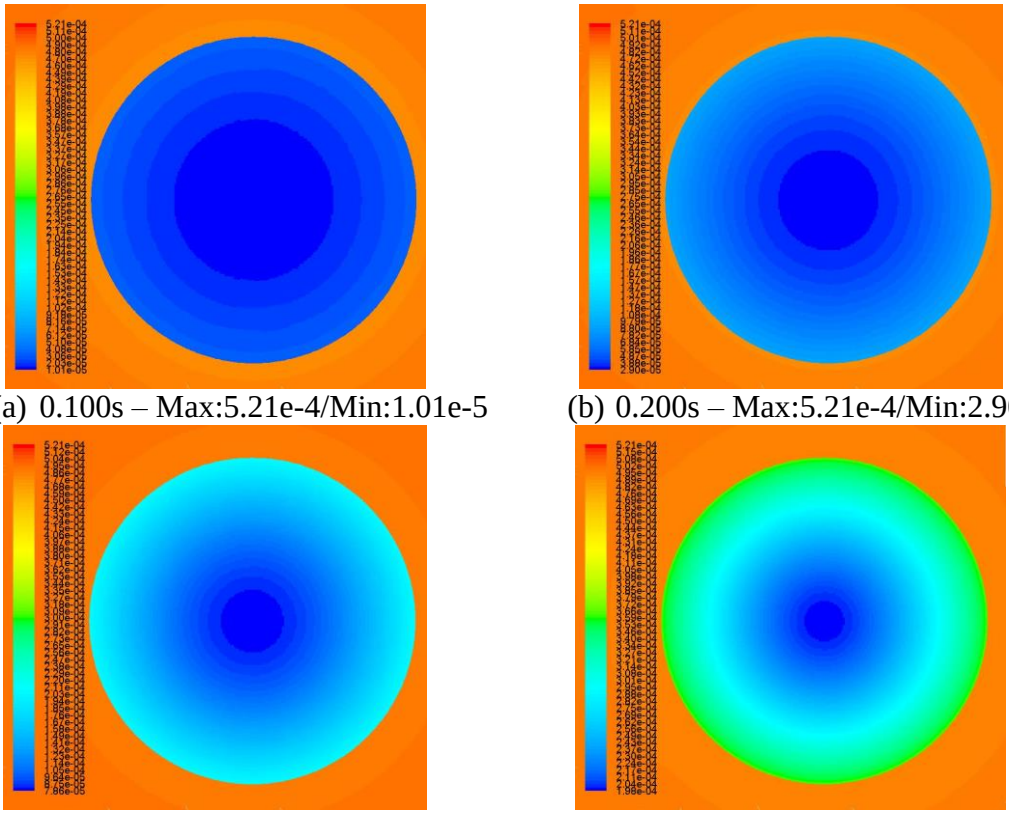

(a) 0.100s – Max:5.21e-4/Min:1.01e-5 (b) 0.200s – Max:5.21e-4/Min:2.90e-5

(c) 0.300s – Max:5.21e-4/Min:7.86e-5 (d) 0.400s – Max:5.21e-4/Min:1.98e-4

Figure 4-3. Unresolved Contour Plot of H_2 to Mixture Diffusion Coefficient (m^2/s)

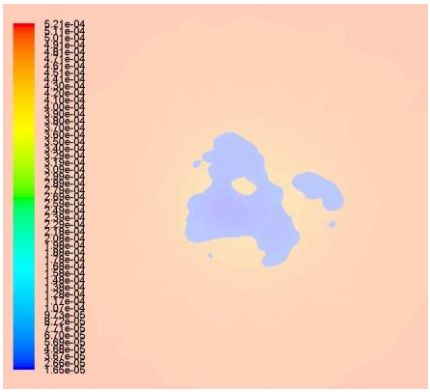

(a) 0.100s – Max:5.21e-4/Min:1.65e-5

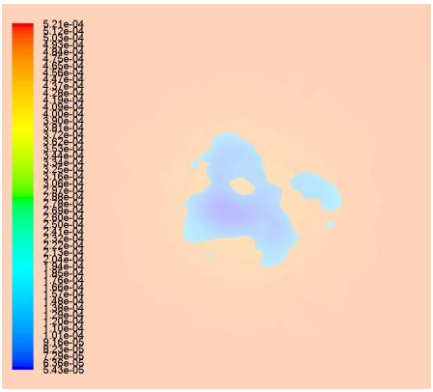

(b) 0.200s–Max: 5.21e-4/ Min:5.43e-5

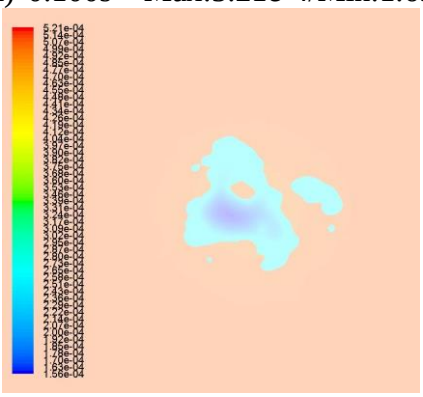

(c) 0.300s – Max:5.21e-4/Min:1.56e-4

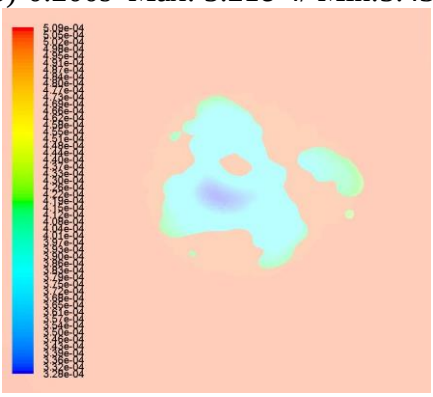

(d) 0.400s–Max: 5.09e-4/ Min:3.28e-4

Figure 4-4. Resolved Contour Plot of H_2 to Mixture Diffusion Coefficient (m^2/s)

The first set of contour plots covers the mole fraction and the diffusional coefficient of the species, H_2 shown above. From the contour plots at times, 0.300s and 0.400s, both the resolved (Figure 4-2c/d) and unresolved particles (Figure 4-1c/d) have ceased production of H_2 evident from the consistent mole fraction range between the two times. Although this is true, the resolved model indicates that it has reached this equilibrium state at a faster rate when compared to the unresolved model shown from the resolved species profile's maximum and minimum remain constant starting from time, 0.200s (Figure 4-2b). Nevertheless, both species profiles are qualitatively similar at times 0.300s and 0.400s. To reinforce the claim made, the resolved model reaches a constant mole fraction profile

faster as the resolved minimums H_2 to mixture diffusion coefficients are significantly greater than those of the unresolved model allowing for the produced H_2 to easily escape the particle to the environment. It may be noted that difference in minimum diffusion coefficients only increases as time progresses.

The minimal value is only of interest regarding the contour range as the maximum value always remains constant value due to the maximum diffusion occurring in the surrounding fluid, which has reached equilibrium during the initial time frame (less than 0.100s). In addition, the minimal value will always occur somewhere inside the particle due to geometric features that heavily impede the diffusion. Since it is evident that diffusion within the particle is greater in the resolved model, H_2 is better able to escape the particle to the surrounding environment, reaching the equilibrium state at a faster rate compared to the unresolved model.

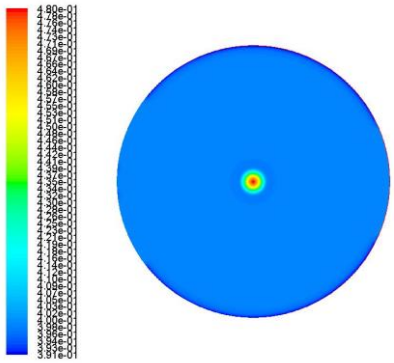

(a) 0.100s – Max: 0.480/ Min:0.391

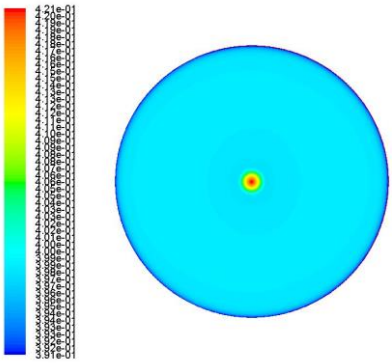

(b) 0.200s – Max: 0.421/ Min:0.391

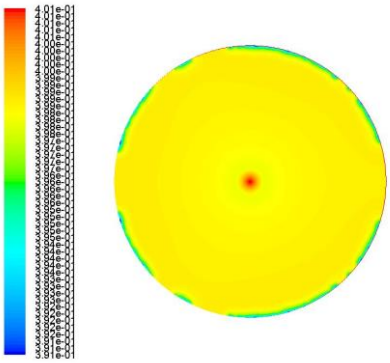

(c) 0.300s – Max: 0.401/ Min:0.391

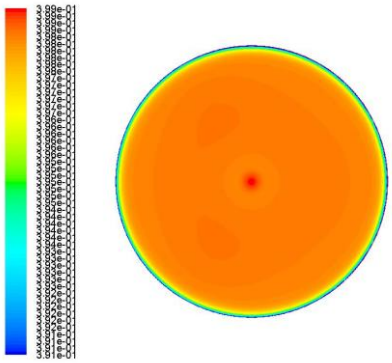

(d) 0.400s – Max: 0.399/ Min:0.391

Figure 4-5. Unresolved Contour Plot of CO Mole Fraction

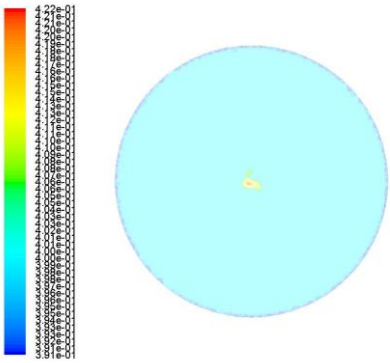

(a) 0.100s – Max: 0.422/ Min:0.391

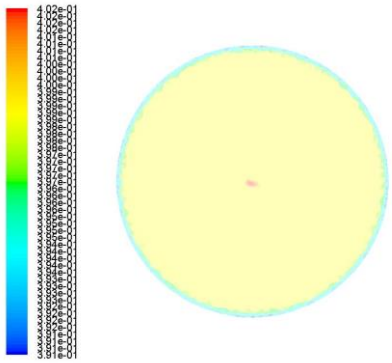

(b) 0.200s – Max: 0.402/ Min:0.391

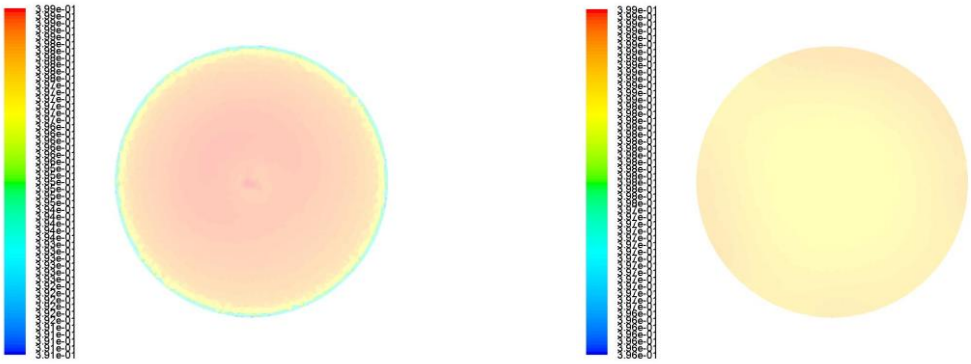

(c) 0.300s – Max: 0.399/ Min:0.391 (d) 0.400s – Max: 0.399/ Min:0.396

Figure 4-6. Resolved Contour Plot of CO Mole Fraction

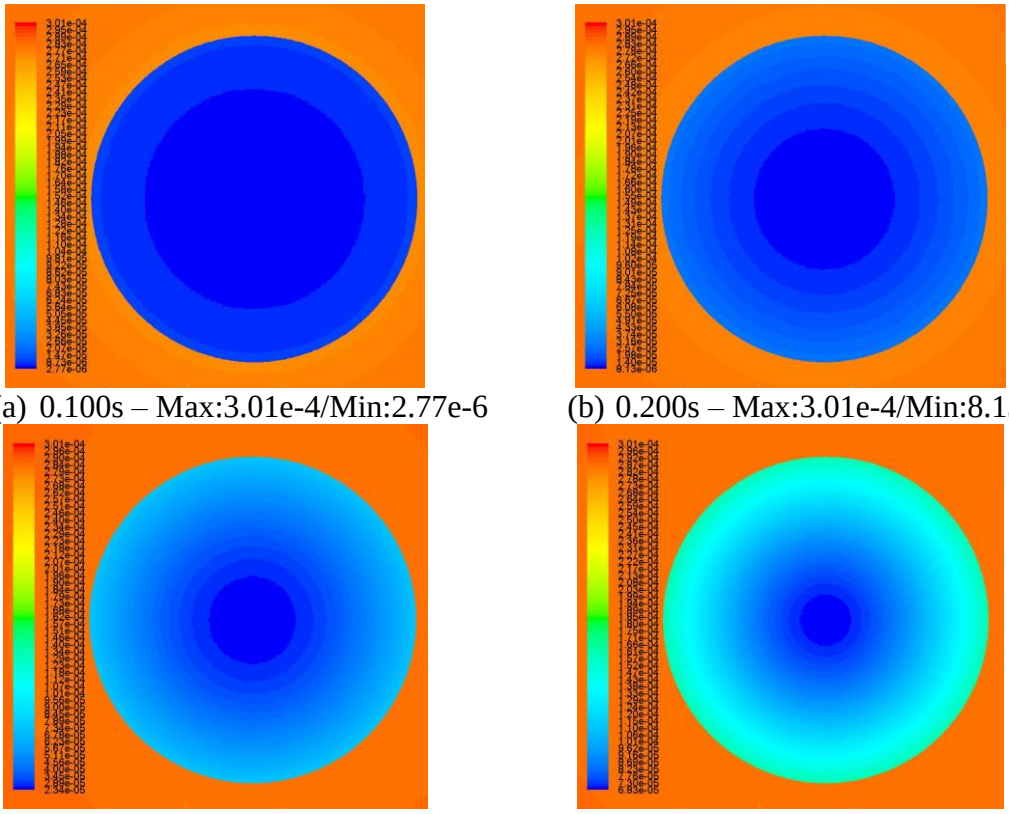

(a) 0.100s – Max:3.01e-4/Min:2.77e-6 (b) 0.200s – Max:3.01e-4/Min:8.13e-6

(c) 0.300s – Max:3.01e-4/Min:2.34e-5 (d) 0.400s – Max:3.01e-4/Min:6.83e-5

Figure 4-7. Unresolved Contour Plot of CO to Mixture Diffusion Coefficient (m^2/s)

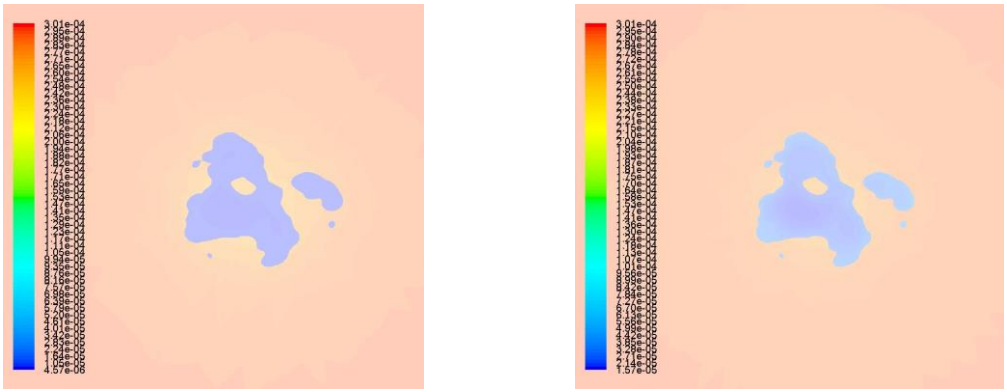

(a) 0.100s – Max:3.01e-4/Min:4.57e-6 (b) 0.200s – Max:3.01e-4/Min:1.57e-5

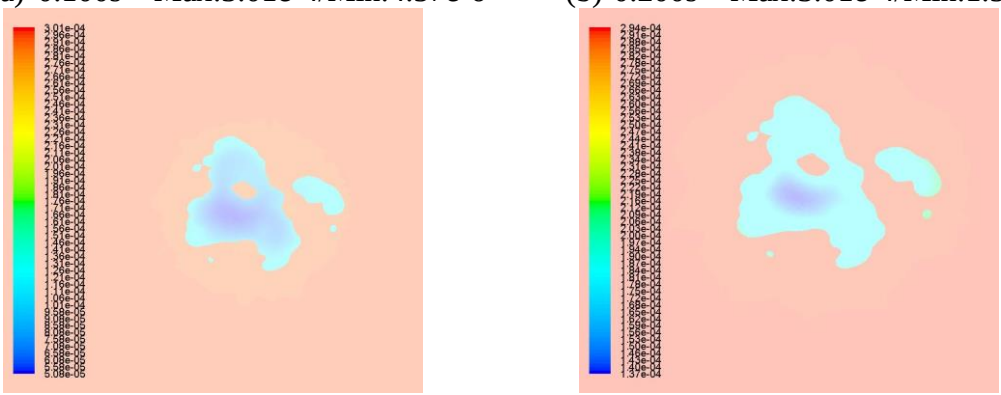

(c) 0.300s – Max:3.01e-4/Min:5.08e-5 (d) 0.400s – Max:2.94e-4/Min:1.37e-4

Figure 4-8. Resolved Contour Plot of CO to Mixture Diffusion Coefficient (m^2/s)

The next set of species contour plots are CO and shown above. The plots share high similarities and trends discussed from the other produced species, H_2. Although the trends have already been discussed in depth, CO is able to emphasize the effect of the resolved geometric features. In this specific set, CO is able to highlight the effects of additional geometric features, such as the void in the middle of the particle on species, primarily the diffusion coefficient. This feature is most notable during the progression of Figure 4-8c to 4-8d, which illustrates a time period where the sufficient amount of the particle has decayed and the void becomes an additional facet where produced species can diffusion in the environment at the same rate as the external surface areas.

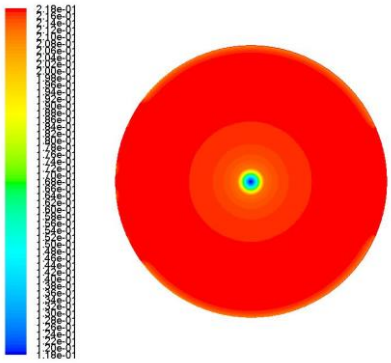

(a) 0.100s – Max: 0.218/ Min:0.118

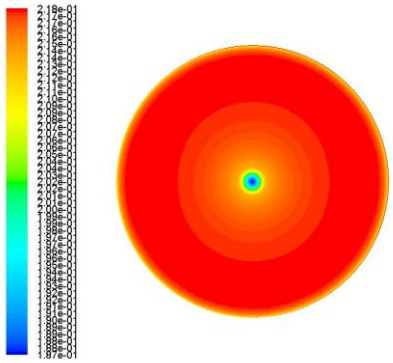

(b) 0.200s – Max: 0.218/ Min:0.187

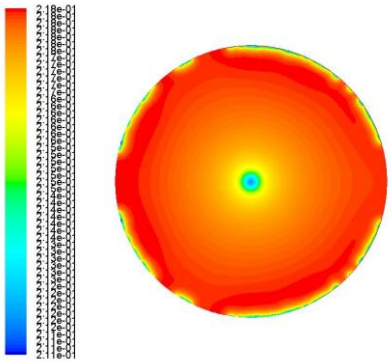

(c) 0.300s – Max: 0.218/ Min:0.211

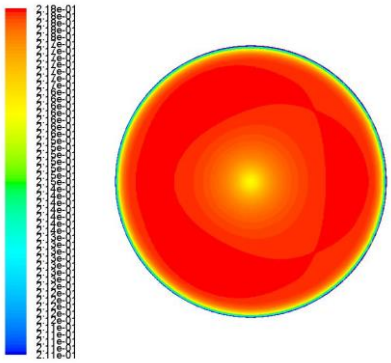

(d) 0.400s – Max: 0.218/ Min:0.211

Figure 4-9. Unresolved Contour Plot of H_2O Mole Fraction

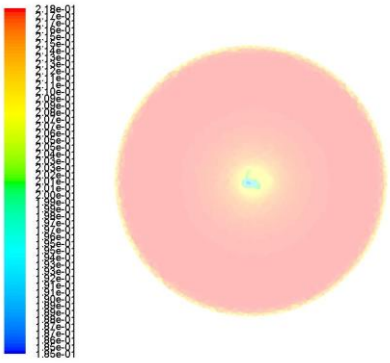

(a) 0.100s – Max: 0.218/ Min:0.185

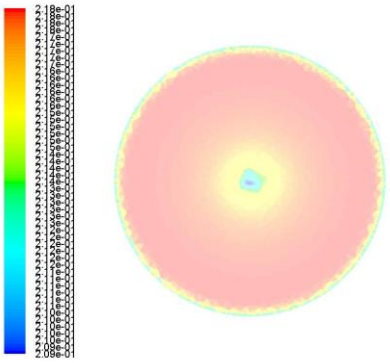

(b) 0.200s – Max: 0.218/ Min:0.209

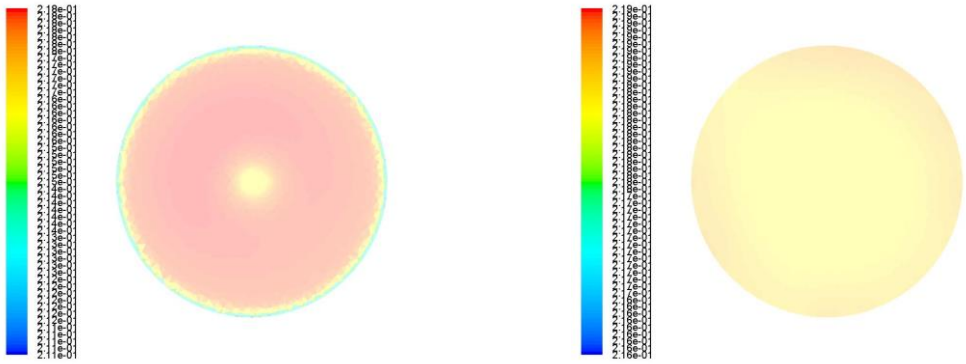

(c) 0.300s – Max: 0.218/ Min:0.211 (d) 0.400s – Max: 0.219/ Min:0.216

Figure 4-10. Resolved Contour Plot of H_2O Mole Fraction

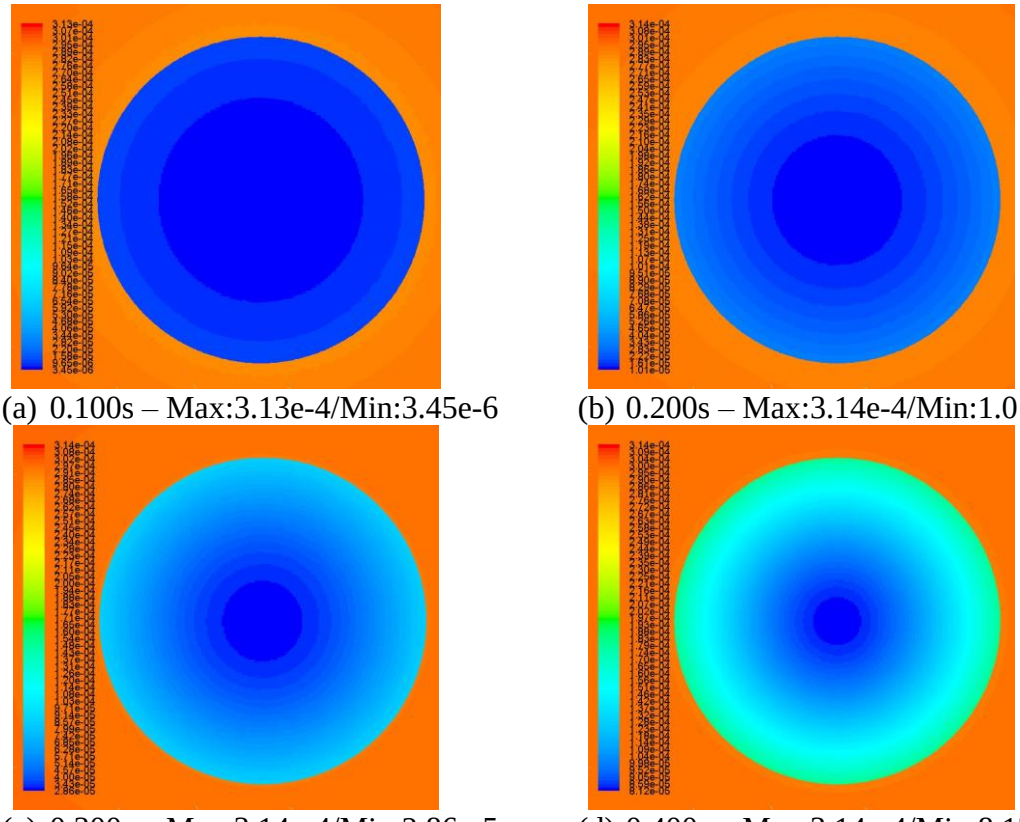

(a) 0.100s – Max:3.13e-4/Min:3.45e-6 (b) 0.200s – Max:3.14e-4/Min:1.01e-5

(c) 0.300s – Max:3.14e-4/Min:2.86e-5 (d) 0.400s – Max:3.14e-4/Min:8.12e-5

Figure 4-11. Unresolved Contour Plot of H_2O to Mixture Diffusion Coefficient (m^2/s)

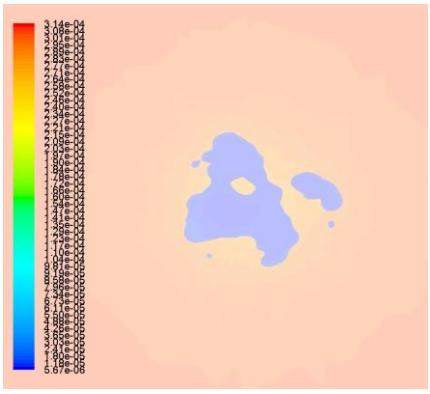

(a) 0.100s – Max:3.14e-4/Min:5.67e-6

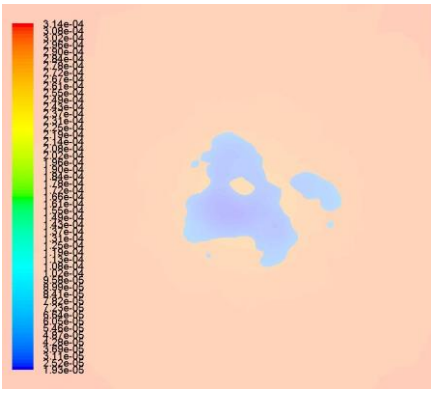

(b) 0.200s – Max:3.14e-4/Min:1.93e-5

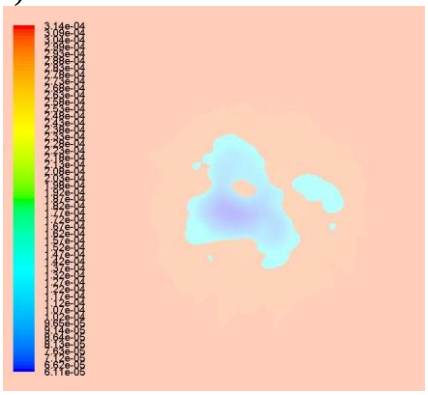

(c) 0.300s – Max:3.14e-4/Min:6.11e-5

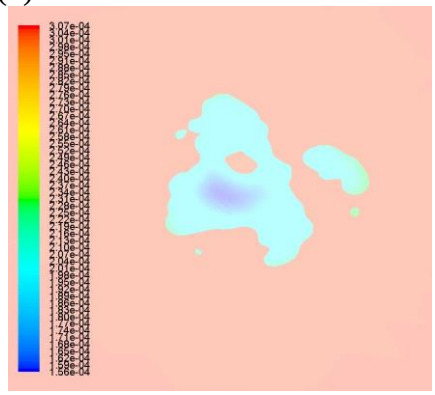

(d) 0.400s – Max:3.07e-4/Min:1.56e-4

Figure 4-12. Resolved Contour Plot of H_2O to Mixture Diffusion Coefficient (m^2/s)

The next set of contour plots covers the mole fraction and the diffusion coefficient of H_2O, shown above. Since H_2O is a reactant for reaction 2, the species will be consumed when in contact with the particle until the reaction has ceased due to particle consumption. Overall, both models show a qualitative trend of the minimum H_2O located in the center of the particle at all times. Although this may be the case, the resolved simulation is shown to again reach the equilibrium state more quickly once the particle has been sufficiently decayed. Evidence of this claim can be seen in the mole fraction contour plots, Figure 4-5 and 4-6. From these figures, it is evident that at time 0.400s, the resolved model qualitatively demonstrates equilibrium characteristics, such as minimal indication of species gradients. In addition, Figure 4-9b and Figure 4-10a show similarities in terms of

qualitative profile along with the contour plot range. This is somewhat substantial as the comparison indicates that the unresolved model is lagging behind the resolved models at every stage and this is emphasized at the earlier particle life.

Similar to H_2, the H_2O to mixture diffusion coefficient serves as evidence that not only the H_2O has reached the equilibrium state faster but when the particle has been approximately depleted. The H_2O diffusion coefficient shows a similar trend as H_2, as the minimum diffusion coefficients for the resolved model are significantly higher than the unresolved case. The increased diffusion coefficients are caused by relatively increased amount of particle decay, which ultimately enhances the mass transport throughout the particle. This affects the species consumption rate, as the reactant is able to further penetrate into the particle resulting in opportunities for surface area to become available. Once more sites are available, the particle will begin to decay at an accelerated rate, thus reaching a constant species profile or better known as Zone I conditions faster. It is emphasized that both models have the approximately the same amount of surface area as the specific area, 480 m^2/g, is implemented in both models and both particle models are equivalent. Also, the resolved diffusion contour plots indicate smaller gradients, meaning that the reactant is better able to penetrate into the particle.

Lastly, between the two models, the higher diffusion coefficients within the particle are confined to the outer edge of the sphere in the unresolved case but not on the outer edge of the resolved structure. From the analysis of Figure 4-12, it is evident that the void in the middle of the particle slowly acts as another method of introducing more species deeper into the particle. Consequentially, the reactant diffusion begins to increase surrounding this additional entrance mode, exposing particle's surface area to more reactants thus faster

particle progression. The effect of the center void is highlighted from Figure 4-8b to Figure 4-8d. These differences in diffusion gradients and profiles are emphasized in Figure 4-7d and Figure 4-8d.

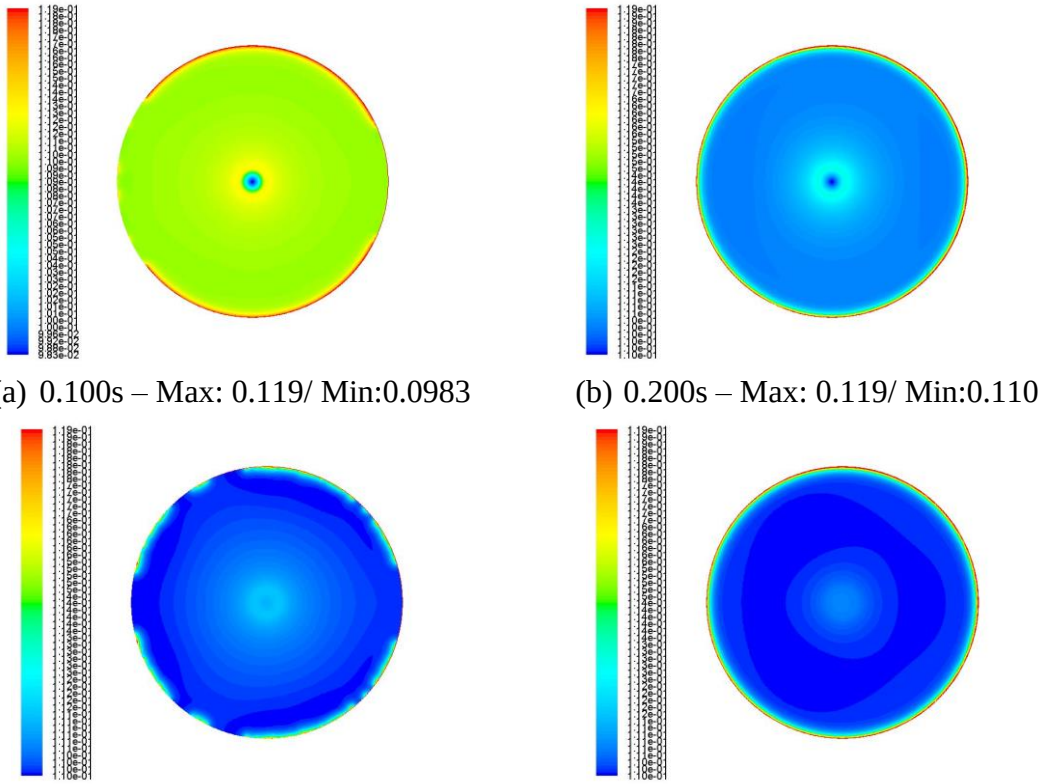

(a) 0.100s – Max: 0.119/ Min:0.0983 (b) 0.200s – Max: 0.119/ Min:0.110

(c) 0.300s – Max: 0.119/ Min:0.110 (d) 0.400s – Max: 0.119/ Min:0.110

Figure 4-13. Unresolved Contour Plot of CO_2 Mole Fraction

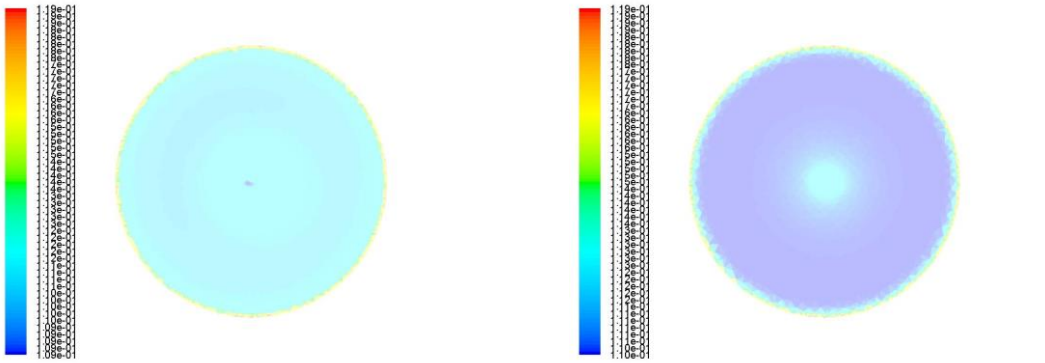

(a) 0.100s – Max: 0.109/ Min:0.119 (b) 0.200s – Max: 0.110/ Min:0.119

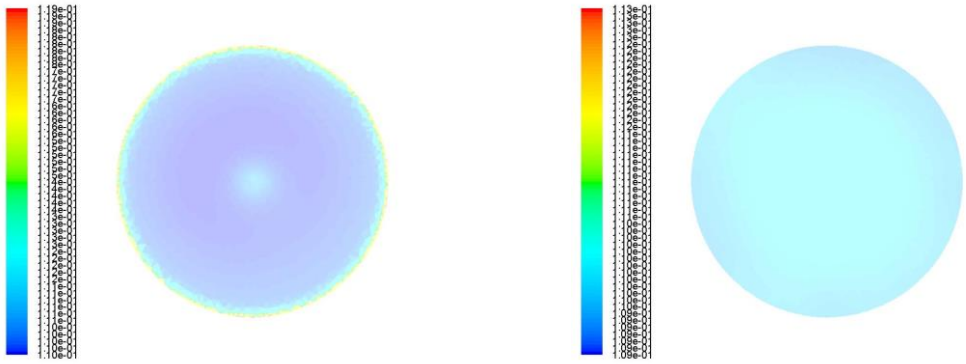

(c) 0.300s – Max: 0.119/ Min:0.110 (d) 0.400s – Max: 0.109/ Min:0.113

Figure 4-14. Resolved Contour Plot of CO_2 Mole Fraction

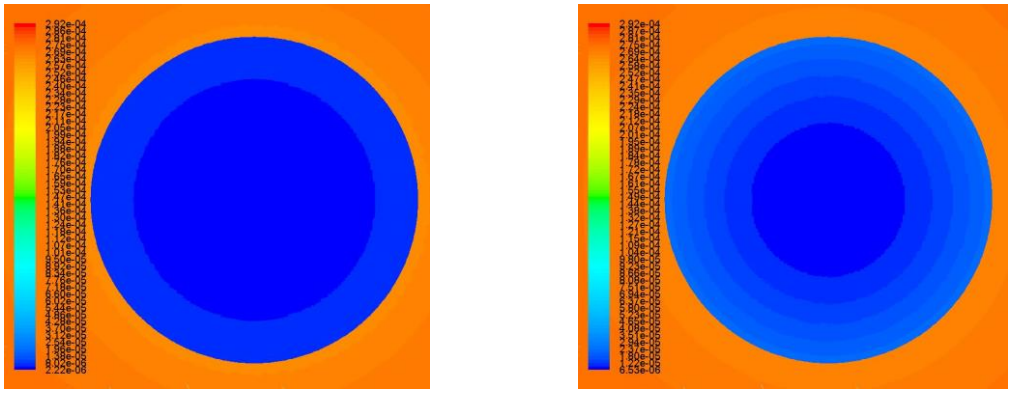

(a) 0.100s – Max:2.92e-4/Min:2.22e-6 (b) 0.200s – Max:2.92e-4/Min:6.53e-6

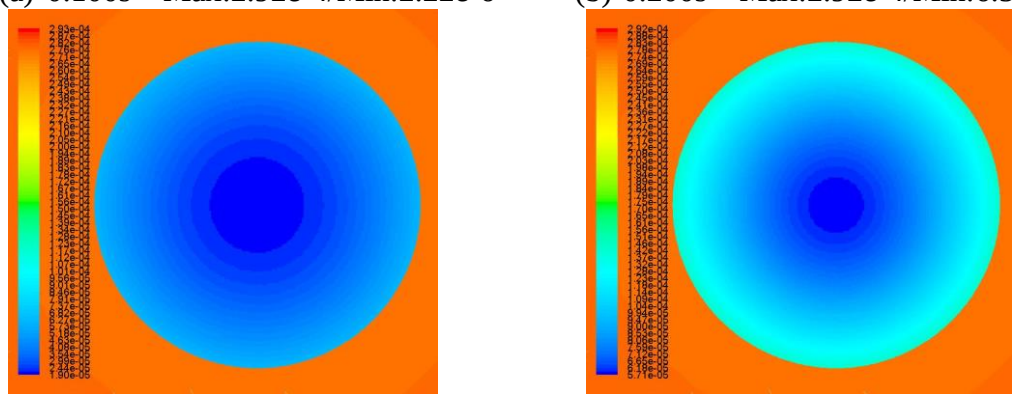

(c) 0.300s – Max:2.93e-4/Min:1.90e-5 (d) 0.400s – Max:2.92e-4/Min:5.71e-5

Figure 4-15. Unresolved Contour Plot of CO_2 to Mixture Diffusion Coefficient (m^2/s)

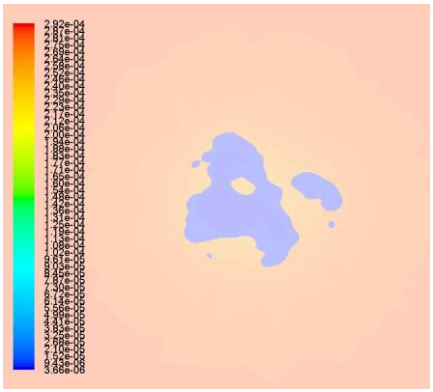

(a) 0.100s – Max:2.92e-4/Min:3.66e-6

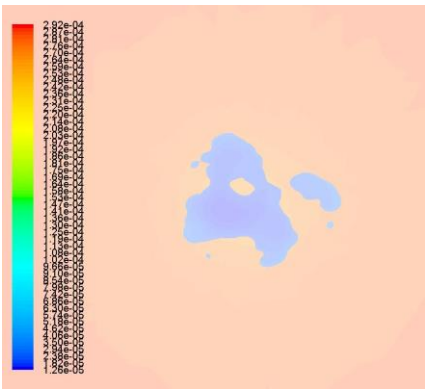

(b) 0.200s – Max:2.92e-4/Min:1.26e-5

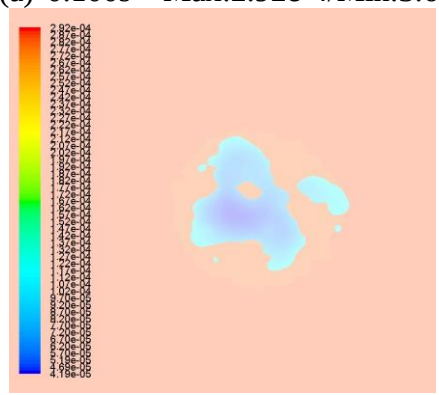

(c) 0.300s – Max:2.92e-4/Min:4.19e-5

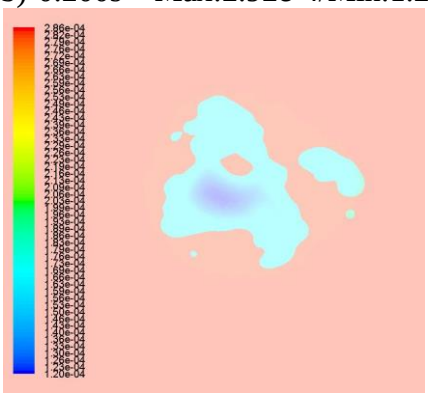

(d) 0.400s – Max:2.86e-4/Min:1.20e-4

Figure 4-16. Resolved Contour Plot of CO_2 to Mixture Diffusion Coefficient (m^2/s)

The next set of contour plots shows the mole fraction and the diffusional coefficient of CO_2. CO_2 is the other reactant during gasification, consumed in reaction 1. As evident from the set of figures above, Figure 4-13 to 4-16, CO_2 is able to penetrate the particle to a greater extent than its reactant counterpart, H_2O. This can be related back to Tremel kinetics that indicate that reaction 2 (H_2O) occurs significantly faster than reaction 1 (CO_2), which translates into relatively less resistance attributed from species consumption for the transport of the reactant CO_2 thus allowing faster CO_2 penetration into the particle. Even though CO_2 is essentially able to reach Zone I conditions before H_2O, the resolved model progresses faster than the unresolved model. This can be attributed same reasoning discussed in H_2O but most notable cause is geometric features, such as the center void in

the particle cross section. The regions around the void contain similar diffusion coefficients as the regions by the surrounding area at all times but is emphasized in earlier times shown in Figure 4-16b. This void in particular, reveals an additional mode of reactant and particle interaction that, along with other stated factors, cause an accelerate particle progression due to increase surface area exposure. Again, it is highlighted that the resolved diffusion coefficient is significantly higher compared to the unresolved counterpart. Compared to the H_2O contour plots, CO_2 is better able to illustrate the impact of the center void shown from the rapid increase in diffusion coefficient from Figure 4-12b to Figure 4-12c.

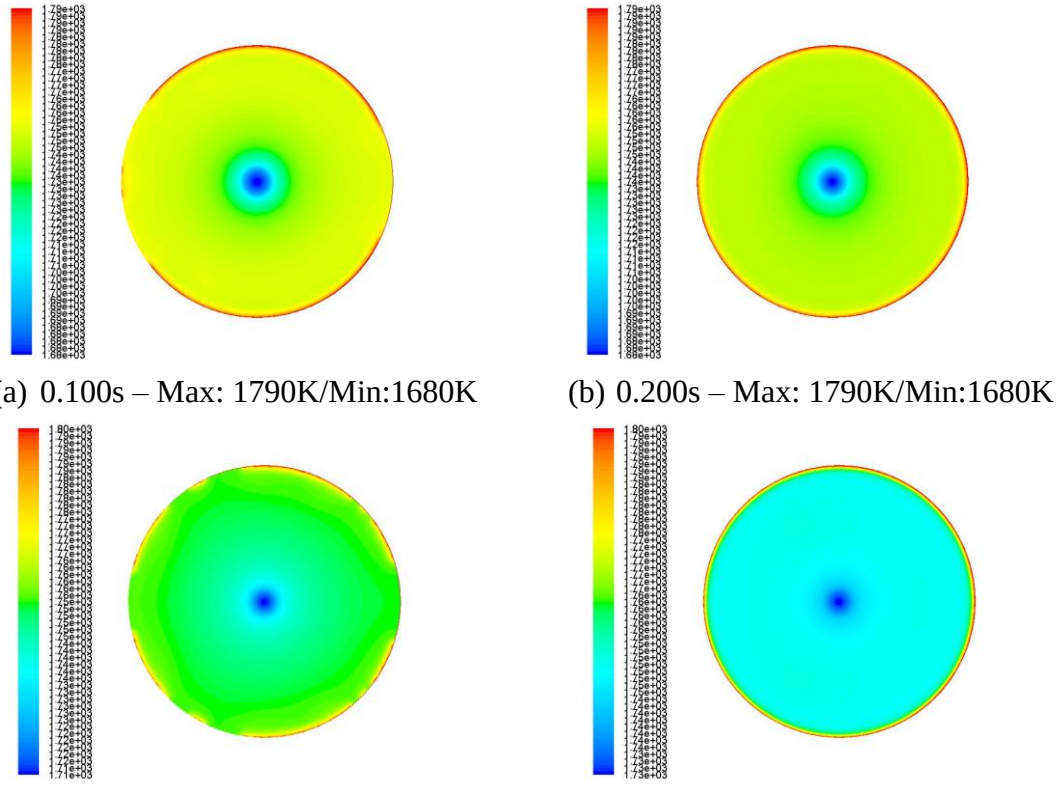

(a) 0.100s – Max: 1790K/Min:1680K (b) 0.200s – Max: 1790K/Min:1680K

(c) 0.300s – Max: 1800K/Min:1710K (d) 0.400s – Max: 1800K/Min:1730K

Figure 4-17. Unresolved Contour Plot of Temperature (K)

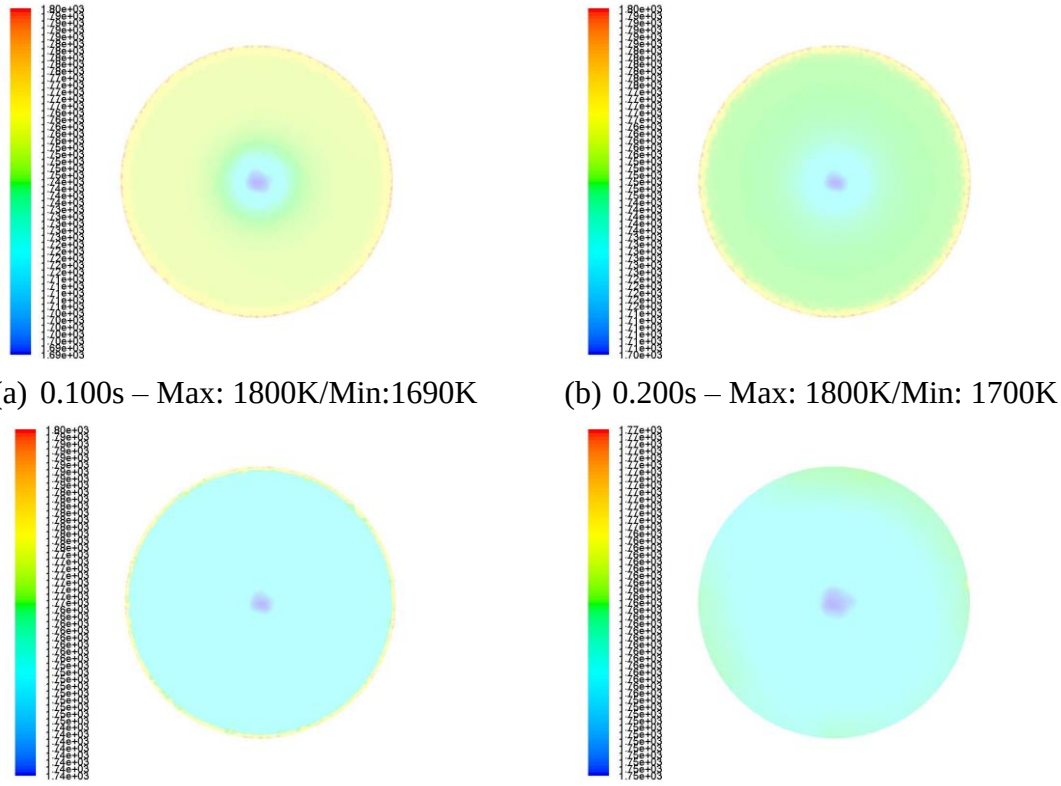

(a) 0.100s – Max: 1800K/Min:1690K (b) 0.200s – Max: 1800K/Min: 1700K

(c) 0.300s – Max: 1800K/Min: 1740K (d) 0.400s – Max: 1770K/Min: 1750K

Figure 4-18. Resolved Contour Plot of Temperature (K)

The next set of contour plots compares the temperature profiles for the resolved and unresolved model. The minimum temperature is located near the center of the particle, which is logical, as gasification reactions are endothermic, which act as resistance to thermal energy penetration into particle. Knowing that, the minimum of the temperature should also theoretical give insight the amount of gasification that has occurred such that the lower the minimum temperature, the more gasification has occurred. This theoretical trend is not consistent with the trend found the later sets of resolved reaction rate contour plots and conversion profiles where the resolved reaction rates are proven to be more frequent yet the temperature remains greater than the unresolved model. This can be explained when analyzing the resolved geometry from Figure 3-8 where additional

penetration modes are presented. Via the additional penetration modes, the surrounding environment is able to penetrate further into the particle with minor interactions with the particle, thus retaining a significant portion of its thermal energy. Since there is a greater amount thermal energy available deeper within the particle, the energy consumption that would have occurred due to gasification reaction on the outer particle region is partially counteracted while also augmenting the gasification reactions. As the particle continues to decay, the amount of surface area also decays causing the gasification endothermic nature to wane, thus increasing temperature as indicated in both contour plot sets. Lastly, the particle's temperature profiles are notably different as the resolved model displays non-symmetrical profile, which can be attributed to the non-uniform geometric features that promote gasification reactions via higher penetration and surface area.

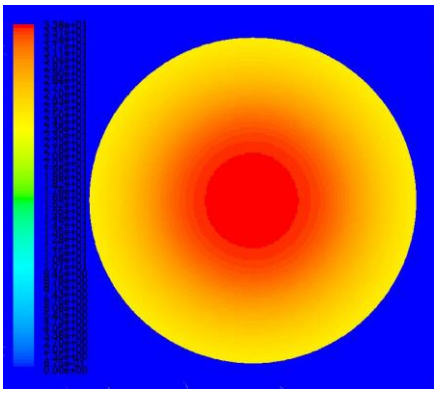

(a) 0.050s – Max: 33.8 / Min:0

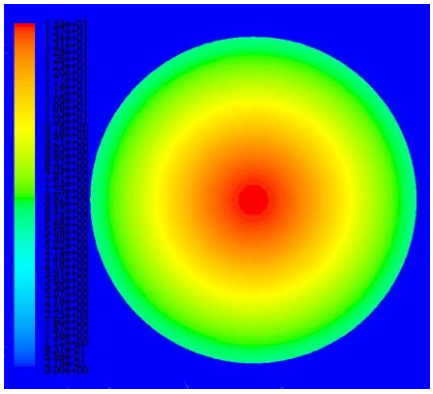

(b) 0.200s – Max: 13.8/ Min:0

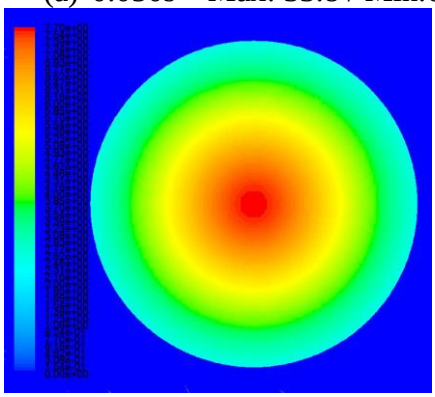

(c) 0.300s – Max: 7.70/ Min:0

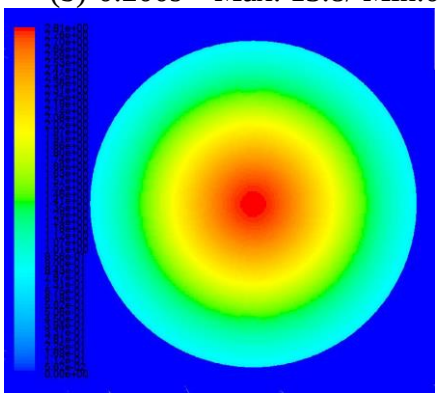

(d) 0.400s – Max: 2.81/ Min:0

Figure 4-19. Unresolved Contour Plot of Reaction Rate 3 (kmol/m3-s)

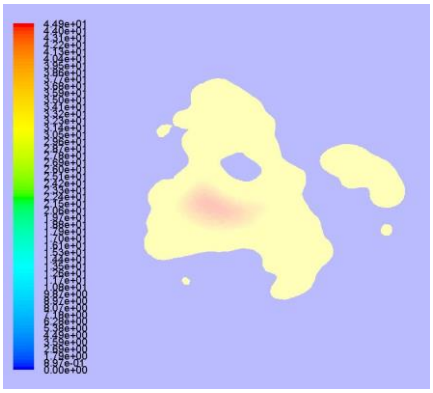

(a) 0.050s – Max: 49.9/ Min:0

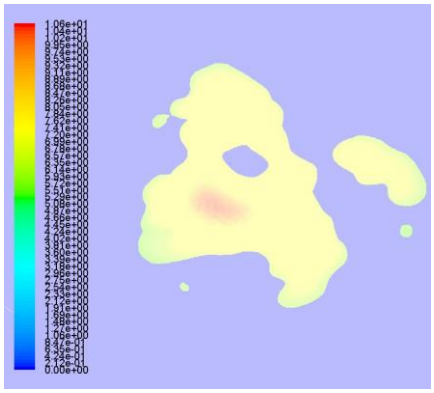

(b) 0.200s – Max: 10.6/ Min:0

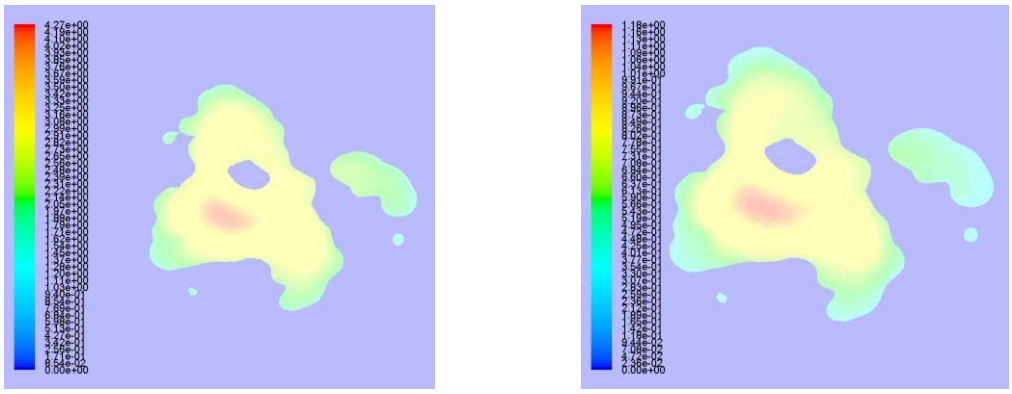

(c) 0.300s – Max: 4.27/ Min:0.0 (d) 0.400s – Max: 1.18/ Min:0

Figure 4-20. Resolved Contour Plot of Reaction Rate 3 (kmol/m3-s)

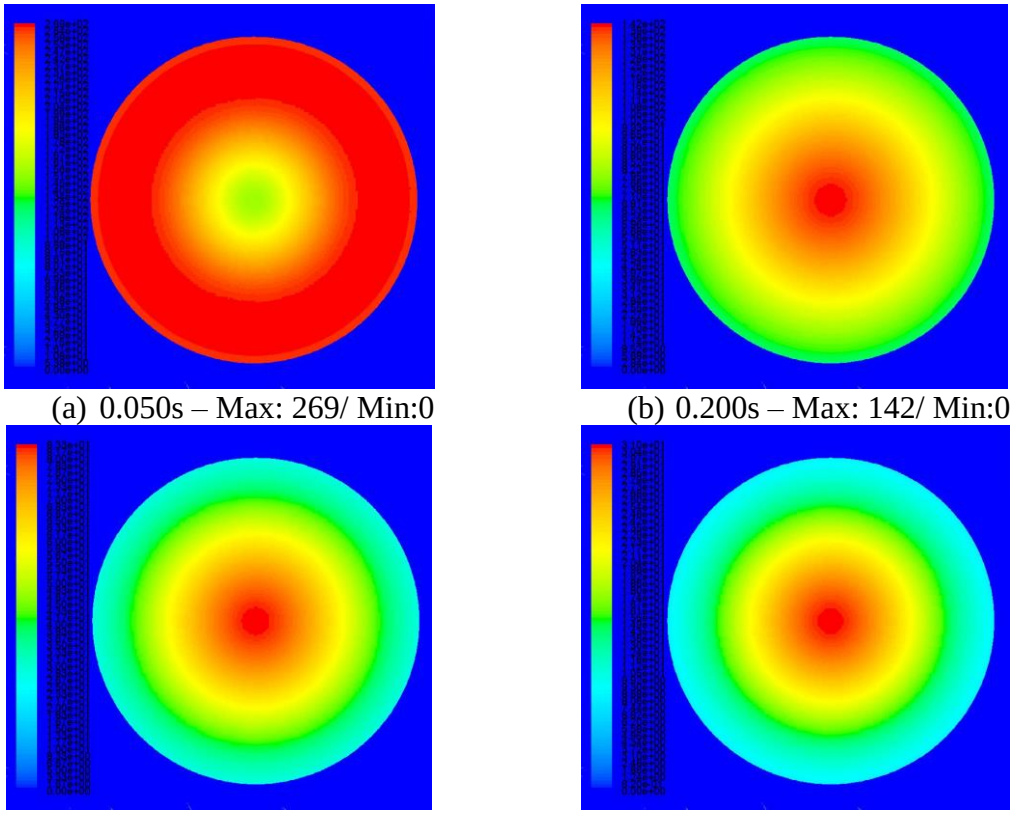

(a) 0.050s – Max: 269/ Min:0 (b) 0.200s – Max: 142/ Min:0

(c) 0.300s – Max: 83.3/ Min:0 (d) 0.400s – Max: 31.0 / Min:0

Figure 4-21. Unresolved Contour Plot of Reaction Rate 4 (kmol/m3-s)

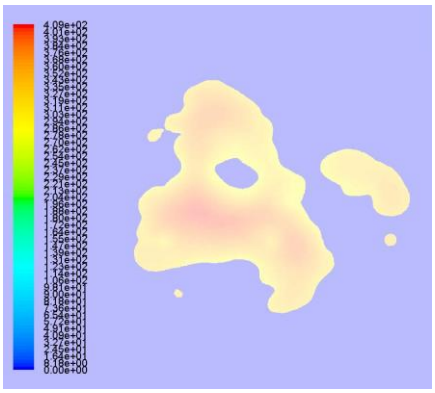

(a) 0.050s – Max: 409 / Min:0

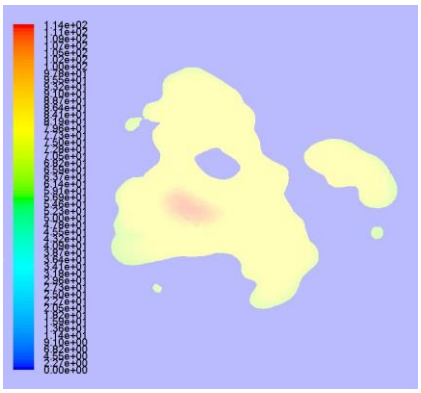

(b) 0.200s – Max: 114 / Min:0

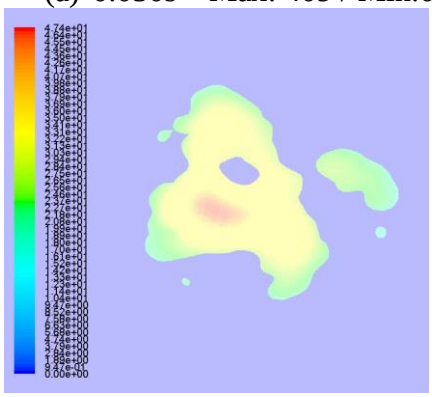

(c) 0.300s – Max: 47.4/ Min:0

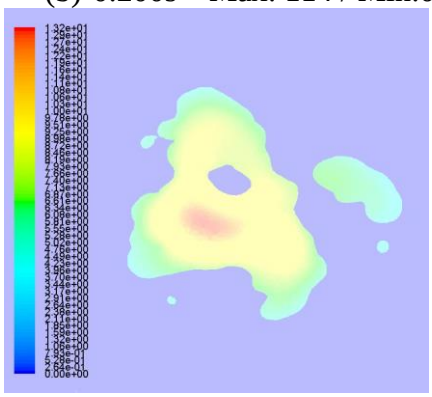

(d) 0.400s – Max: 13.2/ Min:0

Figure 4-22. Resolved Contour Plot of Reaction Rate 4 (kmol/m3-s)

To better understand the temperature profile, the driving factors, gasification reaction rates, are discussed from the contour plots above. The first detail that must be addressed is that the maximum gasification reaction rates are located at the center of the particle even though previous contour plots indicate lower temperatures and reactants within this same region. This can be explained as by 0.050s (Figure 4-21a), a significant amount of gasification has occurred on the first penetrated areas or the initial exposed surface areas causing a reduction of surface area. After this initial timeframe, the majority of viable reaction sites remain near the center of the particle. This indicates that the available surface area or remaining char structure is the reactive limiting factor as there is no possible shortage of other kinetic factors such as reactant and temperature due to model

set-up. The effects of the resolved geometric features are also highlighted as at 0.050s, as the reaction rates exhibit Zone I behaviors shown from the approximate evenly distributed reaction rate throughout the particle, compared to the unresolved model, which still exhibit transitional behavior between Zone I and II.

The reaction rate contour plots also serve as focal point to determine if there is a significant difference between the two geometries. Although this is difficulty to determine qualitatively, a general trend can be extrapolated via reaction rate maximums. The maximums of each reaction can be utilized as a measurement of the particle potential in terms of reaction rates meaning the higher the maximums, the higher the overall particle reaction rate should be. Using this logic and the contour plots, it can be seen that the resolved model further intensifies the gasification reactions at an earlier time frame, more specifically from 0s to 0.0715s, but afterwards, less than the unresolved model. This serves an indication that the resolved gasification reactions are initially amplified by the geometry until the geometry's surface area begin to be depleted allowing the unresolved reaction rates to overcome the resolved model. Additional justification is shown in later sections.

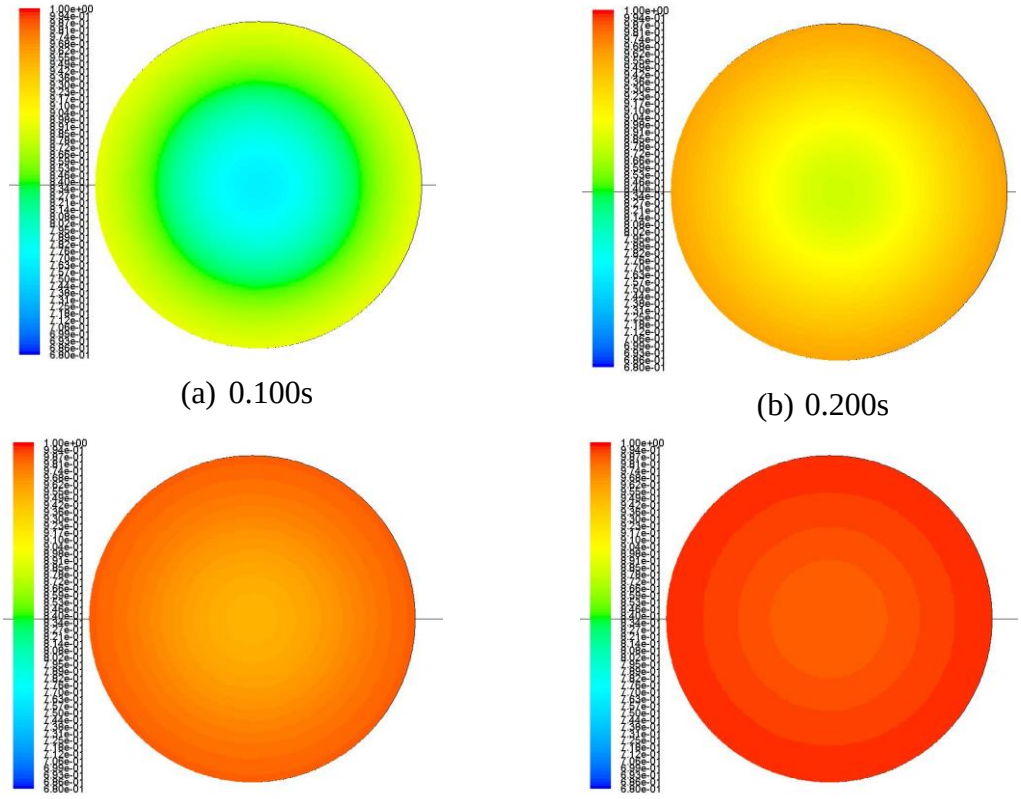

(a) 0.100s (b) 0.200s

(c) 0.300s (d) 0.400s

Figure 4-23. Unresolved Contour Plot of Porosity - Max: 1.00 / Min: 0.68

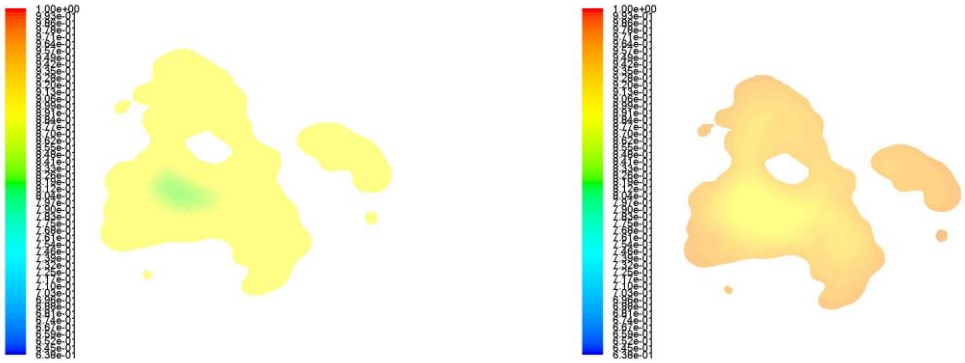

(a) 0.100s (b) 0.200s

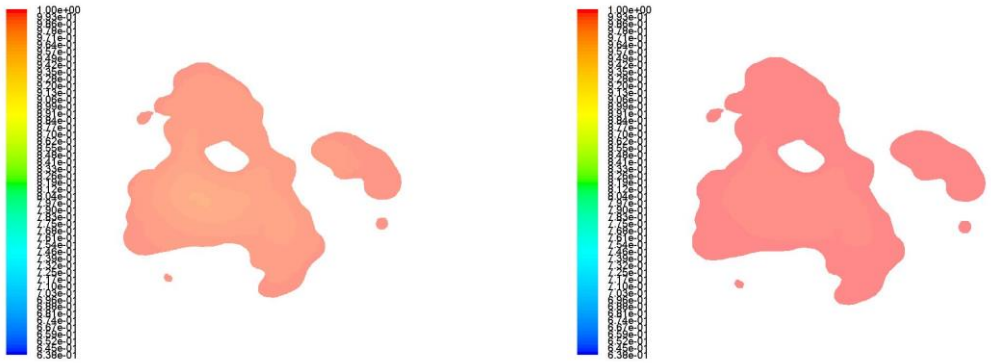

(c) 0.300s (d) 0.400s

Figure 4-24. Resolved Contour Plot of Porosity – Max: 1.00/Min: 0.638

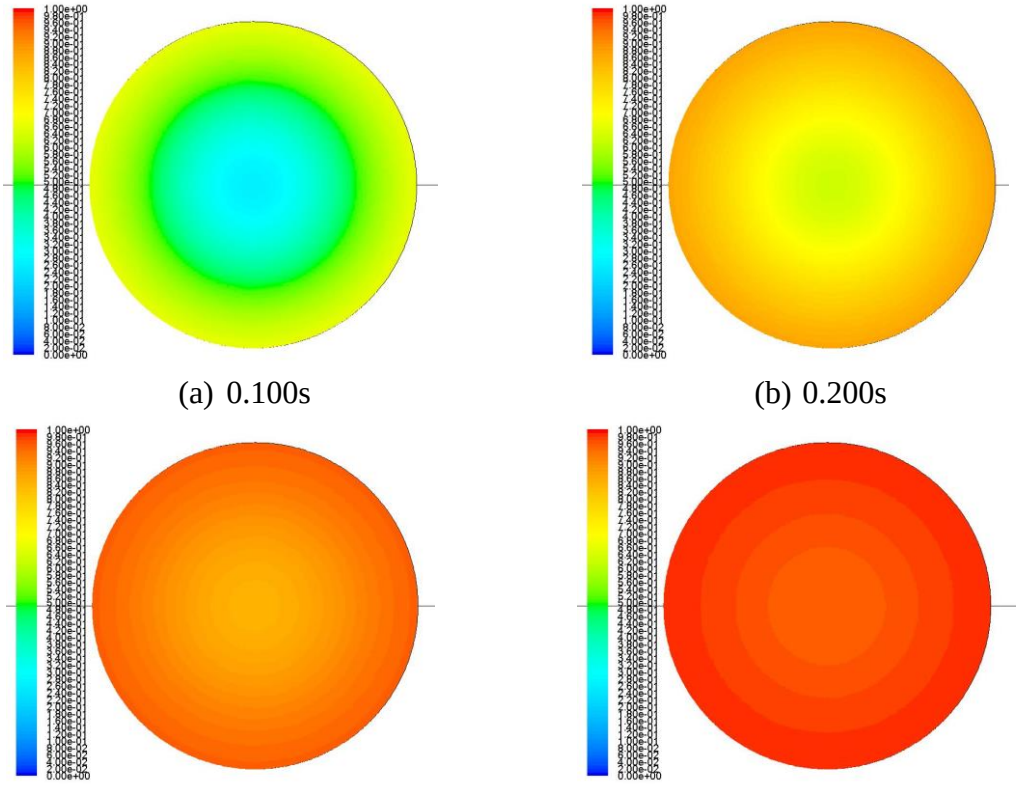

(a) 0.100s (b) 0.200s

(c) 0.300s (d) 0.400s

Figure 4-25. Unresolved Contour Plot of Conversion – Max: 1.00 / Min: 0

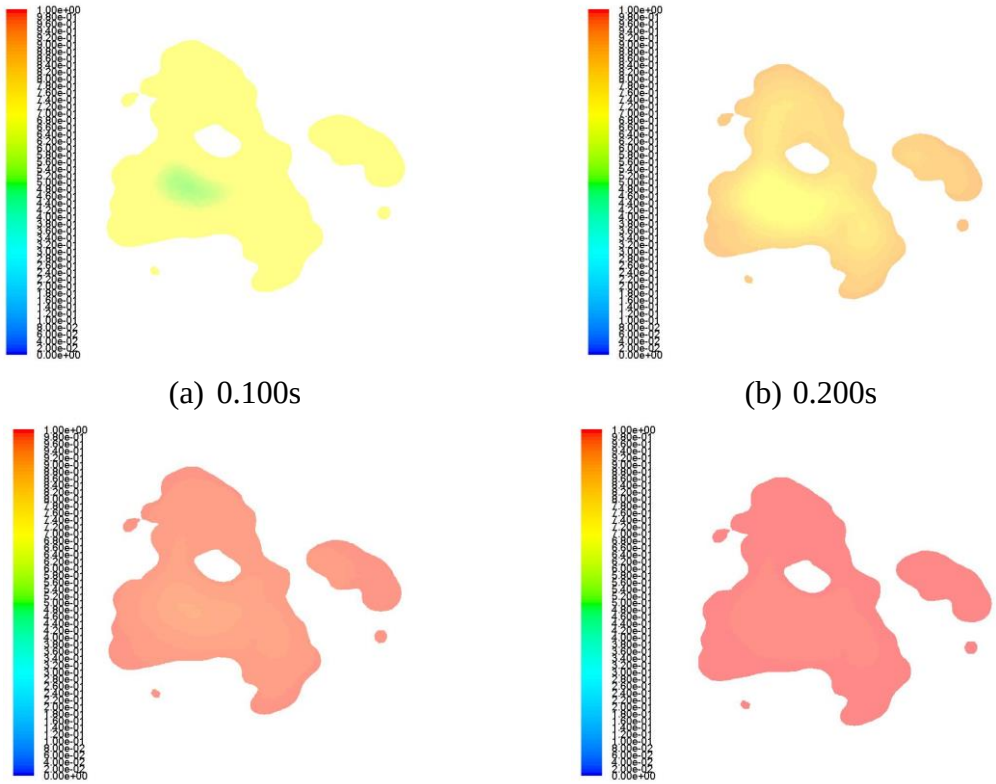

(a) 0.100s (b) 0.200s

(c) 0.300s (d) 0.400s

Figure 4-26. Resolved Contour Plot of Conversion – Max: 1.00/ Min:0.00

Lastly, both the model's resultant conversion and porosity are presented above and discussed. A glaring difference between the two models at 0.400s is evident when comparing Figure 4-25d and Figure 4-26d. At 0.400s, the resolved model (Figure 4-26d) indicates a uniform, approximately fully consumed char particle while the unresolved model (Figure 4-25d) shows the particle nearing completion with distinct conservation gradients still remain. In order to understand the causes of the differences between the two models, earlier times must be analyzed. From the isolated region in Figure 4-26b, it is evident that regions that are surrounded or highly exposed to the surrounding fluids and resultantly accelerate the conversion. This phenomenon can be explained by the fact that region has significant external surface area that increases the potential interaction with

fluid, allowing for more regions for gasification to occur on. With these regions of high fluid exposure, the total penetration distance, or distance from external area to external area, is significantly lower than that of the unresolved model whose particle representation is 100 microns. By reducing the required penetration distance, the reactants will reach their steady state concentration levels at a faster rate, thus maximizing the amount of internal gasification, resulting in a substantial increase in conversion.

Since both unresolved and resolved contour plots have the same range for the conversion contour plots, the qualitative profiles are directly comparable (as opposed to porosity, which has different ranges as explained in section Chapter 3. From interpretation of the conversion plots, it is evident that the resolved model does not contain lower values than the unresolved model at any location. An example of this is at 0.100s, the unresolved model (Figure 4-25a) contains a shade of light blue whereas the lowest value shade from Figure 4-26a, is light green and is greater in value than light blue. Also at 0.100s, the resolved model indicates minimal conversion gradients, unlike the unresolved model, which indicates distinct and significant gradients. Although the unresolved conversion gradients are attenuated as time progresses, the unresolved gradients still exist and are noticeable when compared to the minimal gradients of the resolved case. This trend follows the general narrative found in all sets of contour plots: that the unresolved model overestimates gradients within and surrounding the particle, while the resolved model demonstrates minimal gradients. This difference was consistently determined be the result of geometric features (e.g. voids) that add additional facets where the reactant can interact with the particle and paths for reactant penetration and accelerate the overall particle progression.

4.2 One-Dimensional Profiles

Although contour plots do provide a good means of conveying data qualitatively, there is too much information presented, which may hinder a conclusive difference between the two models from being determined. Therefore, to additionally analyze the data, one-dimensional profiles are developed for several variables every 25 ms. The two-dimensional model's data is gathered from the straight line that was defined as axis during development, since the two-dimensional model is practically spherically-symmetric. The three-dimensional model's data is gathered from a series of incremented spheres that are used to calculate the area average (polar and azimuthally-averaged) of the characterizing variables. All spheres coincide with the origin of the simulation and their radii are incrementally increased by 2.5 microns until a sphere has a radius of 100 microns. The smaller increments are used in order better resolve the gradients within and surrounding the particle. Afterwards, the radii are incrementally increased by 50 microns until the end of the domain to capture the remaining environment outside the particle. The characterizing variables of models are the mole fraction of the species (H_2, H_2O, CO_2, and CO) and the temperature. It may be noted that data for every 50^{th} time step or 0.025s was gathered but to reduce confusion, the times, 0.025s, 0.075s, 0.200s, and 0.400s are displayed. The results are shown below.

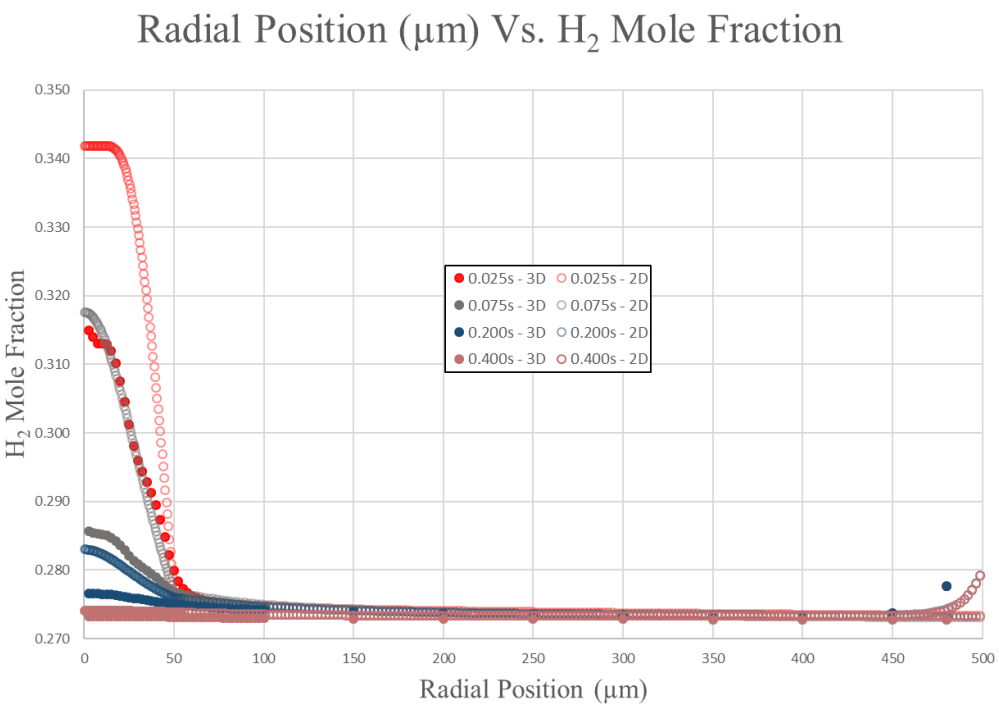

Figure 4-27. One-Dimensional Profile of H_2 Mole Fraction

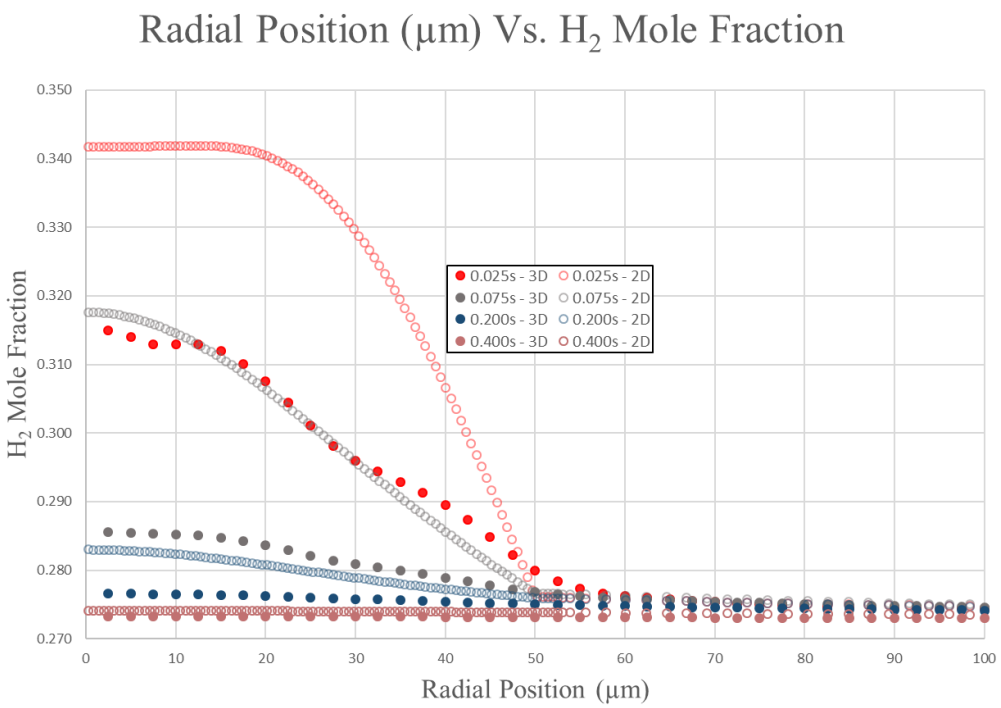

Figure 4-28. One-Dimensional Profile of H_2 Mole Fraction – Zoomed Fig. 4-27

Figures 4-27 to 4-28 are the one-dimensional profiles of the unresolved and resolved models of the species H_2. The main difference between the two models is shown during the initial timeframe (0.025s to 0.125s) before H_2 has begun to converging to its equilibrium state. During this specific timeframe, the H_2 production rate can be shown to begin diminish in both models and begin its convergence to a constant state. From Figure 4-37 to 4-28, the resolved model has comparatively lower produced species concentration than the unresolved model at all times although, from time 0s to 0.0715s, the resolved model is proven to have a superior gasification reaction rates. The resolved accelerated species production is counteracted by the same geometric features that increased penetration modes but in this case, also act as additional exit for produced species. This allows the produced species to rapidly escape the particle via voids and unresolved features

resulting in a lower concentration value even the accelerated species production from the resolved particle. When comparing the diminishing rate between the two models, it is clear that the resolved model displays a faster rate of decay than the unresolved model. For example, between time, 0.025s to 0.050s, at radial position 0 micron, the approximate numerical difference is 0.0175 and 0.005 for the unresolved and resolved models respectively.

Also from the difference between the models' progression are highlight at first recorded time, 0.025s, where the resolved model's H_2 profile is generally has a lower value than that of the unresolved model, especially at center where the difference is approximately 0.25. An attempt is made to fit the resolved profile at 0.025s to the one-dimensional profile to approximately to quantify the relative progression between the two models. This results in the resolved profile at 0.025s being approximately equivalent a profile between 0.050s and 0.075s. As discussed in H_2 contour plots, the resolved geometry enabled a greater amount of gasification reactions from 0s to 0.075s when compared to the unresolved model due an increased accessibility to the surface area and external surface areas causing a significant species production increase. This initial gasification upsurge effect will further accelerate the particle progression.

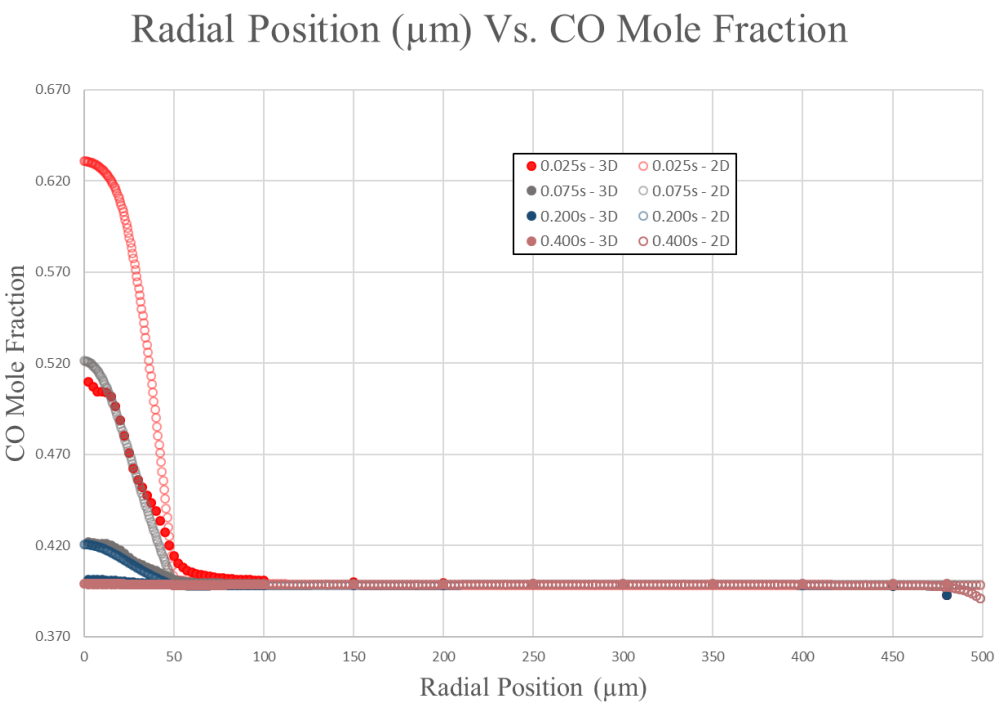

Figure 4-29. One-Dimensional Profile of CO Mole Fraction

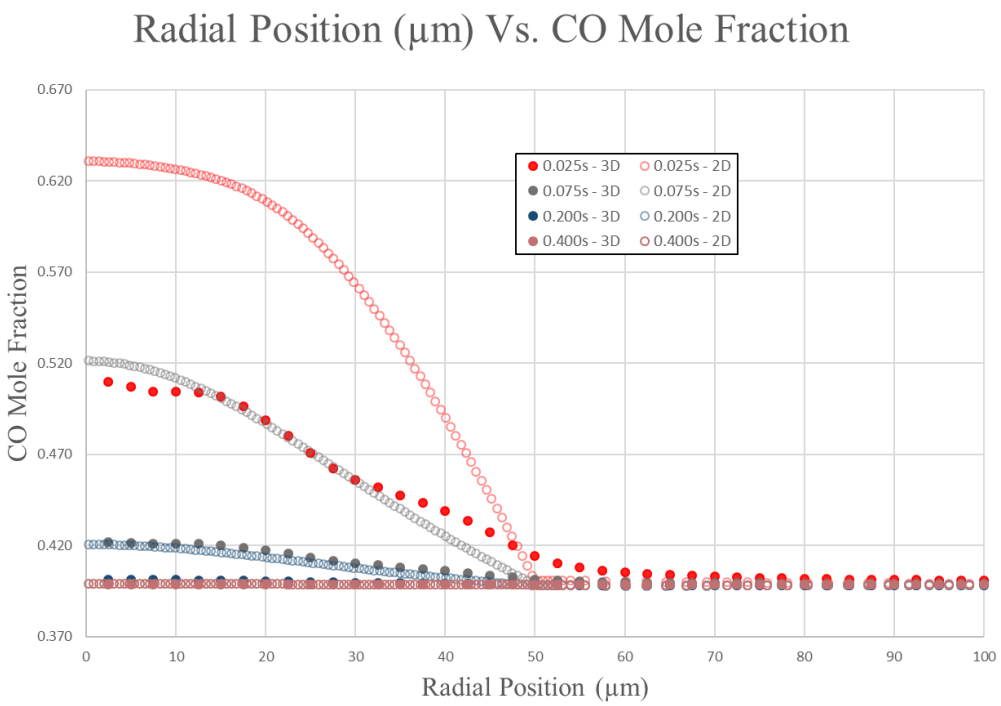

Figure 4-30. One-Dimensional Profile of CO Mole Fraction - Zoomed Fig. 4-29

Similar to other produced species, H_2, the rate at CO display features that indicate high rate of converging to its equilibrium state, evident by the converging profiles, due to previous geometric structure explanations. In addition, the resolved CO concentration is also always lower than the unresolved model due to geometric features expediting the species evacuation out of the particle at a rate that overcomes the initial resolved gasification rate increase. To measure how the progression levels between both models, the same profile fitting procedure (e.g. unresolved profile at 0.025s fits between 0.075s and 0.100s for the resolved profile) that was implemented during the previous species analyzed is executed. From this, the resolved profile from 0.025s is best fitted between the times 0.075s to 0.100s. It may be also noted that both profiles do converge to approximately the same value as time progresses. This fact also can be interpreted as the profiles converge

when the particle's structure is almost depleted thus have minimal effect on species concentration. This statement can be applied to all species profiles.

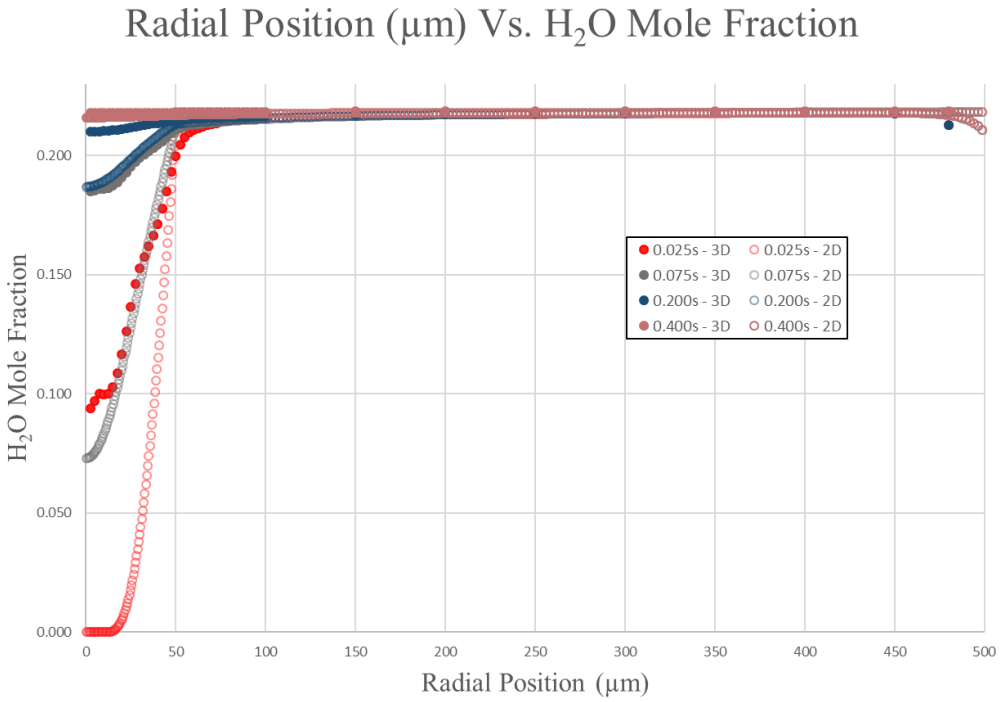

Figure 4-31. One-Dimensional Profile of H_2O Mole Fraction

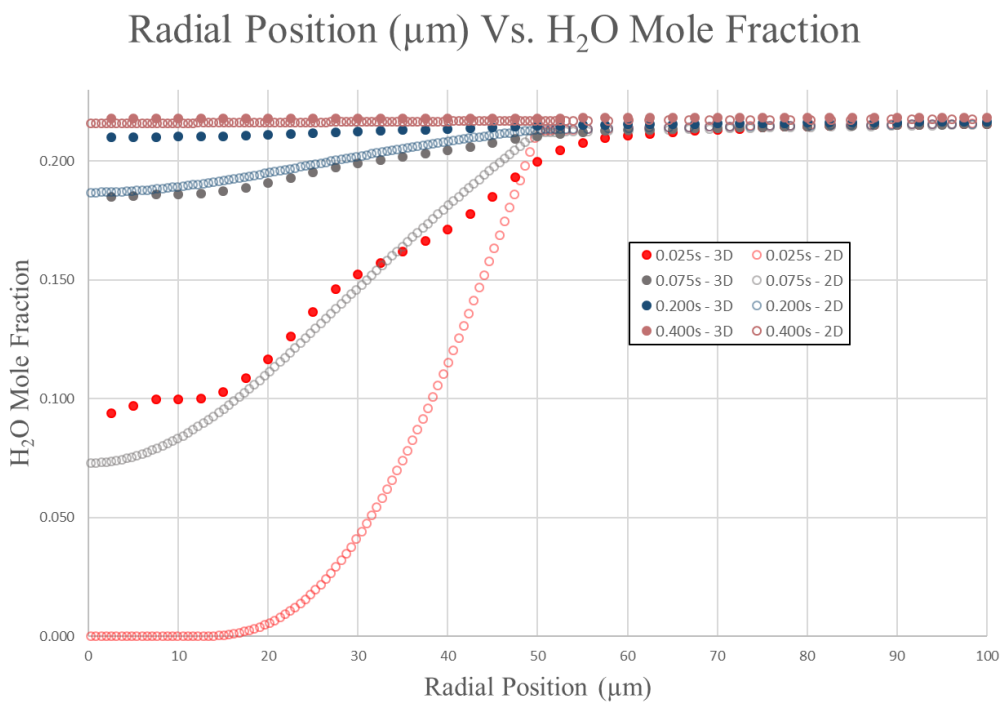

Figure 4-32. One-Dimensional Profile of H_2O Mole Fraction - Zoomed Fig. 4-31

Although the contour plots of H_2O were discussed in depth, the one-dimensional profiles offer a much more insight on the penetration of the reactant. From first glance, it is evident that the reactant is able to penetrate through the particle starting from the initial recorded time step for the resolved model but not in the unresolved model. Similar to the procedure used for H_2, the first resolved recorded profile is shown to be superimposed onto the unresolved in Figure 4-31 and 4-32 as a means of comparison and determining the relative progression between the two particles. The result is the resolved model's first profile would best fit between times 0.750s and 0.100s of the unresolved case showing that advanced penetration of the resolved model when compared to the unresolved model. The elevated amount of reactant penetration can be attributed to the resolution of the geometric features obtained from micro-CT.

To further explore the effects of the resolved geometric features, porous networks need to be discussed. Porous networks are geometric features where a continuous open volume is created from multiple or single pores within the porous matrix. Although it is nearly impossible with current computational resources to resolve the complete networks, the resolved geometry does contain partially resolved porous networks. Examples of partially resolved porous networks can be seen in Figure 3-6 where many abruptly ending macropores are visible. By resolving these macropores, the reactant has another mode of penetration that is not impeded or disrupted from reactant interaction with the unresolved pores. Not only does this enable more surface areas for gasification, but the resolved porous networks allow the reactant to bypass regions of the particle mass thus reducing the required penetration distance to reach the center of the particle. A shorter total penetration distance not only allows for the system to hasten the system to enter Zone I, the reactions will also be transported to volumes near vicinity of the macropore. If more reactants are within particle, the amount of diffusion will subsequently increase and begin to affect the on the outer most area reactants' transport within the particle. When accounting all of these factors, it is logical that the reactant resolved profile differs from the unresolved profile.

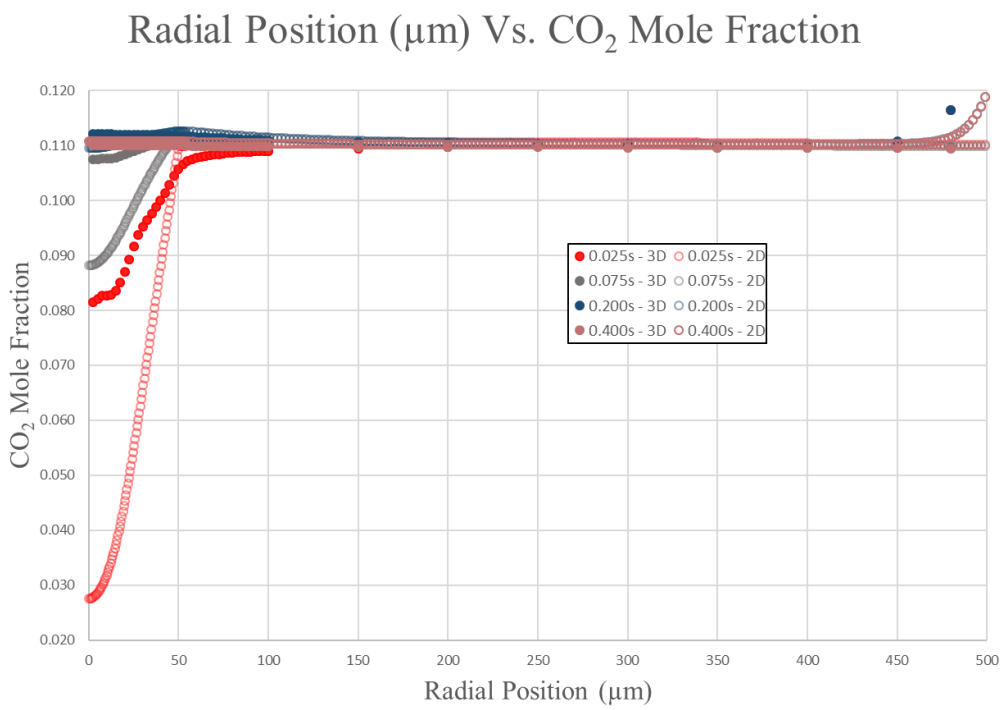

Figure 4-33. One-Dimensional Profile of CO_2 Mole Fraction

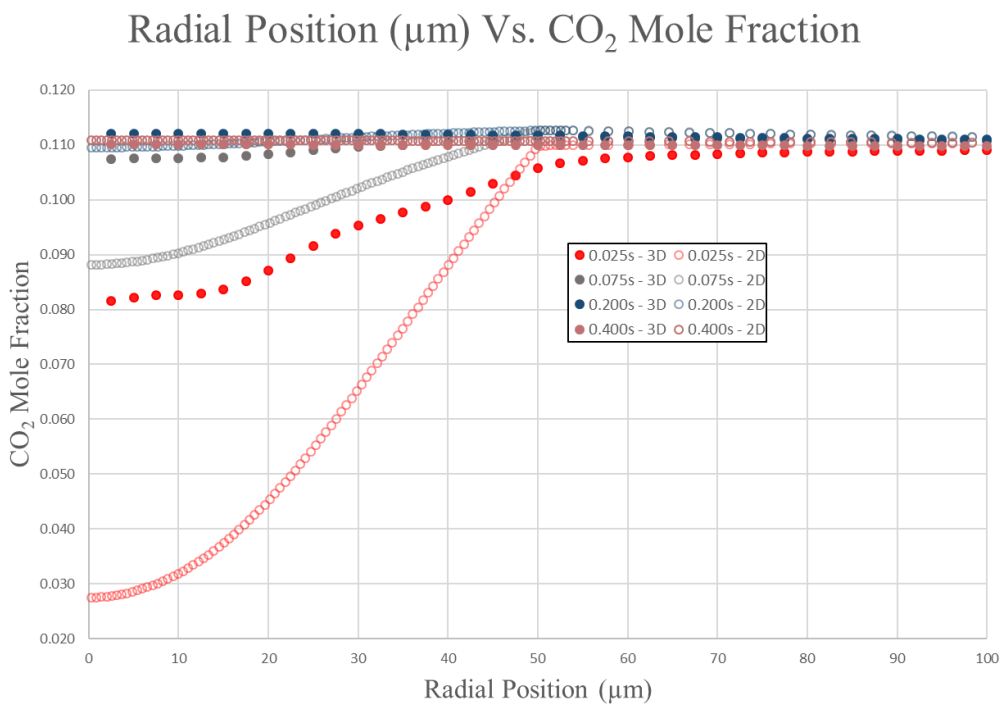

Figure 4-34. One-Dimensional Profile of CO_2 Mole Fraction - Zoomed Fig. 4-33

Unlike the counterpart reactant, H_2O, CO_2 resolved and unresolved profiles look more similar as there profiles have similar trends but the resolved profile is always slightly greater than the unresolved model at any given time. The reason why, as explained before, can be attributed to the relatively lower consumption rate of CO_2 compared to the H_2O. This allows CO_2 transport to overcome the consumption rate and expedite its transition into Zone I conditions for both the resolved and unresolved geometries. The same procedure used to gauge relative progression is implemented for the CO_2 profiles. For this species, the resolved profile at 0.025s would best fit within the unresolved profile between 0.050s and 0.075s. Although the geometric features still have an influence on CO_2, the effects are proven to be attenuated compared to other species at the initial timeframe as the interplay

between resolved geometric structure and reactions are reduced because of the relatively slower CO_2 reaction rate.

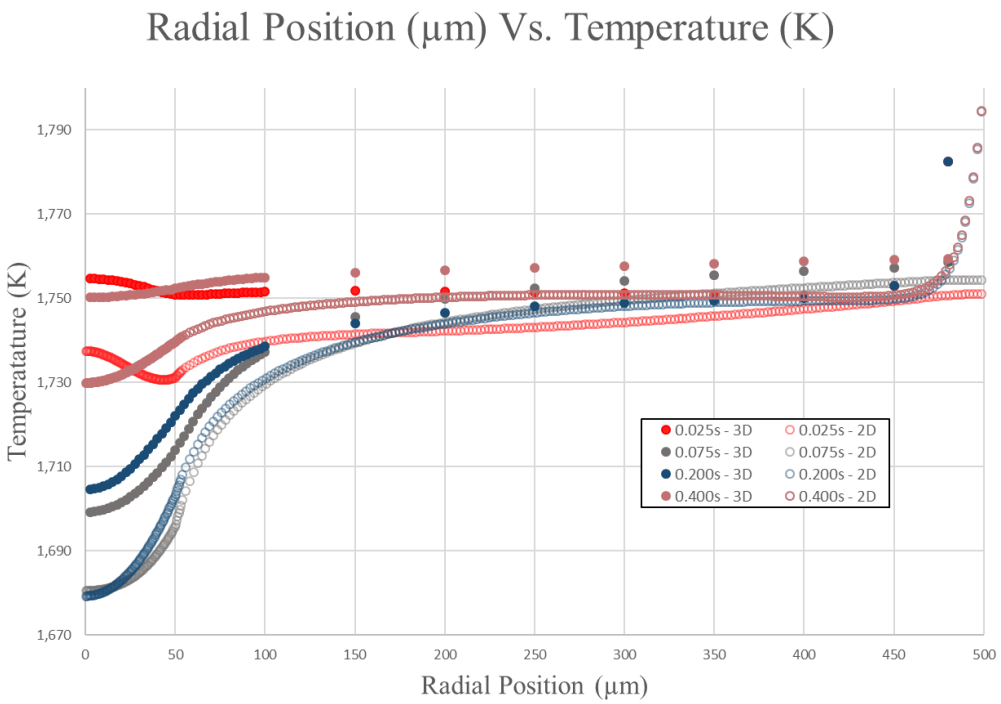

Figure 4-35. One-Dimensional Profile of Temperature

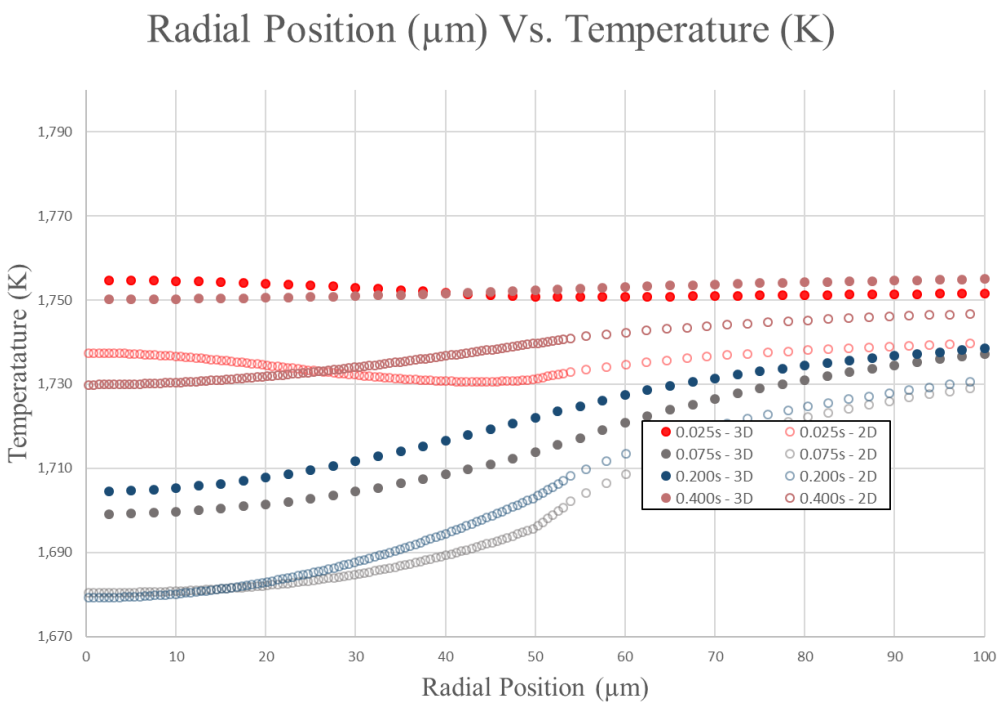

Figure 4-36. One-Dimensional Profile of Temperature - Zoomed Fig. 4-35

As previously mentioned, the gasification reactions are endothermic, which means as long as there is particle mass yet to be consumed, the temperature surrounding and within the particle will always be less than the temperature after the water-gas shift reactions have reached equilibrium. The ambient temperature also fluctuates to account for the amount of species produced or consumed from the resultant gasification reactions at that specific time. Both models indicate an overall trend where for the majority of the particle's residence time, the temperature profile's minimum is located at the center of the particle. The only times where this claim is inaccurate is near the end of the particle's life where the temperature become approximately the same as the surrounding temperature due to minimal gasification occurring. Also, this is not true at early times, due to the particle's highly transient adjustment to the prescribed boundary conditions.

The difference between the two models are emphasize when analyzing the profiles that display comparatively lower values. From this, it is evident that the unresolved temperature profiles from times 0.100s to 0.200s, the temperature profile remains somewhat constant with minor variance between the profiles. The determined resolved trend does not share these similarities as the lesser valued temperature profiles are easily differentiable and temperature's progression can be described as incrementally increasing. The resolved temperature progression at the lower end can be seen from the time frame, 0.075s to 0.150s, where from 0.075s to 0.100s, the temperature reaches its minimum temperature profile.

By comparing the magnitudes of both models' temperature profile, the resolved model is seen to operate at a higher temperature than the unresolved model at all recorded times. As stated in previous discussions and illustrated from the temperature profiles, the acceleration of the particle progression causes the unresolved model to lag behind the resolved model due to resolved geometric features having a significant impact on transport of reactants to active sites within the particle, especially at early times, 0s to 0.715s. The reactants' transport is intensified by permitting reactants to further penetrate into the particle via geometric features, such as porous networks and voids. By utilizing these paths, the reactants are able to bypass interaction with the outer particle volume and retain a significant portion of the thermal energy that would have been otherwise consumed by endothermic reactions. When the relatively high thermal energized reactants begin to interact with the inner regions of the particle, the gasification reactions cause these regions to decay at a rate somewhat similar to the outer particle regions. The faster rates rapidly then reduce the amount of surface area, which translates into less gasification but still

accessible by reactant with relatively high thermal energy. In contrast, the unresolved model has no additional pathways further into the particle. In order to reach penetrate into the inner regions of the particle, the reactants must first interact with the outer particle regions, which consequentially consumes the reactants' thermal energy while the majority of the inner region retain a majority of their surface area. This explains why the resolved model always operates at a higher temperature than the unresolved model.

It may be also noted that all profiles may demonstrate a sudden variable gradient near the furthest radial distance when compared to the fluid domain. This is attributed to the boundary condition (pressure outlet), which as described before, has the potential to act as either as a sink or a source that essentially *slightly* decreases or increases the variables' values at the boundary condition. This does not affect calculations and is a known property associated with the implementation of the boundary condition, "pressure outlet" and "reverse flow". Although not as evident from the contour plots but within the one-dimensional plots, the ambient environment (radial distance greater than 100 microns) does not retain the prescribed ambient values at the pressure outlet boundary condition. This feature is caused by the ambient environment being affected by the water-shift homogeneous reactions, which alters three influential consumption variables, H_2O, CO_2, and temperature. The water gas shift reactions cause an imbalance between the reactants causing for one reactant to increase at the cost of the other. In this specific case, H_2O is the consumed and CO_2 is the produced, which overall decreases the consumption rate due to the $C+H_2O$ reaction rate being naturally faster than the $C+CO_2$ reaction. This is reflected in the chemical kinetics of Tremel illustrated on Table 3.5.[10] Since the water gas shift favors

CO_2 production, water gas shift becomes more endothermic reducing the potential temperature energy that can affect consumption, thus impeding the consumption rate.

The method that was executed to gather the one-dimensional profiles of species and temperature in Figures 4-27 to 4-39, fails to provide accurate data in the three-dimensional model for variables quantifying particle decay. The method's inaccuracies are attributed to the fact that both the particle and fluid zones occupy the spherical shells, without a means to differentiate between them during the polar and azimuthal averaging. Without a method to area average solely the particle domain occupied areas, the outcome would become drastically skewed, due to inclusion of the fluid domain. To overcome this weakness, porosity and conversion are volume averaged within the simulation and recorded at every time step.

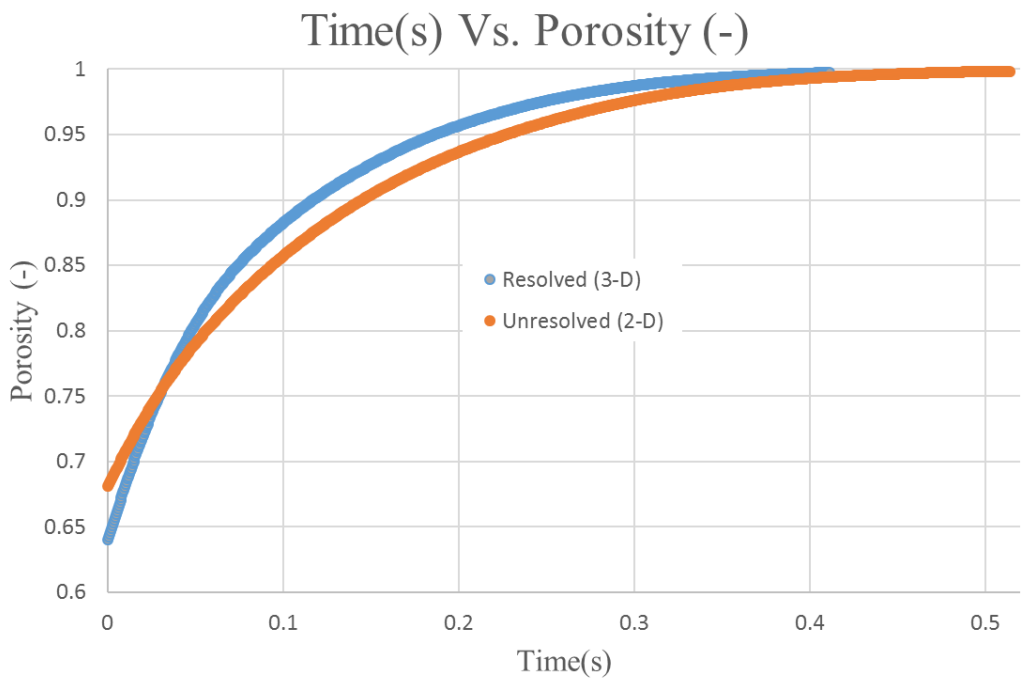

Figure 4-37. Transient Porosity Profile (2-D and 3-D)

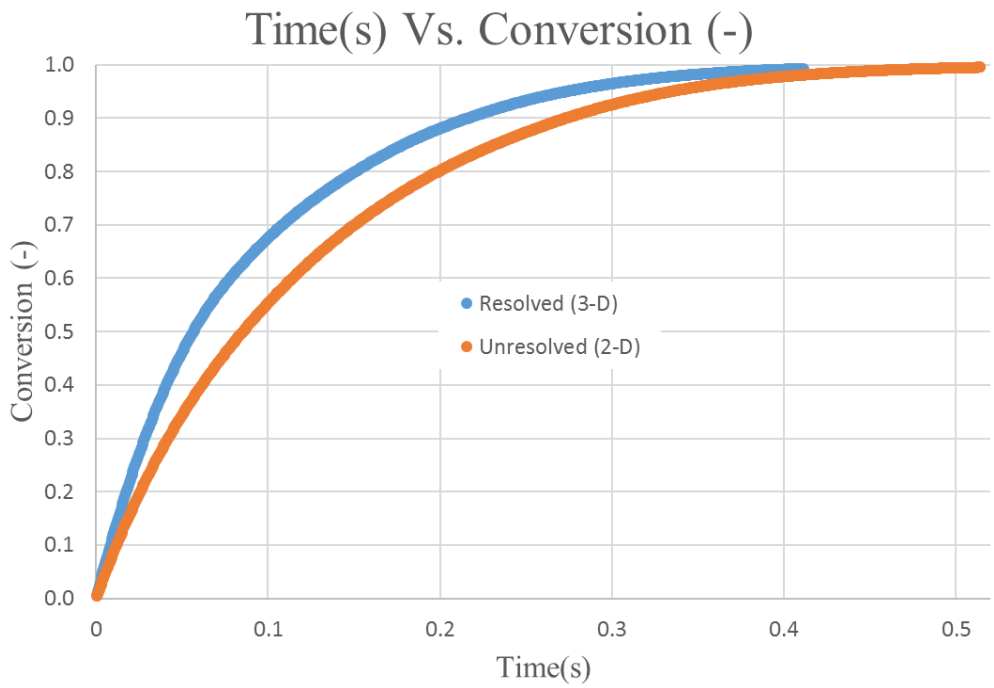

Figure 4-38. Transient Conversion Profile (2-D and 3-D)

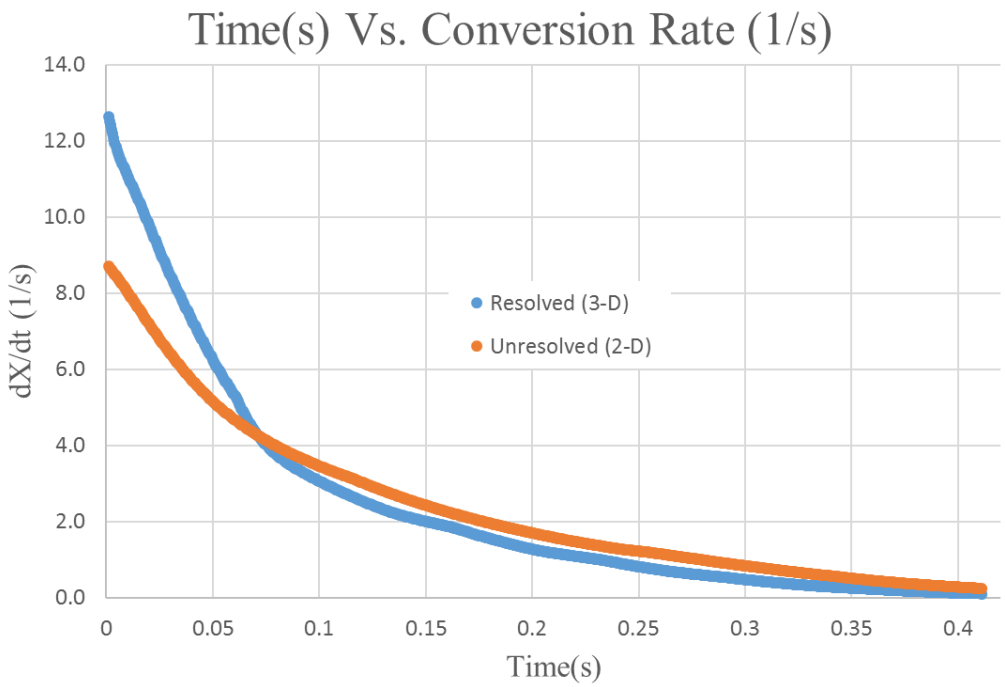

Figure 4-39. Transient Conversion Profile (2-D and 3-D)

Using the volume averaged porosity and conversion, the two models can be compared. It may be noted that conversion will act as the main mode of comparison as it is a non-dimensional variable, enabling a direct comparison between the two models. In addition, although both models' initial total porosity is the same proven from equivalent mass, total volume (sum of unresolved and resolved volumes), and size, Figure 4-37 only accounts for the volume average porosity in the unresolved regions. This explains why the initial porosity is different between the models. The effects of the geometric features are emphasized at the initial consumption timeframe (0s to 0.05s) where the resolved conversion rate is significantly greater than the unresolved conversion rate shown in Figure 4-39. It may be noted that the conversion rate was approximated using the first order central difference approximation. This phenomenon at this timeframe can be explained as the particle of both models is exposed to approximate similar environment and reactants. Since both models have yet to undergo significant decay and the resolved model has a comparatively greater amount of *available* surface area due to enhanced reactant transport, a greater conversion rate will result. After the initial burst of conversion, the conversion *difference* between the two models continually increases until approximately 0.0715s where the conversion difference maximum is approximately 0.1297. After this maximum, the difference between the two models begins to decrease until both particles are fully consumed. This described trend correlates with Figure 4-39 where the resolved rate is greater until 0.0715s where the unresolved rate becomes dominant. The cause of this decrease is due to the structure becoming the limiting conversion factor as the initial rapid particle decay in the resolved model not only increased the amount of conversion, but decreased the amount of surface area. Due to the greater percentage of remaining surface

area in the unresolved model, the difference begins to decrease, but the unresolved conversion is never greater than the conversion in the resolved model. Regardless of model, the conversion rate will eventually be limited by the decaying amount of surface area illustrated in Figure 4-38 after 0.2s where the both conversion rates are drastically diminished. Before reaching the maximum conversion difference, the conversion difference continually increases because the resolved structure increases the transport and the accessibility surface area to outpace the gasification occurring in the unresolved model at the given time.

The particle is considered to be completely consumed when the conversion reaches a value of 0.99. From this criterion, the unresolved and resolved models are fully converted at 0.4605s and 0.3890s respectively. The corresponding relative error between the two models' complete consumption was calculated to be approximately 18.38%. It is also emphasized that although the porosity of the regions between the voids in the 3-D model are adjusted to a lower initial value to make both models have the same total (measured) porosity, and same total mass, the 3-D unresolved porosity eventually becomes greater than the 2-D unresolved porosity. This reiterates the effect the geometric features on the particle's progression. Overall, from analyzing the particle decay via conversion, the error associated with implementation of the porous continuum assumption is shown to result in a relative error of 18.38% and high conversion difference at 0.050s to 0.200s for this specific particle.

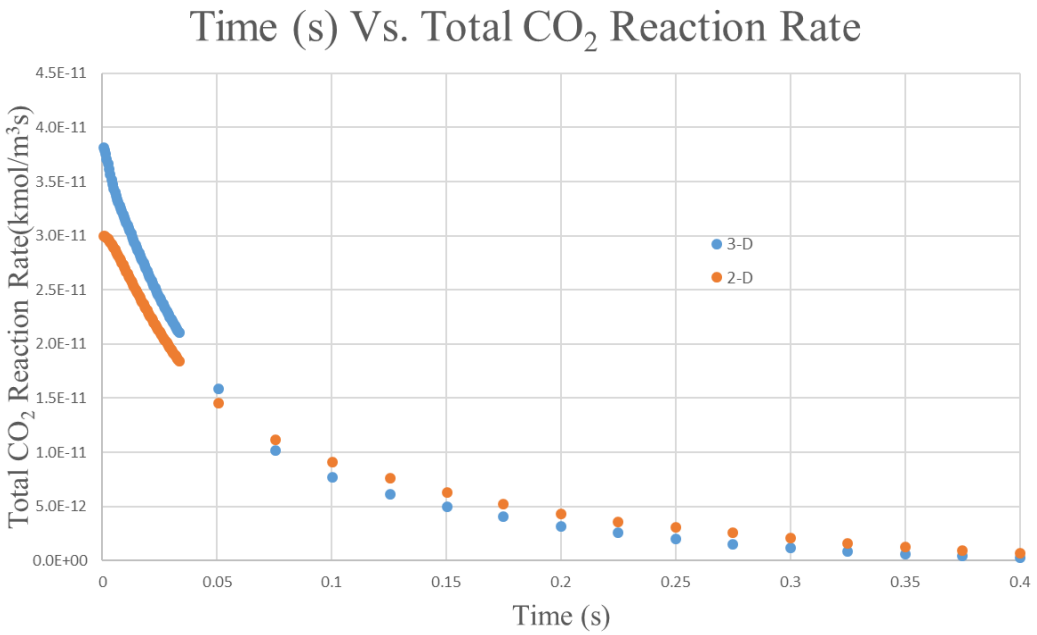

Figure 4-40. Particle Volume Integral of CO_2 Reaction Rate

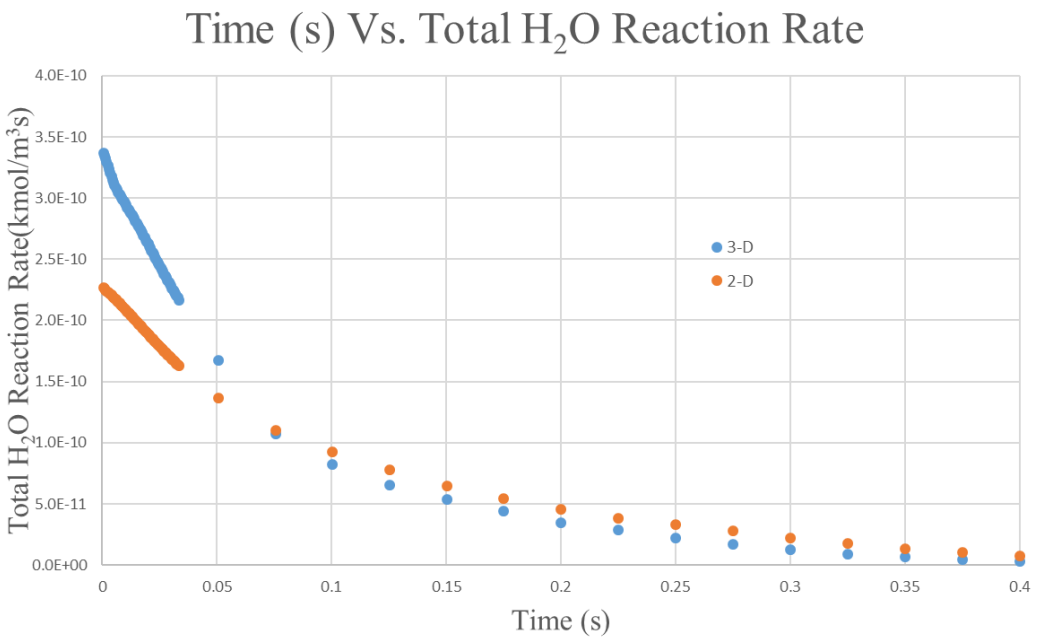

Figure 4-41. Particle Volume Integral of H_2O Reaction Rate

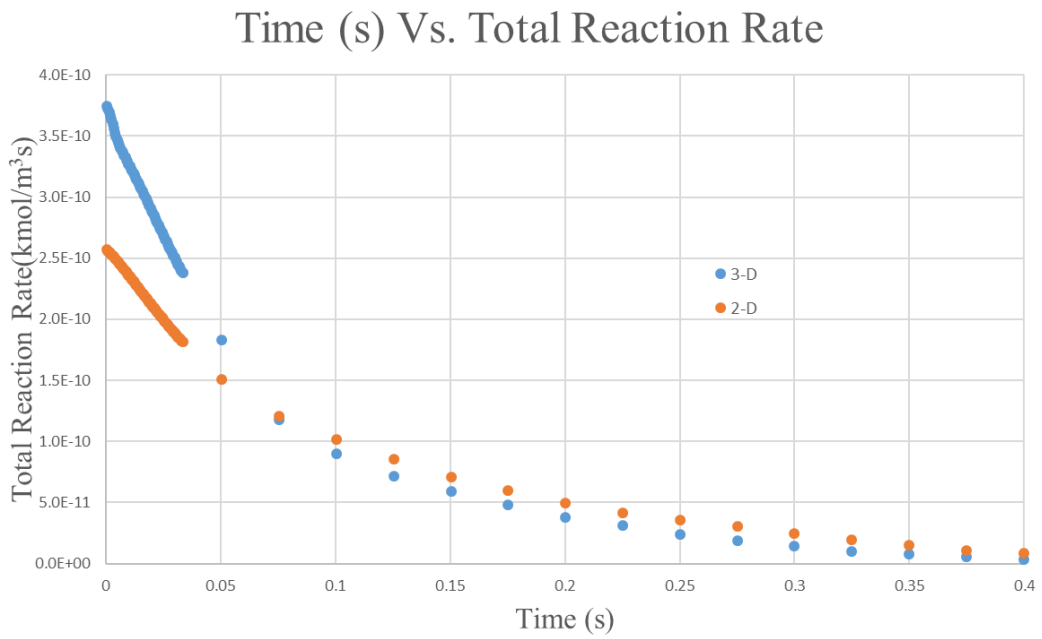

Figure 4-42. Particle Volume Integral of Both Reaction Rates

Although conversion by itself can provide significant insight on the difference between the models, it is also important to analyze the gasification reactions that consume the particle. To accomplish this, the particle's volume was integrated to obtain the total amount gasification reaction rates that occurred at a specified time. The individual total gasification rates are individually and then collectively plotted, shown in the figures above. It can be clearly seen that Figure 4-40 complies with the developed narrative that the reactant.CO_2, only experiences minor influences from geometric features which is indicative by both models' similar reaction rate values and profiles. This can be only explained by Zone I nature where both CO_2 profiles and contour plots previously display approximate constant profiles throughout the particle due to the lack of CO_2 consumption. The only noticeable period where there is a significant difference between the two is before the time where the maximum conversion difference occurs, approximately 0.0715s. At this

time, the geometric features would intensify the initial transport of CO_2 from the environment into the particle.

Similar to CO_2, both H_2O reaction rate profiles are approximate after the maximum conversion time, 0.0715s but show significant difference before 0.0715s shown in Figure 4-41. The difference beforehand can be again attributed to the geometric features that enhance the initial reactant transport into the particle, thus increasing the opportunities for the reactants to interact with the surface area. In Figure 4-42, both total reaction rates are summed and result in a similar profile and value as the H_2O total reaction rate in Figure 4-41. The high similarities between the two figures can be explained by H_2O simply being approximately one magnitude greater than the CO_2 thus H_2O governs the total profile with minor influences from CO_2. When analyzing the three figures above collectively, it is evident that the previously made statement, "the unresolved model lags behind the resolved model" has validity associated with it. This is evident in Figures 4-39 to 4-42 where the resolved model greatly outpaces and out progresses the unresolved model before 0.0715s. Afterwards, both models maintain similar profiles and values, which indicate approximate progression rate. This means the unresolved particle can never overcome the initial progression difference, thus explaining why the contour plots and one-dimensional plots exhibit some lagging behavior.

4.3 Effectiveness Factor

Although there is overwhelming evidence that reinforces the conclusion, complete implementation of the effective porous continuum assumptions results in significant inaccuracies, further analysis is required to support the claim. To strengthen the claim, a

previous discussed modeling method, effectiveness factor is calculated for each model at varying times. The effectiveness factor is calculated as the ratio between the volumes integrated reaction rates of the actual to the ideal case. The ideal reaction rate is calculated using the Tremel expressions in a custom field function using the simulation temperature and pressure profiles while assuming the reactant mole fraction is constant throughout the particle. Since the effectiveness factor is a metric to characterize the particle's zonal behavior and a value of one assumes complete penetration of reactant and indicates Zone I conditions, the ideal reactant mole fraction is determined to be maximum reactant mole fraction throughout all domains and times. Due to the inclusion and complexities of the water gas shift reactions in the surrounding environment, the maximum reactant mole fractions are not simply the prescribed values at the pressure outlet boundary condition. The maximum reactant mole fractions are determined from the maximum value from H_2O and CO_2 auto ranged animation files in addition to analysis of Figures 4-31 to Figure 4-34. The implemented mole fractions of H_2O and CO_2 were chosen to be 0.218 and 0.111 respectively. The resultant figures are shown below where the effectiveness factors of H_2O and CO_2 are separately and then collectively determined.

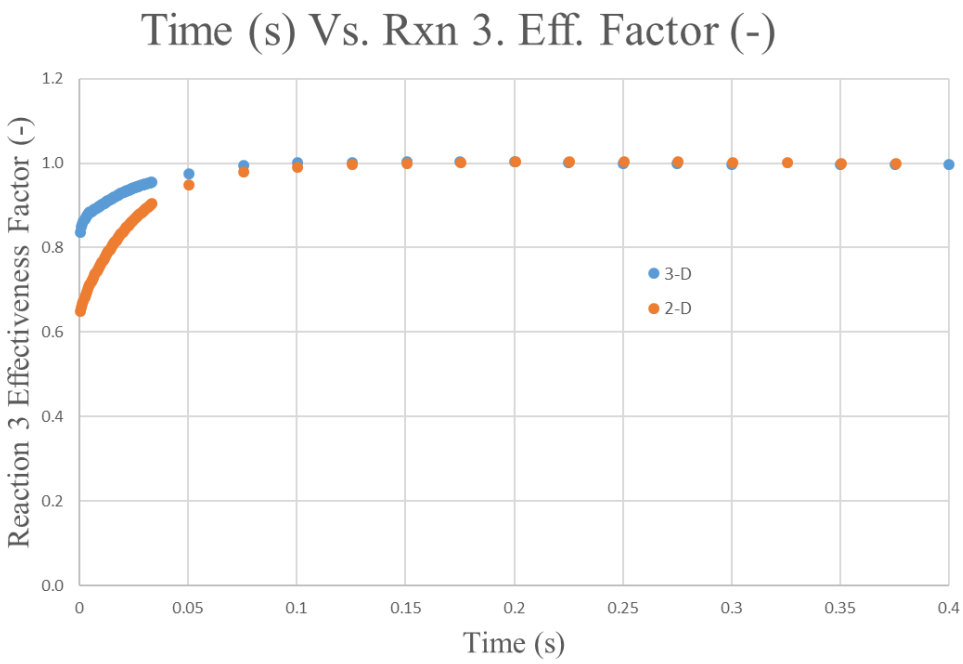

Figure 4-43. Effectiveness Factor – Reaction 1 (CO_2)

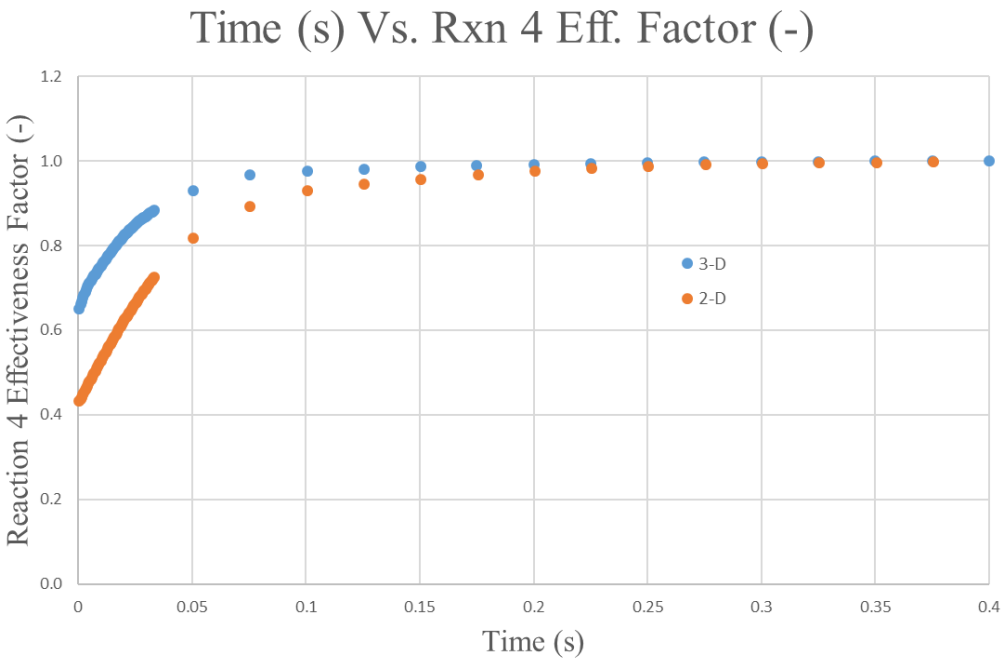

Figure 4-44. Effectiveness Factor – Reaction 2 (H_2O)

From an initial glance of the figures above, the effectiveness factor of the CO_2 reaction is greater than H_2O reaction at all times that do not hold a unity value. This conclusion complies with the current narrative developed from the CO_2 mole fraction, reaction, and diffusion coefficient contour plots and one-dimensional plot as CO_2 is proven in all cases to easily penetrate the particle when compared to H_2O. When comparing the two models in any of the two reactants, it is evident that the resolved model indicates that its earlier life period (0s to 0.1s) correlate to more Zone I characteristics rather than the Zone II from the higher effectiveness factor. An explanation of this cause is the accelerated conversion rate relative to the unresolved model causing for a greater particle decay that translates into further diminishing porous structural transports effects, primarily Knudsen diffusion, that promotes transport throughout the particle. This is cause is also coupled with the resolved geometry, that introduces additional loci for reactant to particle interaction. The new areas not only increase the accessibility to the surface area but as stated before, decreases the distance from external surface area to external surface area signifies a relatively lesser required penetration distance. Overall, these effects justify the initial great difference between both reaction effectiveness factors.

Another interesting aspect presented in Figures 4-43 and 4-44 is time where both the unresolved and resolved model completely functions under Zone I conditions denoted from an effectiveness factor value of unity. In the case of CO_2 reaction, both models reach an effectiveness factor of unity at roughly the same time at 0.1s. Even though the model geometries are different and can cause the stated effects, the CO_2 consumption rate is sufficiently low permitting the CO_2 penetration rate to overcome the consumption rate and reach Zone I conditions relatively rapidly with or without the inclusion of a resolved

geometry. Unlike the CO_2 reaction, H_2O consumption rate is adequately high to have a noteworthy impact on and impede H_2O penetration rate. The amount of disruption is also greatly nullified when coupled with the resolved geometry due to the greater accessibility to the same amount of surface area. This explains why the resolved model reaches unity at 0.125s compared to 0.175s of the unresolved model. Lastly, it may be noted that although the difference between the ideal and actual reaction rates is the reactant mole fraction, the model effectiveness factors difference is simply not the difference between the volume integrated reactant mole fractions. This is because the mole fraction is altered from the Tremel reaction order shown from Table 3.5.

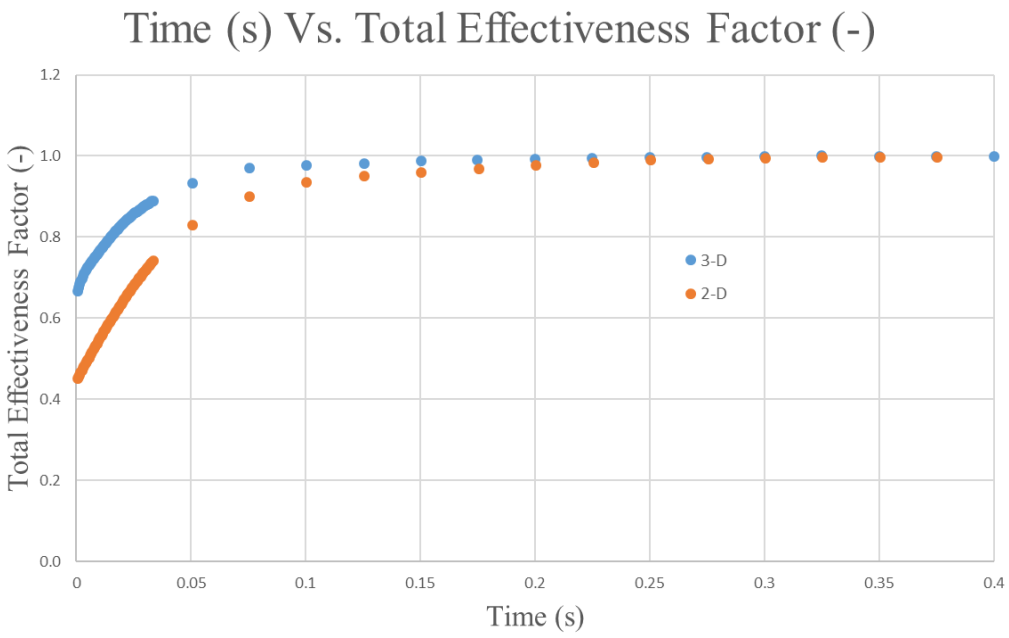

Figure 4-45. Effectiveness Factor – Total Reaction (CO_2 and H_2O)

From the Figure 4-45, it is evident that the total effectiveness factor (combining reaction 1 – CO_2 and reaction 2 – H_2O) shares the high similarities (e.g. trends and values) with the H_2O reaction effectiveness factor, Figure 4-41, throughout the particle lifespan.

This explained from previous discussion that emphasized the fact that H_2O gasification rate occurs at a considerably faster rate than its CO_2 reaction counterpart, apparent from the Tremel kinetics. Since the H_2O gasification reactions occur at more frequent rate compared to CO_2, approximately one magnitude greater at all times, H_2O governs the total effectiveness factor while CO_2 reaction is neglectable with minor influence. Overall, the trend that the overall effectiveness factor is concluding is the resolved geometry reaching complete Zone I characteristics at approximately time 0.125s while the unresolved geometry reaches the same characteristics at approximately time 0.175s supporting the narrative that the resolved geometry does enhance transport thus enhancing conversion properties.

Chapter 5. Conclusion

Typical gasification models implement the effective porous continuum assumption, a volume averaging approach that treats all geometric features as unresolved and sub-grid-scale. To question the current gasification narrative, two gasification CFD models were developed to answer the primary questions: “What are the inaccuracies associated with improper utilization of the effective porous continuum assumption due to length-scale constraint violation shown in Eq 1.1?” and “What effects do the resolved geometric features on char gasification have compared to a simple spherical representation of a char particle?”.

To investigate both questions, one model consists of an unresolved char particle, represented by a simple sphere that completely implements the effective porous continuum assumption, thus violating the length-scale constraint. Another model consists of a partially-resolved Illinois no. 6 char particle (obtained via micro-CT) with the assumption implemented solely in the unresolved microporous regions, thus satisfying the length-scale constraints. To isolate the effects on particle morphology, both models utilize identical boundary and initial conditions, leaving particle transport difference to be attributed to the resolved particle morphology. To further validate the comparison, physical properties, such as total volume, mass, porosity, and effective diameter are equivalent.

From a series of contour plots, one-dimensional plots, conversion plots, volume integrated gasification reaction rate plots, and effectiveness factor plots, the differences between the two models were determined. These plots indicate an enhanced reactant and product transport into and out of the particle, respectively. The enhanced reactant transport

and penetration is indicated by the higher reactant mole fractions within the 3-D resolved particle compared to the 2-D unresolved particle, especially at earlier gasification times. Enhanced transport is enabled by the resolved geometric features, which increases the accessibility of reactants to the inner particle surface area via macroscopic porous networks resulting in accelerated particle consumption. Although more endothermic gasification reactions occur within the 3-D particle, the 3-D temperature profile still remains greater than the 2-D model. This can be explained as the reactants that bypass interactions with the particle to penetrate further into the particle via alternative avenues retain a majority of their thermal or internal energy. In other words, convection is enhanced. Since this thermal and internal energy source remains approximately constant and the surface area wane as particle progression continues, the temperature within the particle remains higher and consequentially contributes to the accelerate consumption. The resolved effects are greatest in the initial time period from 0s to 0.0715s where the 3-D conversion rate is greater than the 2-D conversion rate. After 0.0715s, the 2-D conversion rate is greater but is unable to overcome the initial accelerated rate of the 3-D model. The 2-D and 3-D models fully converted at 0.3890s and 0.4605s, respectively resulting in a relative error of 18.38% for conversion using the effective continuum assumption. Lastly, the individual and combined ex-post-facto effectiveness factors support the above narrative, as the 3-D model indicates Zone I properties at an earlier time allowing all surface area to be fully utilized, thus accelerating the particle consumption.

Chapter 6. Future Work

The current model is only applicable to the study of entrained flow gasification of char particles. The model can be further expanded by including intricacies such as combustion behaviors or inclusion of oxygen. Therefore, much of the required significant modifications pertain to the majority of UDFs rather than the Fluent set-up. The developed model can also be expanded into the renewable energy field, more specifically the study of biochar gasification, which is similar to coal char, although biochar contains more large geometric features. Lastly, the model can be further refined via the implementation of a higher resolution micro-CT scanner, which essentially increases the quality of the particle and its features. As of now, collaboration with the University of Wisconsin – Milwaukee Bioengineering Imaging and Testing Lab is being finalized to utilize their micro-CT scanner, capable of reaching 1.9-micron spatial resolution, which can greatly aid in imaging voids Marquette's micro-CT cannot capture.

Even though the resolved particle model has given significant insight on its effects, the developed model lacks statistical proof that resolving the large geometric features affects the conversion. To obtain the necessary statistical evidence, the process described from reconstructing and simulating many other Illinois no. 6 char particle must be repeated. Once a sufficient number of particles has been simulated and their results processed, a statistical definitive statement can be made. Afterwards, the resolved porous effects can be then quantified and attempts can be made to include their impact in sub-models of individual particles in reactor-scale CFD simulations, to improve their accuracy without significantly increasing computational expense.

Bibliography

[1] A. G. Dixon, J. Boudreau, A. Rocheleau, A. Troupel, M. E. Taskin, M. Nijemeisland and E. H. Stitt, "Flow, transport, and reaction interactions in shaped cylindrical particles for steam methane reforming," *Industrial and Engineering Chemistry Research,* vol. 51, pp. 15839-15854, 2012.

[2] A. G. Dixon, M. E. Taskin, M. Nijemeisland and E. H. Stitt, "CFD Method To Couple Three-Dimensional Transport and Reaction inside Catalyst Particles to the Fixed Bed Flow Field," *Industrial & Engineering Chemistry Research,* vol. 49, no. 19, pp. 9012-9025, 2010.

[3] A. Luckos and A. Koekemoer, "On the sphericity of coal and char particles," *South African Journal of Chemical Engineering,* vol. 19, no. 3, pp. 62-71, 2014.

[4] ANSYS INC., "ANSYS 17.1 Capabilities," 2016. [Online]. Available: http://resource.ansys.com/staticassets/ANSYS/staticassets/resourcelibrary/brochure/ansys-capabilities-17.1.pdf. [Accessed 23 2 2017].

[5] ANSYS INC., *ANSYS Fluent Customization Manual,* 2015.

[6] ANSYS INC., *ANSYS Fluent Theory Guide,* 2012.

[7] ANSYS INC., *ANSYS Fluent User's Guide,* 2011.

[8] ANSYS INC., *Meshing Help,* 2009.

[9] A. Richter, P. Nikrityuk and B. Meyer, "Three-dimensional calculation of a chemically reacting porous particle moving in a hot O 2 / CO 2 atmosphere," *International Journal of Heat and Mass Transfer,* vol. 83, pp. 244-258, 2015.

[10] A. Tremel and H. Spliethoff, "Gasification kinetics during entrained flow gasification – Part II: Intrinsic char reaction rate and surface area development," *Fuel,* vol. 107, pp. 653-661, 2013.

[11] A. Zoulalian, R. Bounaceur and A. Dufour, "Kinetic modelling of char gasification by accounting for the evolution of the reactive surface area," *Chemical Engineering Science,* vol. 138, pp. 281-290, 2015.

[12] B. R. Bird and W. E. Stewart, Transport Phenomena, New York: J. Wiley, 2007.

[13] Brucker microCT, [Online]. Available: http://bruker-microct.com/company/methods.htm. [Accessed 3 5 2017].

[14] C. Botero, R. P. Field, H. J. Herzog and G. A. F. , "Impact of finite-rate kinetics on carbon conversion in high-pressure, single-stage entrained flow gasifier with coal-CO2 slurry feed," *Applied Energy,* vol. 104, pp. 408-417, 2013.

[15] C. Feng and W. E. Stewart, "Practical Models for Isothermal Diffusion," *Industrial & engineering Chemistry Fundamentals,* vol. 12, no. 2, pp. 143-147, 1973.

[16] C. O. Karacan and B. Mark, "Effects of Steam Injection on Pore Structure and Distribution in Coke Samples Produced by Delayed Coking," *Fuel,* vol. 82, no. 2, pp. 909-917, 2003.

[17] "Coal and Climate Change," World Coal Assoication, [Online]. Available: http://www.worldcoal.org/file_validate.php?file=Coal%20and%20climate%20change.pdf. [Accessed 9 2 2017].

[18] D. H. Maylotte, C. L. Spiro, P. G. Kosky and E. J. Lamby, "X-Ray Computed Tomograhy Of Coal: Frinal Report," General Electric Corporation Research & Development, Schectady, 1986.

[19] D. L. Smoot and D. T. Pratt, Pulverized-Coal Combustion and Gasification: Theory and Applications for Continuois Flow Processes, New York: Plenum Press, 1979.

[20] D. Safronov, M. Kestel, P. A. Nikrityuk and B. Meyer, "Particle resolved simulations of carbon oxidaiton in laminar flow," *Can. J. Chem. Eng.,* vol. 92, pp. 1669-1686, 2014.

[21] E. Johnson, U.S. Energy Information Adminstration, [Online]. Available: www.eia.gov. [Accessed 2017 9 2].

[22] E. M. Hodge, D. G. Roberts, D. J. Harris and J. F. Stubington, "The Significance of Char Morphology to the Analysis of High-Temperature Char−CO2 Reaction Rates," *Energy & Fuels,* vol. 24, no. 1, pp. 100-107, 2010.

[23] "Entrained Flow Gasifier," U.S. Department of Energy, [Online]. Available: https://www.netl.doe.gov/research/coal/energy-systems/gasification/gasifipedia/entrainedflow. [Accessed 10 7 2017].

[24] F. Y. Wang and S. K. Bhatia, "A Generalised Dynamic Model for Char Particle Gasification with Structure Evolution and Peripheral Fragmentation," *Chemical Engineering Science,* vol. 2001, no. 56, pp. 3683-3697, 2001.

[25] "+FE Module Technical Data Sheet," [Online]. Available: https://www.simpleware.com/files/techdata/techData_+FE.pdf. [Accessed 24 2 2017].

[26] G. Froment and B. K.B., *Chemical Reactor Analysis and Design,* New York: Wiley, 1990.

[27] G. George, "A Random Capillary Model with Application to Char Gasification at Chemically Controlled Rates," *AIChE journal,* vol. 26, no. 4, pp. 577-585, 1980.

[28] G. Liu, H. Rezaei, J. Lucas, D. .. Harries and T. Wall, "Modelling of a Pressurized Entrained Flow Coal Gasifier: The Effect of Reaction Kinetics and Char Structure," *Fuel,* vol. 79, pp. 1767-1779, 2000.

[29] H. Fatehi and X.-S. Bai, "Effect of Pore Size on the Gasification of Biomass Char," *Energy Procedia,* vol. 75, no. 1, pp. 779-785, 2015.

[30] H. Li, M. Ye and Z. Liu, "A Multi-Region Model For Reaction-DiffusionProcess Within A Porous Catayst Pellet," *Chemical engineering Science,* vol. 147, pp. 1-12, 2016.

[31] H. S. Carem and N. R. Amundson, "Diffusion and Reaction in a Stagnant Boundary Layer about a Carbon Particle," *Industrial & Engineering Chemistry Fundamentals,* vol. 16, no. 2, pp. 171-181, 1977.

[32] I. Smith and R. Tyler, "Internal burning of pulverized semi-anthracite: the relation between particle structure and reactivity," *Fuel,* vol. 51, no. 4, pp. 312-321, 1972.

[33] I. Smith, "THE COMBUSTION RATES OF COAL CHARS: A REVIEW," *Symposium (International) on Combustion,* pp. 1045-1065, 1982.

[34] J. Hong, *Modeling Char Oxidation As A Function of Pressure Using An Intrinsic Languir Rate Equation,* 2000.

[35] J. Hong, W. C. Hecker and T. H. Fletcher, "Improving the Accuracy of Predicting Effectiveness Factors for mth Order and Langmuir Rate Equations in Spherical Coordinates," *Energy and Fuels,* vol. 14, pp. 663-670, 2000.

[36] J. Rouquerol, D. Avnir, C. fairbridge, D. Everett, J. Hayes, N. Pernicone and J. S. K. U. K. Ransay, "Recommendations for the Characterization of Porous Solids," *Pure and Applied Chemistry,* vol. 66, no. 8, pp. 1739-1758, 1994

[37] J. Yu, J. A. Locua and T. F. Wall, "Formation of the structure of chars during devolatilization of," *Progress in Energy and Combustion Science,* vol. 33, no. 2, pp. 135-170, 2007.

[38] K. B. Bischoff, "Effectiveness Factors for General Reaction Rate Forms," *AIChE Journal,* vol. 11, no. 2, pp. 351-355, 1965.

[39] K. L. Smith, D. L. Smoot, T. H. Fletcher and R. J. Pugmire, The Structure and Reaction Processes of Coal, New York: Plenum Press, 1994.

[40] K. Zygourakis, "Effect of Pyrolysis Conditions on Macropore Structure of Coal-Derived Chars," *Energy & Fuel,* vol. 7, no. 1, pp. 33-41, 1993.

[41] L. D. Schmidt, The Engineering Of Chemical Reactions, New York: Oxford University Press, 2005.

[42] L.-S. Fan and C. Zhu, "Size and Properties of Particles," in *Principles of Gas-Solid Flows,* Cambridge, Cambridge University Press, 1998, pp. 3-45.

[43] M. E. D. R. J. Davis, "Effects of Transport Limitations on Rate of Solid-Catalyzed Reactions," in *Fundamentals of Chemical Reaction Engineering,* New York, McGraw-hill, 2003, pp. 184-239.

[44] M. Sahimi, G. R. Gavalas and T. T. Tsotsis, "Statistical and Continuum Models of Fluid-Solid Reactions In Porous Media," *Chemical Engineering Science,* vol. 45, no. 6, pp. 1443-1502, 1990.

[45] Marquette University, [Online]. Available: http://www.eng.mu.edu/medicalimaging/micro-ct.html. [Accessed 2017 26 2].

[46] [Online]. Available: http://energy.kth.se/compedu/webcompedu/S4_Combustion/B10_Thermochemical_Conversion/C1_Introduction_to_Gasification/55_6_Gasifier_efficiency.htm. [Accessed 2017 21 3].

[47] Q. Xu, S. Pang and T. Levi, "Reaction kinetics and producer gas compositions of steam gasification of coal and biomass blend chars, part 2: Mathematical modelling and model validation," *Chemical Engineering Science,* vol. 66, no. 10, pp. 2232-2240, 2011.

[48] R. C. Reid, J. M. Prausnitz and B. E. Poling, The Properties of Gases & Liquids Fourth Edition, Boston: McGraw-Hill, 1987.

[49] R. C. Shurtz and T. H. Fletcher, "Coal Char-CO2 Gasification Measurements and Modeling in a Pressurized Flat-Flame Burner," *Energy Fuels,* vol. 27, no. 6, pp. 3022-3038, 2013.

[50] R. H. Hurt and J. M. Calo, "Semi-Global Intrinsic Kinetics for Char Combustion Modeling," *Combustion and Flame,* vol. 125, no. 3, pp. 1139-149, 2001.

[51] R. Hurt, D. Dudek, J. Longwell and A. Sarofim, "The phenomenon of gasification-induced carbon densification and its influence on pore structure," *Carbon,* vol. 26, no. 4, pp. 433-449, 1988.

[52] R. J. C. M. E. G. P. Kee, Chemical Reaction Flow Theory & Practive, Hoboken, NJ: Wiley-Interscience, 2003.

[53] R. Sahu, R. C. Flagan and G. R. Gavalas, "Discrete Simulation of Cenospheric Coal-Char Combustion," *Combustion and Flame,* vol. 77, no. 3-4, pp. 337-346, 1989.

[54] S. L. Singer and A. F. Ghoniem, "Comprehensive gasification modeling of char particles with multi-modal pore structures," *Combustion and Flame,* vol. 160, no. 1, pp. 120-137, 2013.

[55] S. LTD., *Reference Guide,* 2014.

[56] S. R. Turns, An Introduction to Combustion: Concepts and Applications, Boston: McGraw-Hill, 2000.

[57] S. S., *Gasification and Combustion Modeling for Porous Char Particles,* 2012.

[58] S. Sotirchos and N. R. Amundson, "Dynamic Behavior of a Porous Char Particle Burning in an Oxygen-Containing Environment. Part I. Constant Particle Radius," *AIChE Journal,* vol. 30, no. 4, pp. 537-549, 1984.

[59] T. P. Coffee and J. M. Heimerl, "Transport Algorithms for Premixed , Laminar Steady-State Flames," *Combustion and Flame,* vol. 289, no. 43, pp. 273-289, 1981.

[60] Y. Cai and K. Zygourakis, "A Multiscale Transient Model for Combustion of Highly Porous Chars," *Ind. Eng. Chem. Res.*, vol. 42, pp. 2746-2755, 2003.

[61] Simpleware, *Reference Guide,* 2007.

[62] Simpleware, *Tutorial Guide,* 2002.

Appendix A. Reaction Rate UDF

```
#include "udf.h"
/*----------------------------------------*/
/*
Author: GREG FONG
Last Updated 4/30/2017
Name:Surface Reaction Rate UDF
Aspects that need to be changed:
-In specific surface area (m^2/g) -> 480.0
0.012 -> Mc/rho_p,o change if values change
(1-X) -> in terms of porosity, C_UDSI
*/
/*----------------------------------------*/

/* Universal constants kJ/mol/K*/
#define Ru 0.008314

/* Molecular Weight */
#define MW_CO 28.01055
#define MW_H2 2.01594
#define MW_H2O 18.01534
#define MW_CO2 44.00995

/* Pre-exponential Factors - Tramel*/
#define K_CO2_A 7500
#define K_H2O_A 144800
/* Activation Energy - Tramel*/
#define K_CO2_E 200
#define K_H2O_E 212

DEFINE_SR_RATE(poro_rxn_rate,c,t,r,Mw,yi,rr)
{
/* Reaction Rate */
    real r3, r4;
/* Temperature */
    real Temp;
/* Position Criteria */
    real x[ND_ND], xpos, ypos, zpos;
/* store position in array x*/
    real S;
/* Molar Fraction */
    real X_CO, X_H2, X_H2O, X_CO2;
/* Partial Pressures */
    real P;
/* Reaction Rates - top k */
    real K_H2O, K_CO2;

    /* Defining Positions */
C_CENTROID(x,c,t);
xpos = x[0];
ypos = x[1];
zpos = x[2];



/*  Molar Fraction */
    X_H2 = (C_YI(c,t,0)/MW_H2)/((C_YI(c,t,3)/MW_CO)+(C_YI(c,t,0)/MW_H2)+(C_YI(c,t,1)/MW_H2O)+(C_YI(c,t,2)/MW_CO2));
    X_H2O = (C_YI(c,t,1)/MW_H2O)/((C_YI(c,t,3)/MW_CO)+(C_YI(c,t,0)/MW_H2)+(C_YI(c,t,1)/MW_H2O)+(C_YI(c,t,2)/MW_CO2));
    X_CO2 = (C_YI(c,t,2)/MW_CO2)/((C_YI(c,t,3)/MW_CO)+(C_YI(c,t,0)/MW_H2)+(C_YI(c,t,1)/MW_H2O)+(C_YI(c,t,2)/MW_CO2));
    X_CO = (C_YI(c,t,3)/MW_CO)/((C_YI(c,t,3)/MW_CO)+(C_YI(c,t,0)/MW_H2)+(C_YI(c,t,1)/MW_H2O)+(C_YI(c,t,2)/MW_CO2));

P = (2000000 + C_P(c,t))/1000000; /* Operating Pressure - MPa */
Temp = C_T(c,t);
S = 480.0*(3.125-(3.125*(C_UDSI(c,t,0)))); /* Specific surface area */

/* Reaction Rates */
K_H2O = (K_H2O_A*0.5725*pow(P*X_H2O,0.41)*exp((-1)*K_H2O_E/(Ru*C_T(c,t))));
K_CO2 = (K_CO2_A*0.5725*pow(P*X_CO2,0.41)*exp((-1)*K_CO2_E/(Ru*C_T(c,t))));


if(STREQ(r->name, "reaction-3"))
{
    r3 = (K_CO2*S/(12.0/672.0)); /* 12.0/672.0 is from M_c (Molecular weight of carbon) /rho_p,o (Initial density of particle) */
    *rr = r3;
}

else if(STREQ(r->name, "reaction-4"))
{
    r4 = (K_H2O*S/(12.0/672.0)); /* 2.0/672.0 is from M_c (Molecular weight of carbon) /rho_p,o (Initial density of particle) */
    *rr = r4;
}
}
```

Appendix B. UDS Source UDF

```
#include "udf.h"

/*-----------------------------------------*/
/*
Author: GREG FONG
Last Updated 4/30/2017
Name:Source C_UDSI UDF
Aspects that need to be changed:
- source equal term
(1-C_UDSI - Porosity)
- Specific surface area (m^2/g)
(1-X) expressed X in terms of porosity/C_UDSI
*/
/*-----------------------------------------*/

    real v;
    real ds;

/* Define which user-defined scalars to use. */
/* constants */
/* Species Number - Correlate With Listing */
/*---------CHANGE IF CHANGE ORDER---------*/
/* Universal constants kJ/mol/K*/
#define Ru 0.008314

/* Molecular Weight */
#define MW_CO 28.01055
#define MW_H2 2.01594
#define MW_H2O 18.01534
#define MW_CO2 44.00995

/* Pre-exponential Factors - Tremal */
#define K_CO2_A 7500
#define K_H2O_A 144800
/* Activation Energy -  Tremal*/
#define K_CO2_E 200
#define K_H2O_E 212

DEFINE_SOURCE(source1,c,t,ds,eqn)
{
/* Temperature */
    real Temp;
/* store position in array x*/
    real S;
/* Molar Fraction */
    real X_CO, X_H2, X_H2O, X_CO2;
/* Partial Pressures */
    real P_CO, P_H2, P_H2O, P_CO2, P;
/* Reaction Rates - bottom kappa */
    real Ka_CO, Ka_H2, Ka_H2O, Ka_CO2;
/* Reaction Rates - top k */
    real K_H2O, K_CO2;


Temp = C_T(c,t);

/*  Molar Fraction */
    X_H2 = (C_YI(c,t,0)/MW_H2)/((C_YI(c,t,3)/MW_CO)+(C_YI(c,t,0)/MW_H2)+(C_YI(c,t,1)/MW_H2O)+(C_YI(c,t,2)/MW_CO2));
    X_H2O = (C_YI(c,t,1)/MW_H2O)/((C_YI(c,t,3)/MW_CO)+(C_YI(c,t,0)/MW_H2)+(C_YI(c,t,1)/MW_H2O)+(C_YI(c,t,2)/MW_CO2));
    X_CO2 = (C_YI(c,t,2)/MW_CO2)/((C_YI(c,t,3)/MW_CO)+(C_YI(c,t,0)/MW_H2)+(C_YI(c,t,1)/MW_H2O)+(C_YI(c,t,2)/MW_CO2));
    X_CO = (C_YI(c,t,3)/MW_CO)/((C_YI(c,t,3)/MW_CO)+(C_YI(c,t,0)/MW_H2)+(C_YI(c,t,1)/MW_H2O)+(C_YI(c,t,2)/MW_CO2));

P = (2000000 + C_P(c,t))/1000000;   /* Operating Pressure (MPa) */
/* CHANGE IF INITIAL POROSITY CHANGES (INT - INT*C_UDSI) */
S = 480.0*(3.125-(3.125*(C_UDSI(c,t,0)))); /* Specific surface area */

/*Reaction Rates - Tremal*/
K_H2O = (K_H2O_A*0.5725*pow(P*X_H2O,0.41)*exp((-1)*K_H2O_E/(Ru*C_T(c,t))));
K_CO2 = (K_CO2_A*0.5725*pow(P*X_CO2,0.41)*exp((-1)*K_CO2_E/(Ru*C_T(c,t))));


    real physical_dt, phi_old, sum, Rxn4, Rxn7, source;
        Rxn4 = K_CO2;
        Rxn7 = K_H2O;
        sum = Rxn4 + Rxn7;
    source =  sum*S*0.32; /* 0.32 is from 1 - e_o - CHANGE IF INITIAL POROSITY CHANGES (1-C_UDSI) */
    dS[eqn] = 0.0;
    return source;
}
```

Appendix C. Diffusion Coefficient UDF

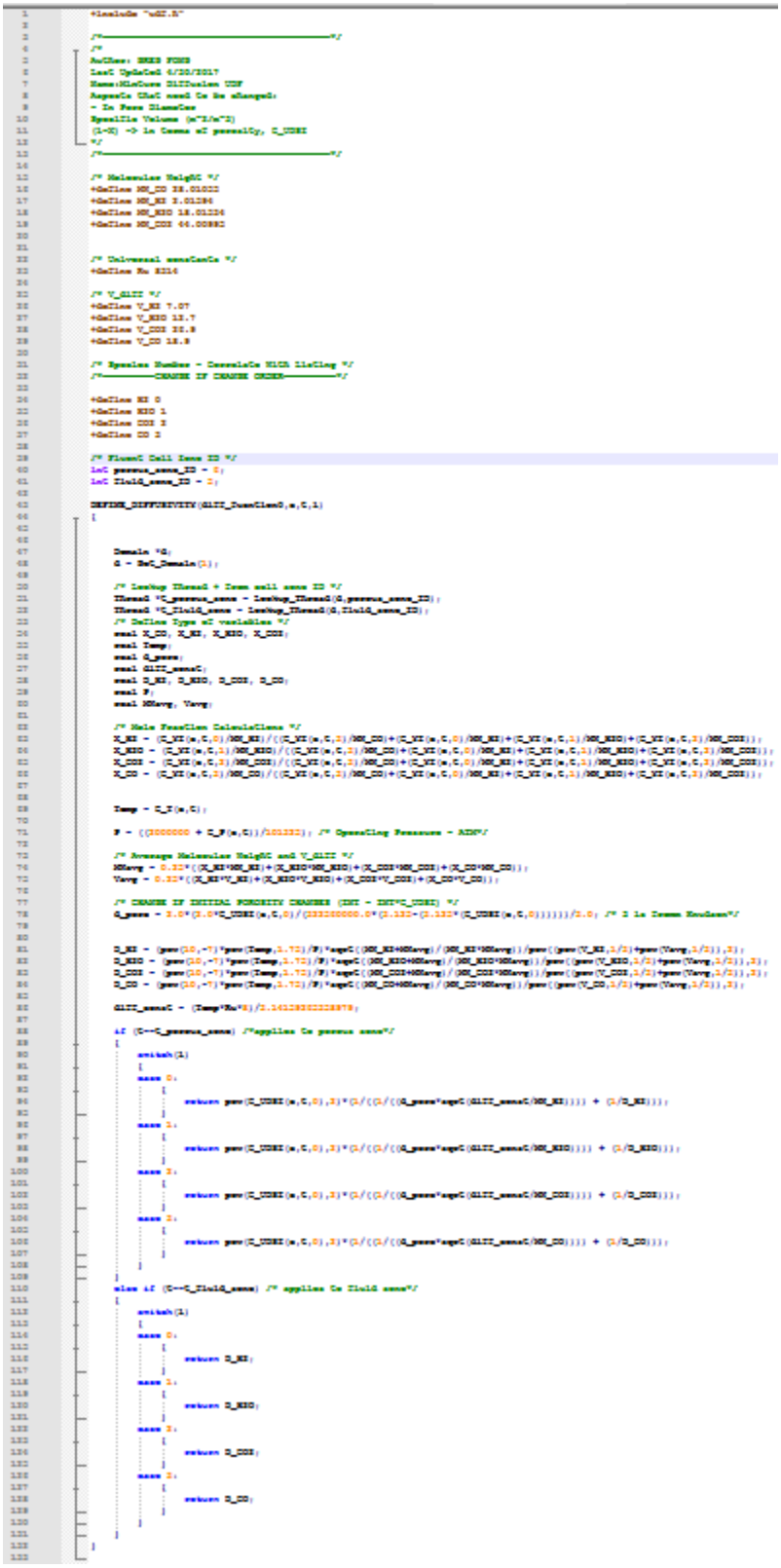

```
#include "udf.h"

/*------------------------------------------*/
/*
Author: ERKE FONE
Last UpdateOn: 6/20/2017
Name:MixCure DiffusionUDF
AspenCo ChaC needS Co Be changed:
- In Fuse ClassCas
SpeciFic Volume (m^3/m^3)
(1-X) -> In Cosma mI porosity, C_UDSI
*/
/*------------------------------------------*/

/* Molecular MeigHC */
#define MW_CO 28.01022
#define MW_H2 2.01184
#define MW_H2O 18.01234
#define MW_CO2 44.00982


/* Universal ansaCasCo */
#define Ru 8314

/* V_DIFF */
#define V_H2 7.07
#define V_H2O 12.7
#define V_CO2 26.9
#define V_CO 18.9

/* Species Number - CasculaCe With ilaCing */
/*----------CHANGE IF CHANGE ORDER----------*/

#define H2 0
#define H2O 1
#define CO2 2
#define CO 3

/* FluenC Cell Zone ID */
int porous_zone_ID = 5;
int fluid_zone_ID = 2;

DEFINE_DIFFUSIVITY(diff_CustCon0,c,t,i)
{


    Domain *d;
    d = Set_Domain(1);

    /* LocHug Thread + Zone cell zone ID */
    Thread *C_porous_zone = LocHug_Thread(d,porous_zone_ID);
    Thread *C_fluid_zone = LocHug_Thread(d,fluid_zone_ID);
    /* DaClare Type aC variables */
    real X_CO, X_H2, X_H2O, X_CO2;
    real Temp;
    real G_poro;
    real diff_ansaC;
    real D_H2, D_H2O, D_CO2, D_CO;
    real P;
    real MWavg, Yavg;

    /* Mole FaseClon CalculaClons */
    X_H2 = (C_YI(c,t,0)/MW_H2)/((C_YI(c,t,3)/MW_CO)+(C_YI(c,t,2)/MW_CO2)+(C_YI(c,t,0)/MW_H2)+(C_YI(c,t,1)/MW_H2O)+(C_YI(c,t,3)/MW_CO2));
    X_H2O = (C_YI(c,t,1)/MW_H2O)/((C_YI(c,t,3)/MW_CO)+(C_YI(c,t,2)/MW_CO2)+(C_YI(c,t,0)/MW_H2)+(C_YI(c,t,1)/MW_H2O)+(C_YI(c,t,3)/MW_CO2));
    X_CO2 = (C_YI(c,t,2)/MW_CO2)/((C_YI(c,t,3)/MW_CO)+(C_YI(c,t,2)/MW_CO2)+(C_YI(c,t,0)/MW_H2)+(C_YI(c,t,1)/MW_H2O)+(C_YI(c,t,3)/MW_CO2));
    X_CO = (C_YI(c,t,3)/MW_CO)/((C_YI(c,t,3)/MW_CO)+(C_YI(c,t,2)/MW_CO2)+(C_YI(c,t,0)/MW_H2)+(C_YI(c,t,1)/MW_H2O)+(C_YI(c,t,3)/MW_CO2));


    Temp = C_T(c,t);

    P = ((10000000 + C_P(c,t))/101325); /* OperaCing Pressure - ATM*/

    /* Average Molecular MeigHC and V_DIFF */
    MWavg = 0.324*((X_H2*MW_H2)+(X_H2O*MW_H2O)+(X_CO2*MW_CO2)+(X_CO*MW_CO));
    Yavg = 0.324*((X_H2*V_H2)+(X_H2O*V_H2O)+(X_CO2*V_CO2)+(X_CO*V_CO));

    /* CHANGE IF INITIAL POROSITY CHANGES (INT - INT*C_UDSI) */
    G_poro = 1.0*(2.0*C_UDSI(c,t,0)/(333000000.0*(2.132-(2.132*(C_UDSI(c,t,0))))/2.0); /* 2 is Ceramm KnuGsen*/


    D_H2 = (pow(10,-7)*pow(Temp,1.72)/P)*sqrC((MW_H2+MWavg)/(MW_H2*MWavg))/pow((pow(V_H2,1/3)+pow(Yavg,1/3)),2);
    D_H2O = (pow(10,-7)*pow(Temp,1.72)/P)*sqrC((MW_H2O+MWavg)/(MW_H2O*MWavg))/pow((pow(V_H2O,1/3)+pow(Yavg,1/3)),2);
    D_CO2 = (pow(10,-7)*pow(Temp,1.72)/P)*sqrC((MW_CO2+MWavg)/(MW_CO2*MWavg))/pow((pow(V_CO2,1/3)+pow(Yavg,1/3)),2);
    D_CO = (pow(10,-7)*pow(Temp,1.72)/P)*sqrC((MW_CO+MWavg)/(MW_CO*MWavg))/pow((pow(V_CO,1/3)+pow(Yavg,1/3)),2);

    diff_ansaC = (Temp*Ru*P)/2.1412382222878;

    if (C==C_porous_zone) /*applies Co porous zone*/
    {
        switch(i)
        {
        case 0:
            {
            return pow(C_UDSI(c,t,0),3)*(1/((1/((G_poro*sqrC(diff_ansaC/MW_H2)))) + (1/D_H2)));
            }
        case 1:
            {
            return pow(C_UDSI(c,t,0),3)*(1/((1/((G_poro*sqrC(diff_ansaC/MW_H2O)))) + (1/D_H2O)));
            }
        case 2:
            {
            return pow(C_UDSI(c,t,0),3)*(1/((1/((G_poro*sqrC(diff_ansaC/MW_CO2)))) + (1/D_CO2)));
            }
        case 3:
            {
            return pow(C_UDSI(c,t,0),3)*(1/((1/((G_poro*sqrC(diff_ansaC/MW_CO)))) + (1/D_CO)));
            }
        }
    }
    else if (C==C_fluid_zone) /* applies Co fluid zone*/
    {
        switch(i)
        {
        case 0:
            {
            return D_H2;
            }
        case 1:
            {
            return D_H2O;
            }
        case 2:
            {
            return D_CO2;
            }
        case 3:
            {
            return D_CO;
            }
        }
    }
}
```

Appendix D. Viscous Resistance UDF

```
#include "udf.h"

/*======================================*/
/*
Author: GREG FONG
Last Updated 4/30/2017
Name:Viscous Resistance UDF
Aspects that need to be changed:
-In pore diameter
Specific Volume (m^2/m^3)
(1-X) -> in terms of porosity, C_UDSI
*/
/*======================================*/

DEFINE_PROFILE(perma_fucntion, t, nv)
{
cell_t c;
begin_c_loop(c,t)
{
    /* Uses the cell information from UDS-0*/
    /* 1/perma = 32/dp^2 */
    /* CHANGE IF INITIAL POROSITY CHANGES (INT - INT*C_UDSI) */
    C_PROFILE(c,t,nv) = 32/pow((4.0*C_UDSI(c,t,0))/(322560000.0*(3.125-3.125*C_UDSI(c,t,0))),2);
}

end_c_loop(c,t)
}
```

Appendix E. UDS Unsteady UDF

```
#include "udf.h"

/*=======================================*/
/*
Author: GREG FONG
Last Updated 4/30/2017
Name:Unsteady C_UDSI UDF
Aspects that need to be changed:
N/A
*/
/*=======================================*/

DEFINE_UDS_UNSTEADY(my_uds_unsteady,c,t,i,apu,su)
{
    real physical_dt, vol, phi_old;
    physical_dt = RP_Get_Real("physical-time-step");
    vol = C_VOLUME(c,t);
    *apu = -vol / physical_dt;/*implicit part*/
    *su = vol*C_UDSI_M1(c,t,i)/physical_dt;/*explicit part*/
}
```

Appendix F. UDS to Porosity UDF

```
#include "udf.h"

/*=======================================*/
/*
Author: GREG FONG
Last Updated 4/30/2017
Name:Link UDSI to Porosity UDF
Aspects that need to be changed:
N/A
*/
/*=======================================*/

/* Cell loop within the particle zone to read the value of UDS */
DEFINE_PROFILE(porosity_function, t, nv)
{
    cell_t c;
begin_c_loop(c,t)
{
    /* Uses the cell information from UDS-0*/
    /* CHANGE IF INITIAL POROSITY CHANGES (INT - INT*C_UDSI) */
    C_PROFILE(c,t,nv) = C_UDSI(c,t,0);

}
end_c_loop(c,t)
}
```

Appendix G. Nomenclature - Variables

Variable	Meaning	Unit
A	Pre-Factor Exponential	Varies
a	Cell Coefficient	N/A
$\vec{B}_f$	Body Forces	Pa
b	Source Constant	N/A
C	Molar Concentration	kmol/m^3
C_2	Inertial Resistance	1/m
c_p	Heat Capacity At Constant Pressure	J/kg-K
D	Diffusion Coefficient	m^2/s
d	Diameter	µm
E_a	Activation Energy	kmol/kJ
E	Energy	J
$\vec{F}$	Model-Dependent Source Terms	Varies
$\vec{g}$	Gravity	m/s^2
h	Enthalpy	Varies
$\vec{J}$	Diffusion Flux	kg/m^2-s
K	Viscous Resistance	1/m^2
k	Thermal Conductivity	W/m-K
k_B	Boltzmann Constant	(1.38* 10^{-23} J/molecule-K)
k_r	Reaction Rate Coefficient	Varies
L	Length Scale	N/A
MW_c	Carbon Molecular Weight	kg/kmol
MW	Molecular Weight	kg/kmol
p	Pressure	Varies
R	Radius	m
R_i	Mass Produced of ith Species from Reaction	kg/s
R_u	Universal Gas Constant	Varies
R^ϕ	Residual	N/A
S_g	Specific Surface Area - Mass	m^2/g
S_f^h	Fluid Enthalpy Source	J
S_V	Specific Surface Area - Volume	m^2/m^3
T	Temperature	K
V	Volume	Varies
$\vec{v}$	Velocity	Varies
ν	Atomic Diffusion Volume	N/A
v_{Ci}	Carbon Stoichiometric Coefficient	N/A
W_{Co}	Initial Percentage of Carbon	%
X	Conversion	N/A
Y	Mass Fraction	N/A

ε	Porosity	Void/Total Volume
ε_{L-J}	Lennard-Jones Energy Parameter	J/molecule
η_i	Effectiveness Factor	N/A
μ	Dynamic Viscosity	Pa-s
ρ	Density	Varies
σ	Lennard-Jones Characteristic Length	Å
τ	Tortuosity	N/A
$\bar{\bar{\tau}}$	Stress Tensor	Pa
ϕ_s	General Scalar	Varies
ϕ	Thiele Modulus	N/A
$\Re$	Reaction Rate	1/s
$\Re_s$	Scaling Ratio	N/A

Appendix H. Nomenclature - Subscripts

Subscript	Meaning
$2D$	Unresolved Model – 2D
$3D$	Resolved Model – 3D
A	Arbitrary Species
AS	"A" Surface Species Concentration
atm	Atmospheric
avg	Average
c	Carbon
eff	Effective
f	Fluid
fi	Final
g	Gauge
i	ith Species or Reaction
$knud$	Knudsen
m	Mixture
$macro$	Macropore
$meso$	Mesopore
$micro$	Micropore
nb	Neighboring
o	Initial
op	Operating
p	Particle
s	Solid
t	True
tol	Total
u	Unresolved
$/$	And